UNIVERSITÀ DEGLI STUDI DI PADOVA

DIPARTIMENTO DI INGEGNERIA INDUSTRIALE DII

MASTER DEGREE IN AEROSPACE ENGINEERING

Numerical investigation of the parachute-capsule aerodynamics in a Mars atmosphere reentry

Thesis advisor: Prof. Francesco Picano
Thesis co-advisor: Dr. Luca Placco

Candidate: Giulio Soldati
2021796

ACADEMIC YEAR 2021 – 2022

ABSTRACT

Growing interest in Mars exploration has boosted the research on atmospheric reentry. Especially the descent phase, which starts with the deployment of a supersonic parachute, is subject of numerous studies: the DGB parachute plays a crucial role in the landing of the payload, and inaccurate predictions of its dynamics can lead to the failure of the mission. This thesis concerns the reentry in Martian atmosphere of a capsule based on ExoMars 2022 mission. Focusing on the descent phase, we simulate a compressible flow over the parachute-capsule system flying at supersonic speed. We use a LES to provide a time-resolved representation of the fluid dynamics. Capsule and parachute are considered rigid and fixed in space, and boundary conditions at the fluid-structure interface are enforced through an IBM. The flow is analyzed at the Mach number of parachute deployment, $M_\infty = 2$, and the Reynolds number based on the capsule diameter is $Re = 10^6$. The Navier-Stokes equations in dimensionless form are solved using the in-house code STREAmS.

Simulation results are examined in terms of instantaneous, mean and fluctuating fields. The analysis of instantaneous fields reveals the presence of canonical flow regions – bow shock, expansion fan, lip shock, recompression shock, turbulent wake – around both capsule and parachute. Specific attention is given to the aerodynamic interaction between the capsule wake and the bow shock ahead of the parachute. Fluctuations of the wake are amplified as it crosses the shock, leading to strong flow oscillations and potential system instability. This instability is related to the parachute *breathing*, a cyclic phenomenon that involves a motion of the parachute shock, producing large variations of drag. The breathing cycle is highlighted by computing the RMS of density and pressure fluctuations, and most unsteady flow regions are identified with the help of a TKE map.

Based on these results, we analytically model the breathing, exploring the idea that it is related to the *big buzz* instability. To fully understand the driving mechanisms, the system is simplified by considering a normal shock in front of the parachute. A zero-dimensional model based on a mass balance is developed and validated against the simulation results with excellent match. By setting an input Mach number, the model provides the time-trend of the involved variables, including shock position and parachute drag. The model is also used to conduct a stability analysis as a function of the parachute radius, showing that a larger parachute is subject to smaller fluctuations of density, being consequently more stable. Through a Laplace-domain analysis, the model is reduced to a spring-damper system, allowing to relate a damping coefficient to the radius. Finally, with a frequency analysis we show that the system behaves as a low-pass filter, with cut-off frequency inversely proportional to the radius.

CONTENTS

LIST OF FIGURES

LIST OF TABLES

ACRONYMS

ALE	Arbitrary Lagrangian Eulerian
BCs	Boundary Conditions
CFD	Computational Fluid Dynamics
DES	Detached Eddy Simulation
DGB	Disk-Gap-Band
DNS	Direct Numerical Simulation
EDL	Entry, Descent and Landing
EDM	Entry Demonstrator Module
EIP	Entry Interface Point
ESA	European Space Agency
FSI	Fluid-Structure Interaction
GPFM	Ghost Point Forcing Method
GPU	Graphics Processing Unit
IBM	Immersed Boundary Method
ILES	Implicit Large Eddy Simulation
IMU	Inertial Measurement Unit
LES	Large Eddy Simulation
MER	Mars Exploration Rover
MPF	Mars Pathfinder
MSL	Mars Science Laboratory
NASA	National Aeronautics and Space Administration
PEPP	Planetary Entry Parachute Program
RANS	Reynolds-Averaged Navier-Stokes
RMS	Root Mean Square
STL	Stereolithography
TGO	Trace Gas Orbiter
TKE	Turbulent Kinetic Energy
WENO	Weighted Essentially Non-Oscillatory

1 INTRODUCTION

1.1 MARS ATMOSPHERE REENTRY

Since the beginning of the space age, Mars has been the focus of planetary robotic exploration. There are several strategic, practical and scientific reasons to explore Mars, among which the opportunity to possibly answer origin and evolution of life questions. Specifically, Mars has captured such a high level of interest because:

- it is the most Earth-like of the Solar system planets;
- besides Earth, it is the planet that most likely developed indigenous life;
- it will probably be the first extraterrestrial planet to be visited by humans [1].

The exploration of Mars began in 1960 with NASA's Mariner Program and Soviet Mars Program. After some failures, Mariner 4 was able to execute the first fly-by of Mars in 1965, while Mariner 9 became the first Mars orbiter in 1971. In the same year, Mars 3 was the first spacecraft to obtain a soft landing on Mars, but it could not transmit informations for more than 20 seconds. Later, in 1976, NASA managed to land on Mars two probes, Viking 1 and 2, whose objectives were to take high-resolution images, characterize the composition of atmosphere and surface, search for evidence of life. Viking mission design was influenced by lunar landers (e.g. Apollo) and, with the help of the substantial budget available for its development, the mission was a great success: the Viking 1 lander, designed for a 90-day surface mission, actually transmitted science messages to Earth for seven years. Over the years, there have been many other attempts of landing on Mars. All of post-Viking Mars exploration mission have exploited, to some extent, the heritage left by Viking missions, which became a benchmark as far as Mars atmosphere reentry is concerned. The chronicle of past and present Mars robotic exploration missions is listed in table 1.1, where details about the parachute utilized and the landing outcome are given.

Mission name	Entry year	Agency/ Country	Parachute type and diameter $[m]$	Deployment Mach number	Landing outcome
Viking 1, 2	1976	NASA	DGB, 16.2	2.1	Successful
MPF	1997	NASA	DGB, 12.7	1.71	Successful
MPL	1999	NASA	DGB, 12.7	1.85	Failed
Beagle 2	2003	ESA	DGB, 3.2	1.5	Failed
MER	2004	NASA	DGB, 14.1	1.9	Successful
Phoenix	2008	NASA	DGB, 11.7	1.74	Successful
MSL	2010	NASA	DGB, 21.4	1.75	Successful
ExoMars	2016	ESA/Russia	DGB, 12.0	1.8	Failed
InSight	2018	NASA	DGB, 11.8	1.49	Successful
Tianwen-1	2021	CNSA	DGB, 16.0	1.8	Successful

Table 1.1: Chronicle of past and present Mars robotic exploration missions [2].

ENTRY, DESCENT AND LANDING

The atmospheric reentry of a capsule on Mars comprises a sequence of three phases: Entry, Descent and Landing (EDL). The *entry* phase begins at an altitude of about $125km$, when the capsule reaches the Entry Interface Point (EIP) and comes into contact with Martian atmosphere, traveling at highly hypersonic regimes. The capsule speed at the EIP is about $6000ms^{-1}$, corresponding to a Mach number of $M_\infty \simeq 25$. Such a high value of Mach number is due to the relatively low speed of sound[1] of the rarefied Martian environment. Once the capsule enters Mars atmosphere, the aerodynamic drag begins to act, with consequent capsule deceleration and heating. Prediction of deceleration and heating rate is made complex by the strongly non-ideal behavior of the high-temperature, hypersonic gas flow. In this type of flow, kinetic energy is not integrally transformed into heat, but also into vibrational, dissociation and ionization energy: thus, the simplistic assumption of ideal gas would involve unrealistically high temperatures, well beyond the degradation limits of the material of the capsule shell. The second phase of the reentry is the *descent*: it begins at a Mach number of $M_\infty \simeq 2$, when a supersonic parachute is deployed decelerating the capsule to subsonic speeds. Once the subsonic regime is reached, usually the first parachute is replaced with a second one with a bigger canopy.[2] The *landing* phase starts when the subsonic parachute is ejected, and a rocket landing system is triggered for touchdown. Focus of the present work is the first part of the descent phase, when the capsule is flying with the supersonic parachute deployed.

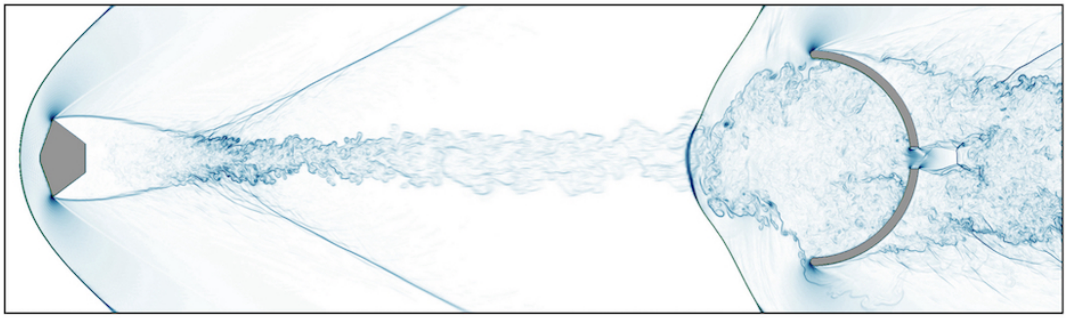

Figure 1.1: Detail of the interaction between the turbulent capsule wake and the canopy bow shock, showing the turbulence *ingestion* by the shock. The image is a snapshot of the numerical Schlieren field, computed by the present simulation.

PARACHUTE-CAPSULE DYNAMICS

To date, the supersonic parachute has been used as decelerator system in all of Mars reentries. Main cause of the *hard* landings (labeled with "Failed" in table 1.1) was an inaccurate prediction of the parachute dynamics, the study of which goes beyond pure aerodynamics. The behavior of a supersonic parachute, in fact, involves interdependent phenomena of Fluid-Structure Interaction (FSI), including bluff body aerodynamics, non-linear structural dynamics, fully coupled interaction between the compressible fluid flow and the deformable membrane structure, undergoing large deformations [3]. In supersonic flight conditions, a specific aerodynamic interaction is observed in the parachute-capsule system. As shown in figure 1.1, the turbulent wake behind the

1 Speed of sound on Mars is $a \simeq 250ms^{-1}$, while on Earth it is $a \simeq 340m^{-1}$.

2 The *canopy* is the dome-shaped part of the parachute, generally consisting of a nylon membrane, which fills with air (or CO_2 in Mars atmosphere) slowing the descent.

capsule interacts with the bow shock ahead of the canopy. This interaction, known as *turbulence ingestion* by the shock, amplifies the fluctuations of the wake as the flow travel across the shock, generating a highly unsteady flow. The source of instability introduced by the capsule wake is coupled with the structural dynamics of the canopy: aerodynamic loads produce large variations in the canopy area, which, in turn, strongly affect the flow behavior. These interactions involve inhomogeneous pressure variations, leading to the parachute *breathing cycle*, an oscillatory phenomenon that produces substantial drag variations and stress fluctuations in the structure. This phenomenon has been recognized through both experimental and numerical observations, and it results in limiting the capability of the supersonic parachute to act as an effective decelerating device. However, the causes of the breathing cycle are still not well known. These phenomena of different nature, interacting with each other, make complex the study on atmospheric reentry, which is a research topic that still demand further investigation.

1.2 CAPSULE CONFIGURATION

For both manned and unmanned atmospheric reentries, the capsule is designed with a blunt body configuration, selected as a result of extensive studies. The atmospheric reentry was first studied by NASA within the programs Mercury, Gemini and Apollo, whose main goal was to land astronauts on the Moon. The success of these missions was made possible by the "Blunt Body Theory" proposed in 1951 by Harvey Allen, which led to the design of capsules shaped as we know them today, in opposition to needle-nose missiles.

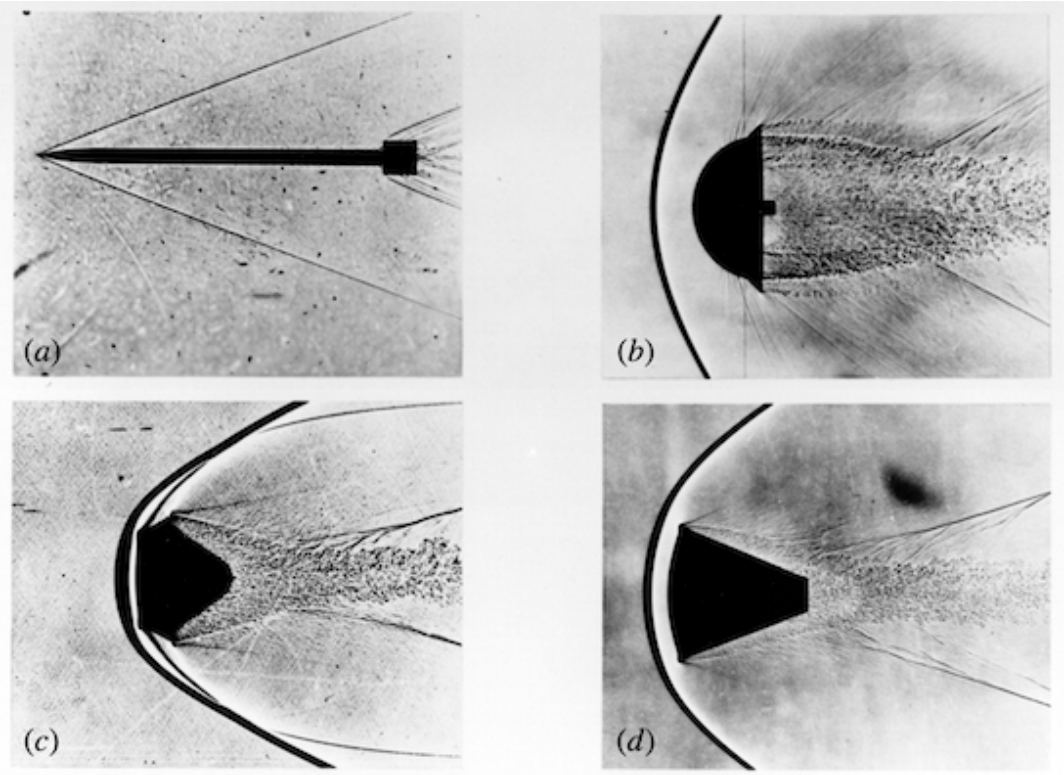

Figure 1.2: Early reentry vehicle concepts (NASA): needle-nose missile (a), blunt-body concept, 1953 (b), nose cone missile (c), manned-capsule concept, 1957 (d).

BLUNT BODY THEORY

For any shape, the kinetic energy from high reentry speed goes into both heating the body and heating the airflow around the body. The intense friction from the boundary layer heats the body, while the shock wave caused by the nose heats the airflow. If more energy is put into the airflow, then less is left to heat the vehicle. Ballistic vehicles with pointed noses generate a weak shock wave – an attached *oblique* shock – leading to a low ratio of pressure drag to friction drag and, consequently, to high vehicle heating. In contrast, Allen proposed to use blunt noses, with a radius of curvature as large as possible, in order to create a strong shock wave – a detached *bow* shock – standing ahead of the vehicle: the high ratio of pressure drag to friction drag would conceivably solve heating problems [4]. The frontal bow shock created by blunt configurations produces high surface pressure and, consequently, high aerodynamic drag. During the entry phase, aerodynamic drag is used to aerobrake the capsule from hypersonic to low-supersonic speeds, before the parachute deployment [5].

Although lower than in the case of hypothetical slender bodies under the same conditions, temperatures on the capsule surface are still extremely high, reaching up to 1500 $°C$ during the entry phase in Martian atmosphere. Thus, entry vehicles are equipped with a frontal heat shield, which protects the crew cabin or the robotic payload from high heat fluxes. The heat shield is generally axisymmetric, with either a sphere-cone or spherical geometry; together with the back shell, it constitutes the full *aeroshell* coating the capsule [6]. While flying through the atmosphere, the capsule is invested by a flow that develops specific features, strongly influenced by the capsule configuration.

SUPERSONIC FLOW OVER A CAPSULE

A sketch of the supersonic flow field over a blunt body is shown in figure 1.3 (a). In the fore-body section of the capsule the fluid decelerates through a bow shock wave. At the corner of the capsule (*shoulder*), the flow turns and rapidly expands. The expansion process follows a fan pattern, modified by both the approaching boundary layer and the radius of the bevel. The boundary layer detaches, forming a free-shear layer in the back-shell region. In correspondence of the free-shear layer generates the *lip* shock wave, separating the inner recirculating flow from the outer inviscid flow. The inner flow forms the near wake, while the outer flow is turned back to the free stream direction by the *recompression* shock wave. At the end of the recirculating region, the free-shear layer develops in the wake trail. The far wake region is characterized by free-shear layers, regions of flow contraction (*necks*) and recompression shocks [7]. From figure 1.3 (b), representing a snapshot of the Mach number field, we can see that these general features are clearly captured by the present simulation.

Despite the Blunt Body Theory was originally developed for reentry missions into Earth atmosphere, the same flow features can be generalized to all atmospheric reentries. In the context of Mars exploration, the capsule interacts with the rarefied atmosphere of Mars. Mainly composed of carbon dioxide (with small amounts of nitrogen and argon), Martian atmosphere reaches up to an altitude of about $150km$, with a surface pressure around $1000Pa$. To decelerate in this environment, the capsule requires a parachute, which is still an effective decelerator although Martian atmosphere has a volume of 1% compared to Earth's. From the simulation results, presented in chapter 3, we will see that the flow field around the parachute exhibits the same characteristics as the flow field around the capsule. The difference is that the incoming flow of the capsule wake is turbulent, causing high instability around the parachute region.

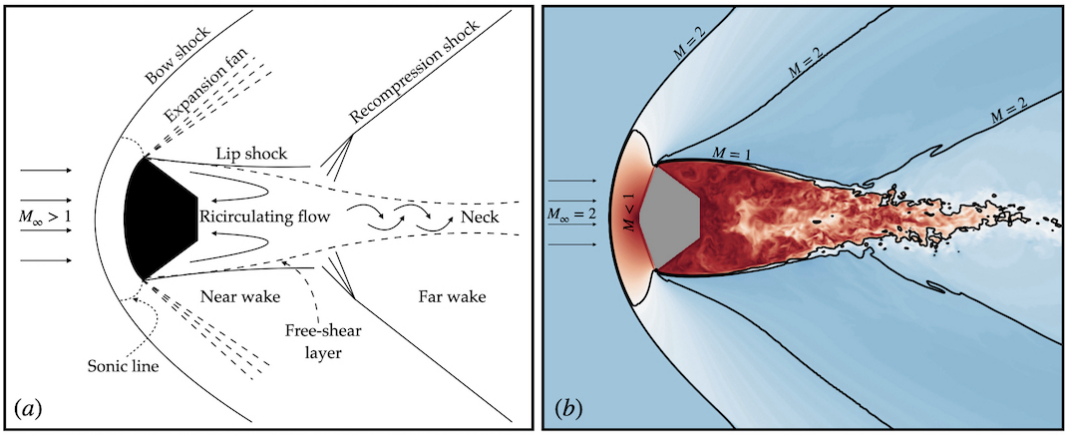

Figure 1.3: Illustration of a supersonic flow over a reentry vehicle. Main flow features are qualitatively represented in (a). Mach number field is quantitatively represented in (b), a snapshot of our simulation, where $M_\infty = 2$. Black isolines correspond to $M = 1$ and $M = 2$.

1.3 PARACHUTE CONFIGURATION

Capsule heat shields have the double function of high-temperature protection and deceleration system, due to their blunt shape. However, such aeroshells do not have sufficient area of resistance to bring the spacecraft safely to the surface: aerodynamic decelerators, thus, are called upon. Parachutes have been used in all Mars landings, due to their efficiency given by the high ratio of aerodynamic drag to mass [2]. For reasons of stability and material strength, the parachute is deployed when the Mach number has dropped to $M_\infty \simeq 2$, and slows the capsule down to subsonic speeds ($M_\infty \simeq 0.1$). The parachute is the key factor for a successful landing of the payload, as it serves several crucial functions:

- decelerate the capsule from supersonic to subsonic speeds;
- provide specific descent rate, to obtain scientific measurements;
- provide stability (*drogue function*), to prevent aeroshell tumbling and meet instrumentation requirements;
- effect the deployment of further aerodynamic decelerator system (*pilot function*);
- provide difference in ballistic coefficients, to enable separation events;
- provide height and timeline, to allow the completion of the EDL sequence.

Being perturbed by the turbulent wake that develops behind the capsule, the parachute tends to destabilize and oscillate. These oscillations affect the trajectory of the capsule: since it is coupled with the parachute, the capsule responds dynamically to parachute oscillations, triggering a self-excited mechanism that can lead to uncontrolled vibrations and possible mission failure. Particular emphasis, thus, should be placed on to the drogue function, aiming to minimize the oscillations of the parachute and ensure its stability.[3] Precisely with this purpose, the Disk-Gap-Band (DGB) configuration was conceived and developed.

3 *Stability* is defined as maintaining parachute oscillations below 6° [8].

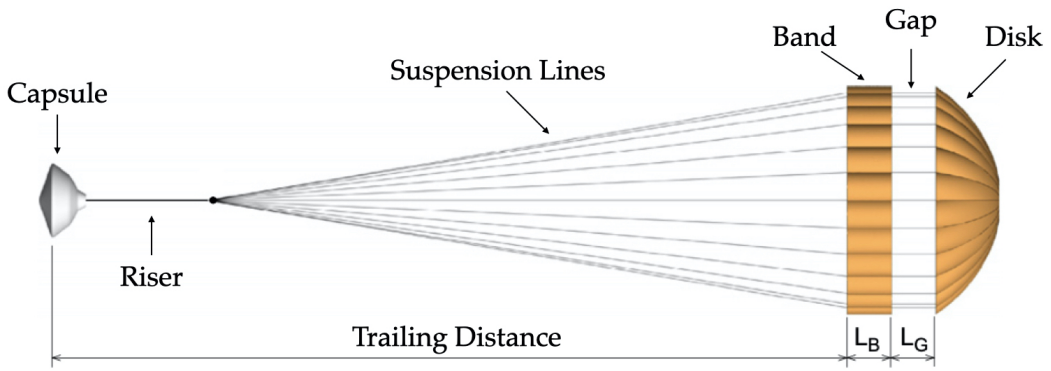

Figure 1.4: Geometric configuration of a Disk-Gap-Band (DGB) supersonic parachute [3]. Clearly, the real system would be placed in vertical direction, with the capsule at the bottom and the canopy at the top.

DISK-GAP-BAND PARACHUTE

Relatively few parachute configurations have been tested and applied in supersonic regime: among these, the most widely used in planetary applications is the Disk-Gap-Band (DGB) parachute. As the name suggests, the basic design elements are a circular disk and an orthogonal cylindrical band, separated by a gap between the two. An illustration of the DGB configuration is represented in figure 1.4. The DGB design was originally devised by Clint Eckstrom in the early 1960's for high-altitude meteorological rocket applications. It was designed as a balance between drag and stability, with a relatively simplistic design and low packing volume. To minimize weight, Eckstrom used polyethylene terephthlate (Mylar) for the fabrication of the canopy. In supersonic conditions, it is necessary for the canopy to be partially permeable to flow, so the parachute can be stable: since Mylar is devoid of fabric porosity (i.e. impermeable), a *geometric* porosity in the canopy was needed to improve stability. This was achieved with the inclusion of vent and gap [9]. Due to its demonstrated high-altitude performance, the DGB was selected as a candidate for planetary missions.

Within the Planetary Entry Parachute Program (PEPP), the DGB configuration was studied by NASA through an experimental approach, in order to provide test data in low-density environments. Specifically for Viking mission, after considering a variety of options, NASA selected a single DGB parachute as its aerodynamic decelerator system. The development and qualification process of the Viking parachute consisted of four main elements: wind tunnel tests, low-altitude subsonic drop tests, high-altitude flight tests and mortar tests. Currently, it is the most extensive and documented parachute qualification program for an unmanned planetary exploration mission [10]. The parachute design developed for Viking had demonstrated suitable flight characteristics in supersonic conditions, which were difficult and expensive to duplicate in test. The Viking DGB parachute, therefore, has become a benchmark, and all subsequent Mars exploration missions have utilized Viking-derived parachutes. In the following, we will try to motivate the design choices of the Viking-type DGB parachute from a theoretical and quantitative point of view, identifying the possible directions along which advancements can be made from the state of the art.

1.4 ESA'S EXOMARS MISSION

ESA's ExoMars program comprises two missions: the first consists of the Trace Gas Orbiter (TGO) and Schiaparelli Entry Demonstrator Module (EDM), and was launched in 2016; the second comprises a rover and surface platform, and – in the days this thesis is written – is still awaiting confirmation for launch.

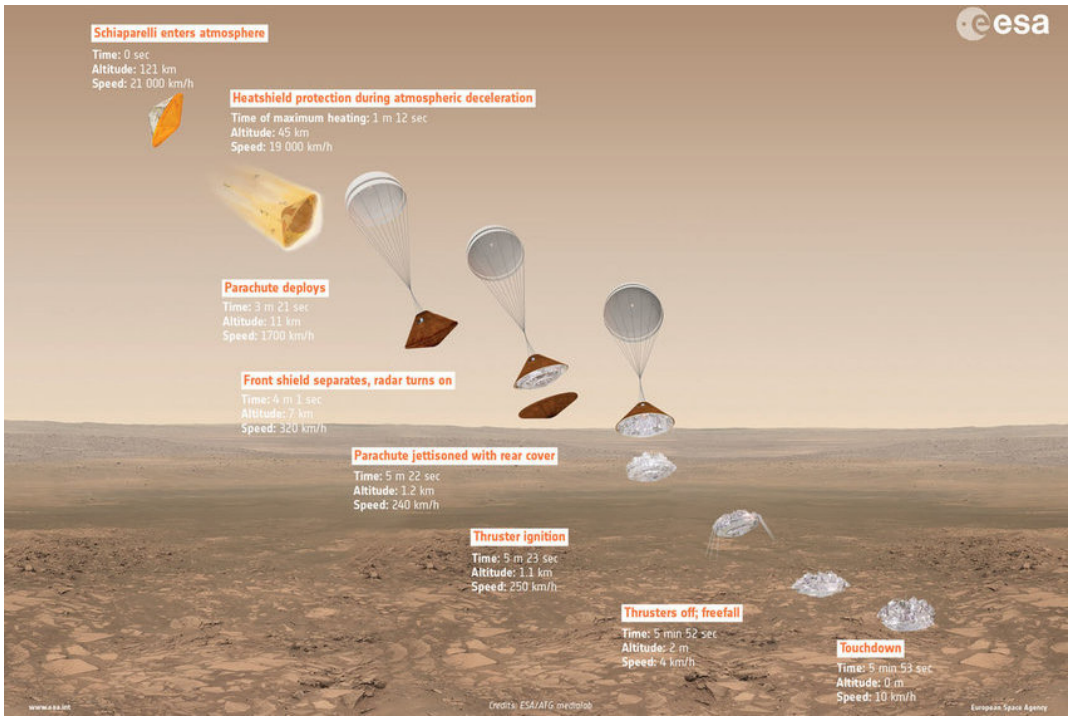

Figure 1.5: Illustration of the EDL sequence of ESA's ExoMars 2016 mission.

FIRST PART – EXOMARS 2016

Schiaparelli EDM was designed to demonstrate and validate a European capability for Entry, Descent and Landing (EDL) on Mars. Launched on 14th March 2016, after six months of interplanetary cruise, TGO delivered Schiaparelli in a ballistic trajectory toward Mars. The module woke up from its hibernation state after 72 hours, one hour before the expected EIP with the atmosphere. On 19th October 2016, Schiaparelli flew through Mars atmosphere. After a successful entry, Schiaparelli failed the last part of the descent and crashed on Mars soil [11]. The EDL sequence, illustrated in figure 1.5, was designed to last about 6 minutes. A hypersonic entry should have been followed by a passive parachute descent and an active proximity phase: thanks to the activation of retrorockets, horizontal accuracy of the landing would have been improved. Schiaparelli should have finally landed on a crushable structure, designed to dampen the impact [12].

However, shortly after the parachute inflation, the capsule began to oscillate with angular rates that exceeded the saturation limit of the Inertial Measurement Unit (IMU). The IMU saturated, providing the control software with the wrong attitude of the module. This led to an incorrect altitude estimation and in a premature activation of the terminal descent phase. After a free fall of 33 seconds, Schiaparelli impacted the surface at a speed of $150 ms^{-1}$. According to the Schiaparelli Anomaly Inquiry report, main causes of the unexpectedly-high angular rates were two:

- large canopy motion, due to unsteady wake dynamics;

- force oscillation along the riser, due to variations of the canopy area.

These phenomena are strongly coupled and excite each other. Actually, the flexibility of the canopy (and thus its variations of area) were not considered in the multi-body model of the simulator that was used to study the EDL aerodynamics [13].

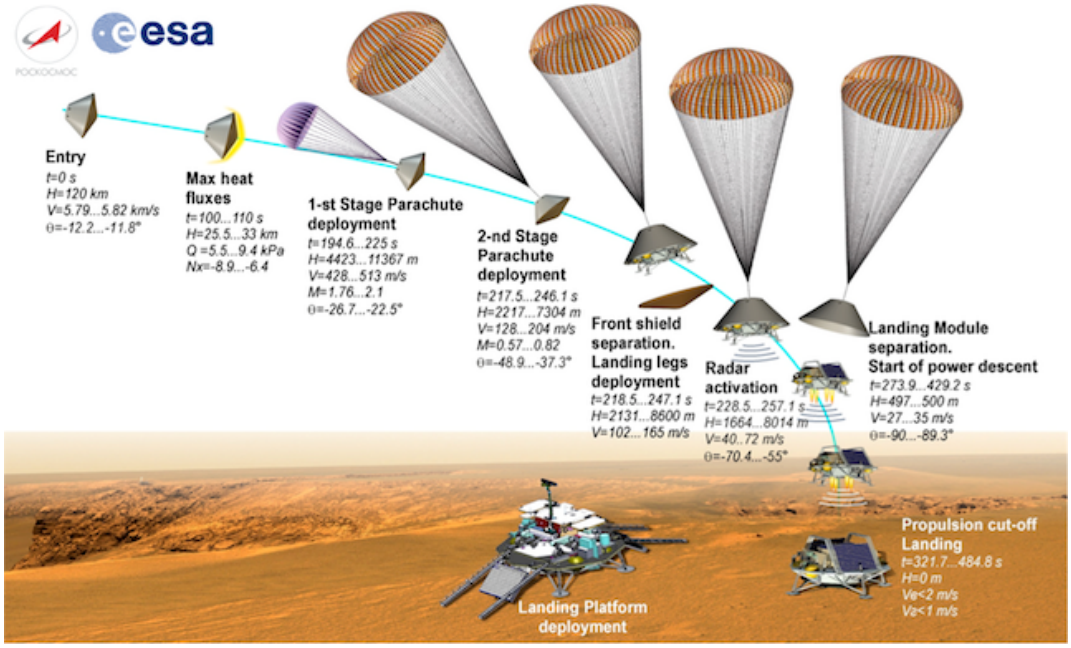

Figure 1.6: Illustration of the Entry, Descent and Landing (EDL) sequence of ESA's ExoMars 2022 mission.

SECOND PART – EXOMARS 2022

After Schiaparelli, ESA has planned a new landing on Mars with the second part of the mission. The launch, initially scheduled for October 2022, has been postponed to a date to be determined. A descent module containing a rover will be transported towards Mars and will follow an EDL sequence, aiming to achieve a soft landing [14]. The planned EDL is shown in figure 1.6.

The capsule is a scaled-up version of Schiaparelli. It is equipped with two parachutes that will be utilized during the descent phase. At $M_\infty \simeq 2$ will be deployed the DGB supersonic parachute, which will drive the capsule velocity to subsonic regimes in about $20s$. This phase is specifically investigated in the present work. At $M_\infty \simeq 0.7$, then, will be deployed the subsonic *ringslot* parachute, which is provided with a larger canopy. The use of a larger drag area is made possible by the fact that aerodynamic loads to be withstood are less intense, since they scale with the velocity squared. In any case, the second parachute also needs high geometric porosity, given by the numerous gaps between the bands that constitute the ringslot model.

The rover, named Rosalind Franklin, is equipped with a drill, through which will be extracted underground samples – more likely to include biomarker, since the tenuous martian atmosphere offers little protection from radiation and photochemistry at the surface – and they will be analyzed thanks to an on-board laboratory. Forward-looking, the experimental setup of the present work is based on ExoMars 2022 mission. The key difference from ExoMars 2016 is the presence of two parachutes instead of one: this choice is required by the increased weight of the descent module compared to Schiaparelli.

1.5 LITERATURE REVIEW

Within the broad topic of Mars atmosphere reentry, we will focus the present study on the descent phase of a capsule flying with a deployed parachute at supersonic speed. Over the past 60 years, the study on the supersonic parachute-capsule system has significantly progressed, and yet it is still evolving, as we will see in this brief review of the available literature on this problem.

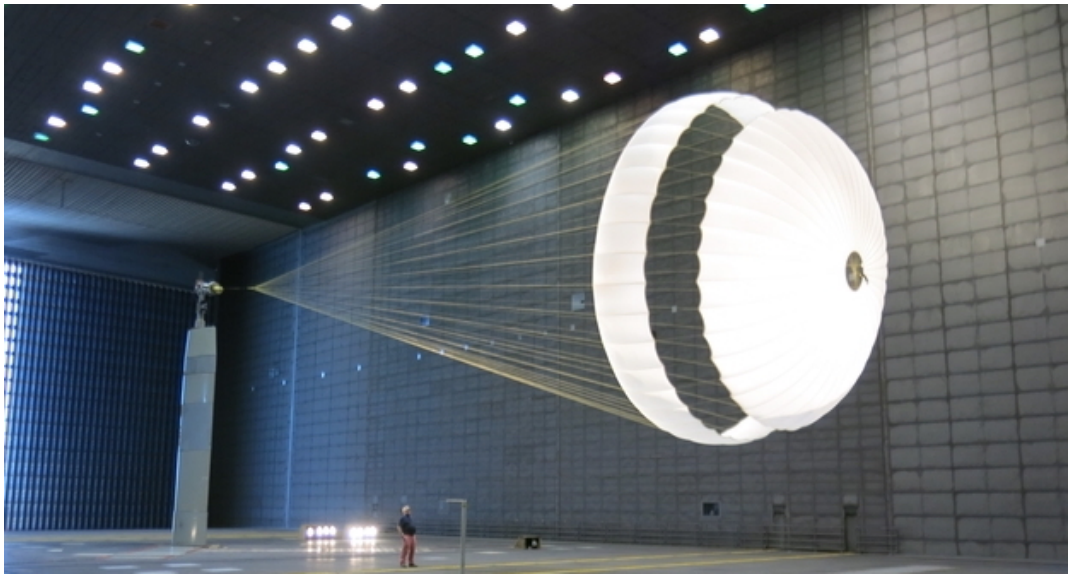

Figure 1.7: Schiaparelli's parachute during wind-tunnel testing. USAF Arnold Engineering Development Complex.

EXPERIMENTAL STUDIES ON SUPERSONIC PARACHUTES

The study of the behavior of supersonic parachutes was first approached experimentally within NASA's Project Mercury. Through a wind tunnel campaign, Maynard [15], 1961 identified the most critical flight regime at a Mach number of $M_\infty \simeq 2$, at which the parachute is prone to large oscillations and the system tends to be unstable. At higher Mach number, drag decreases rapidly because of inflation instability. The research had slowly established that parachute oscillations were a by-product of the turbulent wake developed behind the capsule. It was also shown that the parachute performance decreased, in terms of drag and stability, when the canopy bow-shock was shifted upstream to the capsule.

In order to improve the parachute performance at high Mach numbers, the Disk-Gap-Band (DGB) design was investigated and flight-tested by Eckstrom et al. [16], 1967 as part of the program PEPP. Within Viking mission, these studies were expanded for applications in the rarefied atmosphere of Mars with several high-altitude flight tests [17], [18], [19], [20]. Steinberg et al. [21], 1974 conducted a wind tunnel study of a 10% scale-model of the Viking DGB parachute. It was found that the drag coefficient reached a maximum value at $M_\infty = 1.4$, while further Mach number increase involved a drag reduction. It was also noted that a substantial drag increase was achieved by increasing the ratio of cables length to canopy diameter (L/D). Cruz et al. [22], 2003 tested in wind tunnel two type of DGB parachutes, based on Mars Exploration Rover (MER) and Mars Pathfinder (MPF) missions, in order to determine drag and stability coefficients. Their study showed that increasing the relative height of the band in a DGB parachute decreases the drag, on one side, and improves the static

stability, on the other. Moreover, it pointed out the relevant effect of fabric porosity on drag and stability, besides geometric porosity.

Sengupta et al. [23], 2009 tested in wind tunnel a scaled version of the DGB parachute of the Mars Science Laboratory (MSL) mission. Specifically, they investigated the effect of parachute trim angle with respect to alignment with the entry vehicle wake, from $M_\infty = 2$ to $M_\infty = 2.5$. High-speed shadowgraph video of the upstream parachute flow-field was used to capture bow shock motion and standoff distance oscillation, two phenomena related to the so-called parachute *breathing*.

NUMERICAL STUDIES ON SUPERSONIC PARACHUTES

Computational research on supersonic parachutes began relatively late, because of the complex parachute-capsule dynamics, mentioned in section 1.1. Lafarge et al. [24], 1993 proposed a Computational Fluid Dynamics (CFD) code coupled with finite-element structural analysis to calculate the distribution of pressure and temperatures on the canopy surface of a cross parachute at high supersonic Mach numbers. Early studies on FSI used an Arbitrary Lagrangian Eulerian (ALE) method to simulate flexible parachute systems in supersonic conditions, as presented by Lingard et al. [25], 2005. They used a fully coupled Fluid-Structure Interaction (FSI) model to simulate a flexible DGB parachute flying in the wake of a capsule at $M_\infty = 1.5$, discussing the effect of both fore-body wake and trailing distance on parachute drag at different Mach numbers. This FSI model was also used to study the supersonic parachute system for MSL mission [26].

Barnhardt et al. [27], 2007 used the Detached Eddy Simulation (DES) to study the aerodynamics of a rigid DGB parachute based on MSL mission in supersonic conditions. It was found that the time-varying momentum deficit in the capsule wake interacts with the bow shock ahead of the canopy, generating a highly unsteady flow. An alternating over- and under-pressurization of the canopy (*breathing cycle*) leads to a periodic motion of the canopy bow shock, and to a consequent oscillation of the drag coefficient. Sengupta et al. [28], 2008 used FSI computational methods (validated through sub-scaled wind-tunnel experiments) to assess the MSL parachute behavior. A relevant finding was that, as the relative size of the canopy to the capsule wake increases, the flow becomes more stable.

Karagiozis et al. [3], 2011 studied the FSI of a flexible DGB parachute and a supersonic flow at Mach number around 2. They used a new computational approach, based on Large Eddy Simulation (LES) and Immersed Boundary Method (IBM), to couple the finite-difference flow solver with the finite-element structural thin-shell solver. Their simulation reproduced large canopy-area oscillations, which are related to the parachute breathing cycle. They also showed that, increasing the Mach number, drag decreases and its variability increases. This research was continued by Pantano et al. [29], 2019 improving the information exchange between solvers thanks to a feedback scheme. They pointed out that the main factor affecting the drag coefficient is the behavior of canopy deformations under dynamic loads, which is characterized by the canopy projected area. After an initial transient, flow and structure dynamics synchronize, and the parachute starts its breathing cycle, with strong *inhaling* and *exhaling* of the parachute.

Xue et al. [30], 2015 investigated the effect of suspension lines on the supersonic parachute behavior. The canopy bow shock interacts with the suspension line shocks and develops into a multiple shock system, which then couples with the capsule wake. Instantaneous pressure distribution on the canopy surface is slightly modified, while mean pressure distribution is unchanged by the presence of the cables. Yang [31],

2021 studied the effect of air permeability, showing that a porous canopy improves the static stability of the system compared to a non-porous one. Finally, Xue and Wen [2], 2021 published a review with last developments in both computational study and experimental research of supersonic parachutes for Mars exploration missions.

1.6 THESIS MOTIVATIONS AND OUTLINE

It is current belief that the growing interest in Mars robotic exploration, along with the space agencies goal of sending humans to Mars, requires further investigation of the parachute-capsule aerodynamics in a Mars atmosphere reentry. We have seen that this problem can be addressed experimentally or numerically: both approaches offer several advantages but, currently, they still suffer from some limitations.

MOTIVATIONS

In the experimental context, the conditions of Martian atmosphere can be reproduced on Earth by following two approaches, both of which are extremely complex and expensive. The first approach consists of high-altitude flight tests: despite offering the most realistic configuration, where parachute and capsule dynamics are actually coupled, it must cope with the difficulty in controlling the atmospheric environment, and can hardly give a full representation of the parameters encompassed during the descent. The second approach, relying on tests conducted in supersonic wind tunnels, has provided relevant developments in this research; however, it must still face some difficulties. First, it suffers from a scale effect: actual parachutes are excessively large for the tunnels, and have to be downsized. To maintain the right proportions, cables diameter of the scaled model becomes too small to be fabricated. In addition, it is challenging to avoid any perturbation from the support parts for a two-body configuration [32], and the motion of the capsule, which must be kept fixed, is not affected by the parachute dynamics.

Recent advancements of the parallel computing, boosted by the development of Graphics Processing Unit (GPU) technology, enabled the study on the supersonic parachute-capsule system through a computational approach. The development of advanced numerical methods is essential to obtain reliable results for these type of configurations, which cannot be easily tested on Earth. However, state-of-the-art numerical methods are not yet able to provide comprehensive results, due to several complexities.

The investigated flow is characterized by both a supersonic Mach number and a high Reynolds number; in addition, it develops around solid bodies with complex geometries. Currently, fully resolved Direct Numerical Simulation (DNS) are not feasible for this type of flows, and a model of turbulence must be adopted. Different models have been proposed to simulate turbulent compressible flows, mostly based on the Reynolds-Averaged Navier-Stokes (RANS) technique. This technique, if extremely efficient from a computational point of view, is unable to capture the non-stationary nature of the flow, since it can only compute time-averaged quantities. Therefore, RANS-based methods struggle to reliably represent the fluid dynamics of a supersonic parachute-capsule system. A compelling evidence of the need for numerical methods better suited to reproduce Mars atmosphere reentries is given by the unfortunate outcome of ESA's ExoMars 2016 mission, discussed in section 1.4.

One of the major difficulties in studying the parachute-capsule system is due to the instability of the flow field. Especially when the flight regime is supersonic, the

wake from the capsule interacts with the bow shock ahead of the canopy, amplifying flow fluctuations. The flow unsteadiness is further increased by the flexible canopy deformations, which depend on the flow behavior and, in turn, they influence it back. This coupling could be captured by numerical methods based on Fluid-Structure Interaction (FSI). In this context, an interesting research has recently been undertaken, but FSI methods specifically suited for atmospheric reentry are still under development. The problem that most limits this approach is ensuring a time-accurate coupling between flow solver and structure solver, as fluid and canopy dynamics are strongly coupled.

THESIS OUTLINE

Compared to FSI, the CFD allows an easier and straightforward study of the aerodynamic interactions around a parachute-capsule system. Thus, we will simplify the system employing a rigid parachute model to fully understand the basic flow physics, without considering the effect of the parameters depending on the flexible structure. Focusing on the first part of the descent phase, we will analyze the aerodynamic behavior of a supersonic parachute-capsule system based on ExoMars 2022 mission, after the initial transient of the parachute inflation.[4] We will perform an Implicit Large Eddy Simulation (ILES) of compressible flow, in order to capture the unsteadiness of the flow, without the addition of any external model of turbulence. The fluid-structure interface, i.e. capsule and parachute surfaces, will be modeled through the Ghost Point Forcing Method (GPFM), a discrete-forcing IBM.

In the first instance, simulation results will be analyzed in terms of instantaneous fields; these will be subsequently decomposed into mean fields and fluctuating fields, for a more complete study of the problem. As mentioned in section 1.5, the aerodynamic interaction between capsule wake and canopy bow shock is related to the so-called *breathing cycle* of the parachute. Due to its central role in the parachute dynamics, this interaction will be deeply investigated. The parachute breathing involves an oscillation of the bow shock, leading to large variations of pressure and possible instability of the system. A similar dynamics characterizes the *big buzz instability*, a phenomenon of self-sustained shock oscillations, which occurs in supersonic inlets when the incoming mass flow is overly reduced.

Investigating the idea that the driving mechanism of parachute breathing is the same as big buzz, we will develop a zero-dimensional model that it is able to capture and describe the breathing cycle. By assuming a normal shock ahead of the canopy and a straight sonic line between shock and parachute, we will derive the governing equation of the system from a flow mass balance within the canopy volume, assessing time-trends of the variables of interest. Moreover, the original model will be simplified and traced back to a spring-damper system, allowing to give a physical meaning to the main parameters, as well as to analyze its frequency response. This model can help to evaluate the effect of geometric parameters (such as the ratio of trailing distance to canopy diameter, L/D) on parachute drag and stability, depending on different environmental conditions and external disturbances.

4 Approaches dfferent from the present one are needed to study the parachute inflation, for which we refer to Huang et al. [33], 2020.

2 METHODOLOGY

2.1 BALANCE EQUATIONS

The behavior of a Newtonian, isotropic fluid is mathematically described by the Navier-Stokes equations, which are derived from the fundamental principles of mass, momentum and energy conservation. In the case of a compressible, viscous, heat-conducting gas, the Navier-Stokes equations can be expressed as follows

$$\frac{\partial \rho}{\partial t} + \frac{\partial (\rho u_j)}{\partial x_j} = 0 \tag{2.1a}$$

$$\frac{\partial (\rho u_i)}{\partial t} + \frac{\partial (\rho u_i u_j)}{\partial x_j} + \frac{\partial p}{\partial x_j} - \frac{\partial \sigma_{ij}}{\partial x_j} = 0 \tag{2.1b}$$

$$\frac{\partial (\rho e)}{\partial t} + \frac{\partial (\rho e u_j + p u_j)}{\partial x_j} + \frac{\partial q_j}{\partial x_j} - \frac{\partial (\sigma_{ij} u_i)}{\partial x_j} = 0 \tag{2.1c}$$

where t is the time, ρ is the gas density, x_i is the i-th direction ($i = 1, 2, 3$), u_i is the velocity component in the i-th direction, p is gas thermodynamic pressure, e is the total energy per unit mass. The viscous stress tensor, σ_{ij}, and the total heat flux, q_j, are respectively defined as

$$\sigma_{ij} = \mu \left(\frac{\partial u_i}{\partial x_j} + \frac{\partial u_j}{\partial x_i} - \frac{2}{3} \frac{\partial u_k}{\partial x_k} \delta_{ij} \right) \tag{2.2}$$

$$q_j = -\lambda \frac{\partial T}{\partial x_j} \tag{2.3}$$

where μ is the gas dynamic viscosity, δ_{ij} is the Kronecker delta, T is the gas temperature, λ is the heat transfer coefficient. This model consists in 5 equations with 7 unknowns (ρ, u_i, e, p, T): the system must be completed by adding an equation of state and a constitutive equation for the total energy. The analyzed conditions allow us to assume a calorically perfect gas:[1] this assumption leads, respectively, to

$$p = \rho R T \tag{2.4}$$

$$e = c_v T + \frac{u_i u_i}{2} \tag{2.5}$$

where R is the specific gas constant[2] and c_v is the heat coefficient at constant volume. The system of equations 2.1 is now autonomous, but it can be reformulated in a more convenient way.

1 The assumption of calorically perfect gas is valid as long as its temperature is lower than $T \sim 1000K$. In the present case ($M_\infty = 2$), the maximum temperature reached by the gas is $T \sim 400K$.

2 The specific gas constant is defined as $R = \mathscr{R}/\mathscr{M}$, where $\mathscr{R} = 8.314$ J $\cdot$ mol$^{-1}\cdot$ K^{-1} is the universal gas constant, and $\mathscr{M}$ [kg $\cdot$ mol^{-1}] is the molar mass of the gas.

DIMENSIONLESS NAVIER-STOKES EQUATIONS

In the present work, we utilize a non-dimensional formulation of the Navier-Stokes equations (2.1). This formulation is useful to minimize the number of independent parameters that control the system, as well as normalize the relevant quantities to be order one, reducing the computational cost. Dimensionless quantities, $\bullet'$, are obtained through a change of variables: each dimensional variable is expressed as the product between the corresponding dimensionless variable and a reference quantity, $\bullet_0$

$$\begin{aligned} x = l_0 x', \quad u_i = u_0 u_i', \quad t = t_0 t', \quad \rho = \rho_0 \rho', \\ T = T_0 T', \quad e = e_0 e', \quad \mu = \mu_0 \mu', \quad \lambda = \lambda_0 \lambda'. \end{aligned} \tag{2.6}$$

The choice of reference values is arbitrary. In this work, they are defined as follows

$$\begin{cases} \rho_0 = \rho_\infty \\ p_0 = p_\infty \\ T_0 = T_\infty \\ l_0 = D_0 \end{cases} \implies \begin{cases} R_0 = p_0 (\rho_0 T_0)^{-1} \\ u_0 = \sqrt{R_0 T_0} \\ t_0 = l_0 / u_0 \\ \mu_0 = \rho_0 u_0 l_0 \\ \lambda_0 = \mu_0 R_0 \\ c_{p0} = \gamma R_0 (\gamma - 1)^{-1} \\ c_{v0} = R_0 (\gamma - 1)^{-1} \\ e_0 = c_{v0} T_0 + u_0^2 / 2 \end{cases} \tag{2.7}$$

where c_p is the heat coefficient at constant pressure. The reference length, l_0, is set equal to the capsule diameter, D_0. Reference values 2.7 have been chosen because they allow us to work with free-stream quantities that are unitary

$$\rho_\infty' = p_\infty' = T_\infty' = R_\infty' = 1 \tag{2.8}$$

From Buckingham's Π theorem,[3] we know that the compressible Navier-Stokes equations system can be described by 4 fundamental dimensionless groups. Using reference values 2.7, we define the following fundamental groups

$$\textit{Heat capacity ratio} \longrightarrow \gamma = \frac{c_{p0}}{c_{v0}} \longrightarrow \frac{\text{Entalpy}}{\text{Internal energy}}$$

$$\textit{Free-stream Mach number} \longrightarrow M_\infty = \frac{u_\infty}{\sqrt{\gamma R_0 T_0}} \longrightarrow \frac{\text{Velocity}}{\text{Speed of sound}}$$

$$\textit{Reynolds number} \longrightarrow Re = \frac{\rho_0 u_\infty l_0}{\mu_\infty} \longrightarrow \frac{\text{Inertial forces}}{\text{Viscous forces}}$$

$$\textit{Prandtl number} \longrightarrow Pr = c_{p0} \frac{\mu_\infty}{\lambda_\infty} \longrightarrow \frac{\text{Viscous diffusion}}{\text{Thermal diffusion}}$$

to which we have associated the respective physical meaning. We observe that the physical meaning of γ is only valid under the assumption of perfect gas. Imposing

3 Buckingham's Π theorem is used to determine the number of dimensionless groups required to describe a physical system, stating that the number of dimensionless groups, p, to define a system equals the total number of variables, n, minus the fundamental dimensions, k. Hence, $p = n - k$.

the values of these groups, we are able to compute free-stream quantities, which are normalized using reference values 2.7

$$u'_\infty = \frac{u_\infty}{u_0} = \frac{M_\infty \sqrt{\gamma R_0 T_0}}{\sqrt{R_0 T_0}} = \sqrt{\gamma} M_\infty \tag{2.9}$$

$$\mu'_\infty = \frac{\mu_\infty}{\mu_0} = \frac{\rho_0 u_\infty l_0}{Re} \cdot \frac{1}{\rho_0 u_0 l_0} = \frac{\sqrt{\gamma} M_\infty}{Re} \tag{2.10}$$

$$\lambda'_\infty = \frac{\lambda_\infty}{\lambda_0} = \mu_\infty \frac{c_{p0}}{Pr} \cdot \frac{1}{\rho_0 u_0 l_0 R_0} = \frac{\gamma}{\gamma - 1} \cdot \frac{1}{Pr} \cdot \frac{\sqrt{\gamma} M_\infty}{Re} \tag{2.11}$$

From now on, we will always refer to dimensionless (or normalized) quantities. Therefore, we omit to indicate them as $\bullet'$, and we simply use the symbol of their respective variables. Hence, we can write the *dimensionless* Navier-Stokes equations for a viscous, heat-conducting, ideal gas

$$\frac{\partial \rho}{\partial t} + \frac{\partial (\rho u_j)}{\partial x_j} = 0 \tag{2.12a}$$

$$\frac{\partial (\rho u_i)}{\partial t} + \frac{\partial (\rho u_i u_j)}{\partial x_j} + \frac{\partial p}{\partial x_j} - \frac{\sqrt{\gamma} M_\infty}{Re} \cdot \frac{\partial \sigma_{ij}}{\partial x_j} = 0 \tag{2.12b}$$

$$\frac{\partial (\rho e)}{\partial t} + \frac{\partial (\rho e u_j + p u_j)}{\partial x_j} - \frac{\sqrt{\gamma} M_\infty}{Re} \left[\frac{\partial (\sigma_{ij} u_i)}{\partial x_j} - \frac{\gamma}{\gamma - 1} \cdot \frac{1}{Pr} \cdot \frac{\partial q_j}{\partial x_j} \right] = 0 \tag{2.12c}$$

The assumption of a calorically perfect gas implies that heat capacity ratio, γ, and Prandtl number, Pr, are constant. With the intent of reproducing Martian atmosphere, we consider a perfect gas of CO_2, with $\gamma = 1.30$ and $Pr = 0.72$. The free-stream Mach number is set to $M_\infty = 2$: this value is selected as corresponding to the deployment Mach number of the parachute, as well as being the most representative and critical supersonic case. In accordance with ExoMars database, the Reynolds number is based on the capsule diameter, D_0, and is set to $Re = 10^6$, corresponding to $M_\infty = 2$. Hence, normalized free-stream velocity and viscosity are fixed

$$u_\infty = \sqrt{\gamma} M_\infty \simeq 2.28 \tag{2.13}$$

$$\mu_\infty = \frac{\sqrt{\gamma} M_\infty}{Re} \simeq 2.28 \cdot 10^{-6} \tag{2.14}$$

The dynamic viscosity, $\mu = \mu(T)$, depends on the gas temperature and it is assumed to follow the *power-law* of a generalized fluid, while the heat transfer coefficient, $\lambda = \lambda(T)$, is obtained from Prandtl number definition. Respectively,

$$\mu = \mu_\infty T^{0.76} \simeq 2.28 \cdot 10^{-6} \cdot T^{0.76} \tag{2.15}$$

$$\lambda = \frac{\gamma}{\gamma - 1} \cdot \frac{\mu}{Pr} \simeq 1.37 \cdot 10^{-5} \cdot T^{0.76} \tag{2.16}$$

where all quantities are normalized using the respective reference quantities. We utilize the power-law dependence of viscosity because, in contrast to the Sutherland's law, allows simulations to be independent of the Sutherland's constant, which is not calibrated for Martian environment.

The Navier-Stokes equation in non-dimensional formulation (2.12) are discretized on a Cartesian grid, and solved with the in-house code STREAmS, which is described in the next section.

2.2 NUMERICAL APPROACH

STREAmS is a compressible flow solver developed by Bernardini et al. [34], 2021 at "La Sapienza" University of Rome. This solver implements advanced numerical methods based on finite-difference for Direct Numerical Simulation (DNS) of wall-bounded supersonic turbulent flows. However, employing a DNS approach is computationally prohibitive for our application: therefore, we utilize the Large Eddy Simulation (LES). The LES allows to capture the unsteadiness of the problem, which is caused by the capsule-released turbulent wake vortices, interacting with the bow shock ahead of the canopy. All this keeping the computational cost affordable.

LARGE EDDY SIMULATION

First step of a LES is the application of a low-pass filter to the Navier-Stokes equations. Filtering a generic variable, x, consists of decomposing it as $x = \overline{x} + x'$, where $\overline{x}$ is the *filtered* part (resolved), and x' is the *fluctuating* part (unresolved). In the present work, we adopt an *implicit* filtering: the grid itself acts as a filter, whose size is the grid-step, $\Delta = \sqrt[3]{\Delta x \Delta y \Delta z}$. This means that the LES solves directly on the grid only the turbulence scales bigger than Δ. For a compressible flow, it is convenient to express the flow variables in terms of Favre (or density-weighted) variables: a generic variable x is then decomposed as $x = \tilde{x} + x''$, where $\tilde{x} = \overline{\rho x}/\overline{\rho}$ is the density-weighted resolved part, and x'' is the unresolved part. Applying a spatial filter, $\overline{\bullet}$, to the equations 2.12, and exploiting the definition of the Favre filter, $\tilde{\bullet}$, we obtain the *filtered* Navier-Stokes equations in dimensionless form

$$\frac{\partial \overline{\rho}}{\partial t} + \frac{\partial (\overline{\rho}\tilde{u}_j)}{\partial x_j} = 0 \tag{2.17a}$$

$$\frac{\partial (\overline{\rho}\tilde{u}_i)}{\partial t} + \frac{\partial (\overline{\rho}\tilde{u}_i\tilde{u}_j)}{\partial x_j} + \frac{\partial \overline{p}}{\partial x_j} - \frac{\sqrt{\gamma}M_\infty}{Re} \cdot \frac{\partial \overline{\sigma}_{ij}}{\partial x_j} + \frac{\partial \overline{\tau}_{ij}^{SG}}{\partial x_j} = 0 \tag{2.17b}$$

$$\frac{\partial (\overline{\rho}\tilde{e})}{\partial t} + \frac{\partial (\overline{\rho}\tilde{e}\tilde{u}_j + \tilde{p}\tilde{u}_j)}{\partial x_j} - \frac{\sqrt{\gamma}M_\infty}{Re}\left[\frac{\partial (\overline{\sigma}_{ij}\tilde{u}_i)}{\partial x_j} - \frac{\gamma}{\gamma - 1} \cdot \frac{1}{Pr} \cdot \frac{\partial \tilde{q}_j}{\partial x_j}\right] + \frac{\partial \overline{e}_j^{SG}}{\partial x_j} = 0 \tag{2.17c}$$

where

$$\overline{\tau}_{ij}^{SG} = \overline{\rho}(\overline{u_i u_j} - \tilde{u}_i\tilde{u}_j), \qquad \overline{e}_j^{SG} = \overline{\rho e u_i + p u_i} - (\overline{\rho}\tilde{e}\tilde{u}_i + \overline{p}\tilde{u}_i). \tag{2.18}$$

The two terms 2.18 are, respectively, the sub-grid stress tensor and the sub-grid energy term. They represent the unresolved turbulent contributions arising from the filtering process, and they have to be modeled. Following Boussinesq's hypothesis, we can assume that the fluctuations of turbulence act in a dissipative way, similarly to the molecular viscosity. Traditionally, the effect of sub-grid stress tensor, $\overline{\tau}_{ij}^{SG}$, and sub-grid energy term, $\overline{e}_j^{SG}$, is take into account by introducing the concept of *eddy viscosity*, which is coupled through an external model to the resolved flow quantities.

IMPLICIT LARGE EDDY SIMULATION

The Navier-Stokes equations must be discretized to obtain their solution in terms of flow variables, which vary in both space and time. As we will see in the next section, spatial discretization is based on finite-difference methods. This type of discretization generates a numerical dissipation, whose effect is similar to that of the eddy viscosity: since this dissipation is not physical, it is referred to as *artificial viscosity*. The idea is to exploit the artificial viscosity to take into account the sub-grid turbulence contributions. Specifically, the discretization of convective terms is inherently characterized by low-pass filters, which provide an implicit sub-grid model, naturally coupled to the resolvable scales of the flow. By utilizing this implicit sub-grid model, conventional LES turbulence modeling is omitted. In the present work, we follow this approach, known as Implicit Large Eddy Simulation (ILES). The code STREAmS, therefore, solves the compressible Navier-Stokes equations in dimensionless form (2.12), without the addition of any external model.

2.3 SOLUTION PROCEDURES

To numerically obtain their solution, the Navier-Stokes equations must be discretized in both time and space domain, by approximating partial derivatives with *finite differences*: temporal derivatives became differences of values at successive instants of time, spatial derivatives became differences of values at adjacent grid nodes.

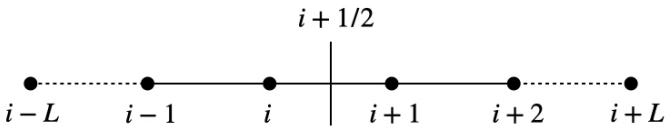

Figure 2.1: Schematic of the computational stencil in one space direction. In the present case, we set $L = 3$, meaning that the accuracy order of derivatives is $2L = 6$.

SPATIAL DISCRETIZATION

The convective terms in Navier-Stokes equations are discretized using a hybrid energy-conserving/shock-capturing scheme [34]. The energy-conserving formulation is based on a central sixth-order finite-difference scheme. If we call ϕ the transported quantity,[4] the convective flux in x direction is $f_x = \rho u \phi$. Considering the schematic in figure 2.1, the numerical discretization of the flux streamwise derivative at the i-th node is expressed as

$$\left.\frac{\partial f_x}{\partial x}\right|_i = \frac{1}{\Delta x}\left(\hat{f}_{x,i+1/2} - \hat{f}_{x,i-1/2}\right) \tag{2.19}$$

where Δx is the grid-step of the mesh, and $\hat{f}_{x,i+1/2}$ is the numerical flux at the intermediate node. The numerical flux can be written in a conservative formulation as

$$\hat{f}_{x,i+1/2} = 2\sum_{l=1}^{L} a_l \sum_{m=0}^{l-1} \left(\rho, \widetilde{u, \phi}\right)_{i-m,l} \tag{2.20}$$

4 $\phi = 1$ for mass equation, $\phi = u_j$ for momentum equation in the j-th direction, $\phi = e + p/\rho$ for energy equation.

where a_l are the standard coefficients for central finite-difference approximations of the first derivative, and $2L$ is the order of accuracy. In the present case, we set $2L = 6$. The two-point, three-variable discrete averaging operator is defined as

$$\left(\rho, \widetilde{u, \phi}\right)_{i,l} = \frac{1}{8}(\rho_i + \rho_{i+l})(u_i + u_{i+l})(\phi_i + \phi_{i+l}) \tag{2.21}$$

Central schemes are most accurate, but they are unable to describe shock waves, and can only be used in the smooth regions of the flow. In presence of shocks, STREAmS switches to generalized up-wind schemes. The locally conservative formulation allows direct hybridization of the central flux with classical shock-capturing reconstructions, which are based on Lax-Friedrichs flux splitting. The components of positive and negative characteristic fluxes are reconstructed at interfaces using a fifth-order Weighted Essentially Non-Oscillatory (WENO) scheme [35]. To judge on the local smoothness of the solution and switch between the two types of discretization, STREAmS relies on a modified version of the Ducros shock sensor

$$\theta = \max\left\{ \frac{-\nabla \cdot u}{\sqrt{\nabla \cdot u^2 + \nabla \times u^2 + u_0^2/l_0}},\ 0 \right\} \in (0, 1) \tag{2.22}$$

where u_0 and l_0 are reference velocity and length. The sensor is designed to be $\theta \approx 0$ in smooth flow regions, and $\theta \approx 1$ in presence of shock waves. Viscous terms are expanded to Laplacian form and approximated with sixth-order central schemes, avoiding odd-even decoupling phenomena. The numerical discretization of the spatial derivative in x direction of the viscous fluxes at the i-th node is

$$\left[\frac{\partial}{\partial x}\left(\mu \frac{\partial u}{\partial x}\bigg|_i\right)\right]_i = \frac{1}{\Delta x^2} \sum_{l=-L}^{L} \left(a_l^2 \mu_{i+l} u_{i+l} + \mu_i b_l u_{i+l}\right) \tag{2.23}$$

where b_l are the finite-difference coefficients for the second derivative of order $2L = 6$.

TIME INTEGRATION

From the discretization of spatial derivatives, we obtain a *semi-discrete* system of ordinary differential equations

$$\frac{\partial \mathbf{w}}{\partial t} = \mathbf{R}(\mathbf{w}), \qquad \mathbf{w} = [\rho, \rho u, \rho v, \rho w, \rho e] \tag{2.24}$$

Time integration relies on a three-stage, third-order Runge-Kutta scheme

$$\mathbf{w}^{(s+1)} = \mathbf{w}^{(s)} + \alpha_s \Delta t \mathbf{R}^{(s-1)} + \beta_s \Delta t \mathbf{R}^{(s)} \tag{2.25}$$

where $s = 0, 1, 2$ is the sub-step, $\mathbf{w}^{(0)} = \mathbf{w}^n$ is the solution at n-th step, $\mathbf{w}^{(3)} = \mathbf{w}^{n+1}$ is the solution at $(n+1)$-th step, $\alpha_s = (0, 17/60, -5/12)$ and $\beta_s = (8/15, 5/12, 3/4)$ are the integration coefficients [34].

2.4 INTERFACE MODELING

In the present simulation we consider a flow field developing around two solid bodies, capsule and parachute. No-slip and no-penetration Boundary Conditions (BCs) on solid surfaces can be imposed through different methods, among which an attractive choice is the Immersed Boundary Method (IBM).

IMMERSED BOUNDARY METHOD

The IBM, in fact, allows to cope with complex geometries reducing at the same time the computational cost (especially in the case of moving objects), since it removes the need to generate body-conforming meshes. The concept of IBM is that immersed bodies are discretized with grids that do not conform to their shape. Contrary to conventional approaches, the volume grid of the computational domain is generated with no regard to the immersed bodies, which are discretized with surface grids that cut through the volume grid, generating the solid boundaries [36]. Since the volume grid does not conform to the solid boundaries, it is necessary to add a *forcing term* to the Navier-Stokes equations at the fluid-solid interface, in order to incorporate the BCs.

Within IBM, two main groups can be distinguished: continuous forcing and discrete forcing methods. Continuous forcing methods consist in including in the Navier-Stokes equations a source term of body forces that mimic the presence of the solid body. This term is added to the equations before their discretization, leading to the *forced* Navier-Stokes equations

$$\frac{\partial}{\partial t}\begin{pmatrix}\rho\\ \rho u_i\\ \rho e\end{pmatrix}+\frac{\partial}{\partial x_j}\begin{pmatrix}\rho u_j\\ \rho u_i u_j+p\\ \rho e u_j+p u_j\end{pmatrix}-\frac{\partial}{\partial x_j}\begin{pmatrix}0\\ \sigma_{ij}\\ \sigma_{ij}u_i-q_j\end{pmatrix}=\begin{pmatrix}0\\ \rho f_i\\ \rho f_i u_i\end{pmatrix} \tag{2.26}$$

where we have temporarily returned to the dimensional formulation. The right-hand side of the equations system 2.26 is a source term containing the body forces; $f_i = f_i(x_i, t)$ is the specific force acting on the element of mimicked boundary. Continuous forcing methods are accurate and easy to implement, but they can only deal with Dirichlet conditions.[5] However, BCs in compressible flow problems are naturally specified as gradients of flow variables: this type of BCs are called Neumann conditions.[6] Thus, it is necessary to employ a discrete forcing method, which is able to deal with both Dirichlet and Neumann conditions [37]. Discrete forcing methods differ according to the imposition of the BCs, which can be direct or indirect. Indirect BCs imposition exploits a *force distribution function*, which introduces a spreading effect on interfaces. In simulations of high Reynolds number flows, where great accuracy is required on immersed surfaces, this spreading effect is undesirable.

GHOST POINT FORCING METHOD

Therefore, we utilize the Ghost Point Forcing Method (GPFM), which directly imposes BCs at the interface, allowing a sharp representation of the body surface. In the first place, the three-dimensional surface of embedded bodies must be discretized with triangular elements, unlike continuous forcing methods where is sufficient to

5 Dirichlet BCs impose that the solution, ϕ, is equal to a value fixed in space (time-varying only) at the boundary position, x_b : $\phi(x_b, t) = \phi_b(t)$.

6 Neumann BCs impose that the solution derivative, $\partial\phi/\partial x$, is equal to a value fixed in space (time-varying only) at the boundary position, x_b : $\partial\phi(x_b, t)/\partial x = \partial\phi_b(t)/\partial x$.

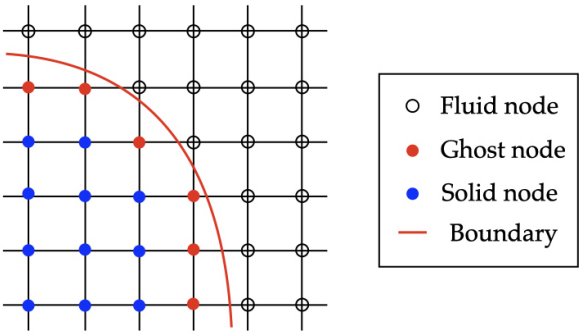

Figure 2.2: Two-dimensional schematic illustration of the Ghost Point Forcing Method (GPFM), where the three categories of grid nodes are highlighted.

set a collection of Lagrangian points. In the present work, the shape of immersed bodies is provided through triangulated surfaces in Stereolithography (STL) format. Subsequently, we proceed with the imposition of BCs on the surface: this is implemented through the use of *ghost cells*, i.e. cells in the solid that have at least one neighbor in the fluid. The category of a cell is identified from the related grid nodes, as illustrated in figure 2.2. A ghost region is thus created adjacent to the immersed boundary: ghost nodes within the ghost region must be as many as required by the accuracy order of finite-difference scheme utilized in the solver. Since in this work we employ sixth-order schemes, the number of ghost nodes is six.

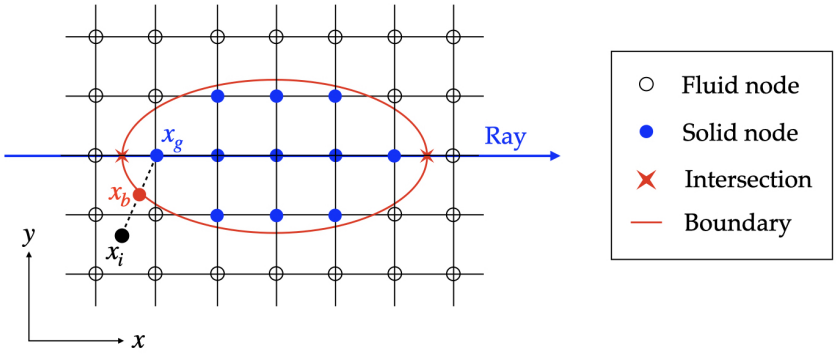

Figure 2.3: Sketch of ray tracing algorithm and grid nodes classification. The node x_g is a *ghost* point, x_b and x_i are its related *boundary* point and *image* point.

The algorithm needs to discern if a computational node is a fluid, a solid, or a ghost one. To this purpose, an automatic solid-detection technique based on a *ray tracing algorithm* is employed. To reduce the computational load, we assume the class of rays coincident with the coordinate axis (e.g. x axis in the sketch of figure 2.3). By computing the intersections of each ray with the surface, it is possible to tag all grid nodes lying on that ray: if the number of intersections on the left of each node is odd (even), the node is solid (fluid). Once the fluid nodes are located, we identify the subset of nodes for which the discretization of the Navier-Stokes equations involves the use of solid nodes: these are tagged as *ghost* points [38]. Referring to figure 2.3, for each ghost point, x_g, a correspondent *boundary* point, x_b, and *image* point, x_i (lying in the flow region), can be determined. Flow variables at the image point, $\phi(x_i)$, are computed from the surrounding fluid nodes through an interpolation procedure. Finally, Boundary Conditions (BCs) are enforced in the correspondent ghost point by reflecting the value at the image point, $\phi(x_i)$.

2.5 SIMULATION SETUP

The structure examined in this work, shown in figure 2.4, is based on ESA's ExoMars 2022 mission. It consists of a capsule (on the left side of the figure) and a parachute canopy (on the right). The two bodies are considered fixed in space, and a rigid-canopy model has been employed, for the reasons explained in section 1.6.

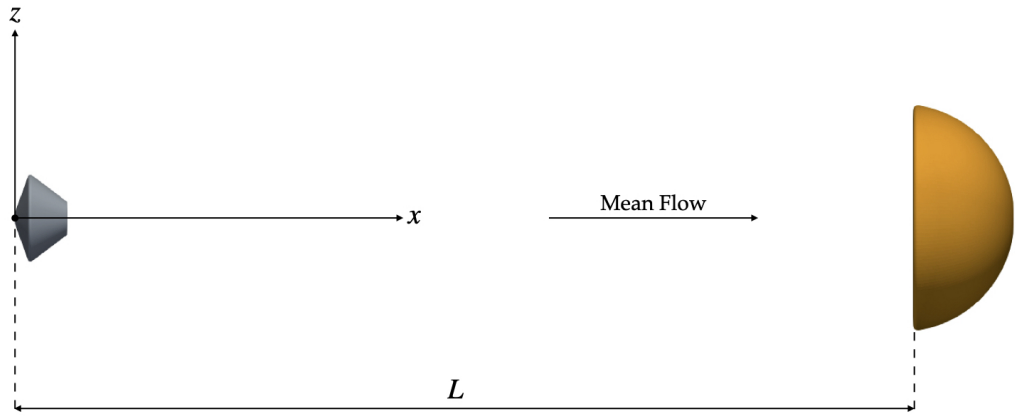

Figure 2.4: Two-dimensional view of the overall simulation setup (x, z plane). Trailing distance, L, is measured from the capsule tip to the parachute leading edge.

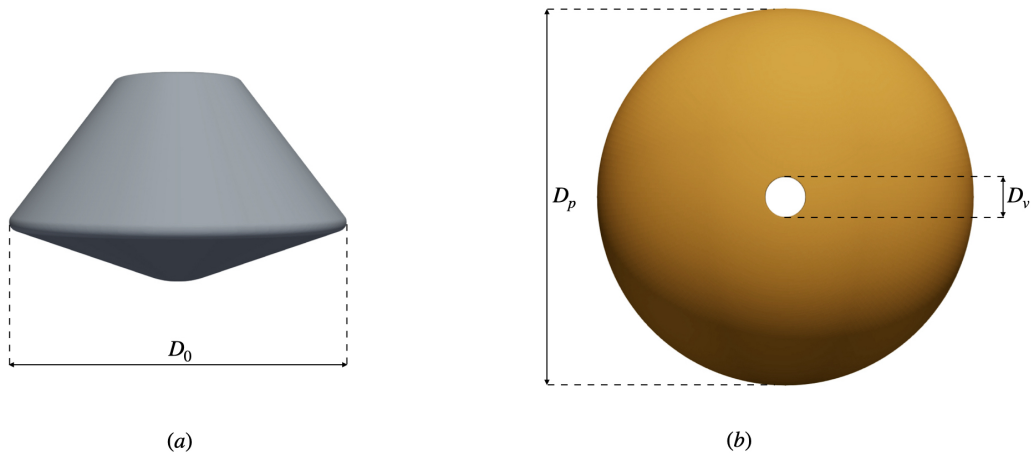

Figure 2.5: Representation (not to scale) of the capsule (a) and the parachute (b), with specification of the dimensions of interest.

The reference coordinate system is centered at the capsule nose, and x axis coincides with the capsule-parachute symmetry axis (mean direction of the flow). Suspension lines are not considered in this study.[7] Nevertheless, the effect of suspension lines on the general behavior of the flow can be considered negligible.

7 As seen in paragraph 2.4, the GPFM simulates the presence of solid bodies through a surface ghost region. In this work, we utilize 6 ghost nodes within the ghost region (in accordance with the accuracy order of the finite-difference scheme), which are used to impose the BCs at the interface. If the object is smaller than the ghost region, it can not be simulated, as in the case of cables. For a detailed study of the effect of parachute cables we refer to Xue et al. [30], 2015.

CONFIGURATION OF THE EMBEDDED BODIES

The capsule, shown in figure 2.5 (a), is a scaled version of ExoMars 2022 descent module. It is a sphere-cone entry vehicle, whose original dimensions are quoted in figure 2.6a: maximum diameter is $D_0 = 3.8m$, height is $2.4m$, front-shield half-angle is 70°. In figure 2.6b is represented the capsule discretization, ready to be written as STL file and imported in STREAmS. The capsule maximum diameter is used as reference length, $l_0 = D_0$. All dimensions are normalized with respect to D_0, i.e. divided by $3.8m$. Thus, the normalized capsule diameter is unitary. The distance from the capsule tip to the parachute leading edge (i.e. its leftmost edge in figure 2.4) is called *trailing distance*, L. In the present work, the normalized trailing distance is $L = 10$. This value has been chosen lower than that designed for ExoMars 2022, equal to $1.5 \cdot L$, in order to increase the distance between canopy and outflow, avoiding perturbations of the flow behavior in the parachute wake region, due to the imposition of outflow conditions.

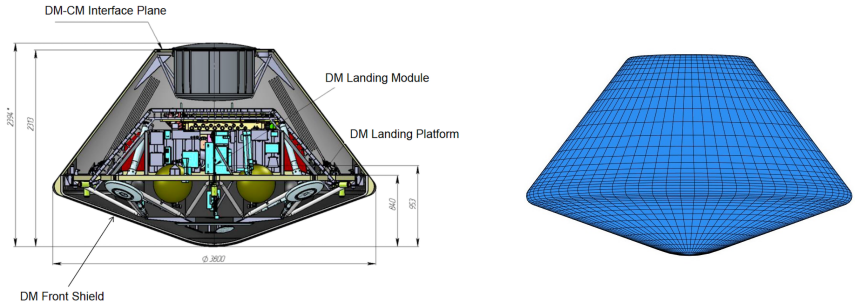

Figure 2.6: Design parameters (a) and discretization (b) of the descent module.

The considered parachute is shown in figure 2.5 (b). It has a hemispherical shape cut by the back hole (*vent*) and, unlike classic DGB, it is designed without a band. As noted above, the supersonic parachute dynamics is characterized by the *breathing cycle*, a phenomenon that strongly affects drag and stability. This phenomenon is emphasized by the absence of the band, whose nominal purpose is precisely to limit the effects of breathing. Therefore, we decided to simulate a parachute without a band, with the aim of highlighting driving mechanism of parachute breathing. The nominal diameter[8] of the supersonic parachute for ExoMars 2022 mission is $D_0 = 15m$. Assuming the typical *inflation ratio* of a DGB parachute, $D_p/D_0 = 0.65$ [40], the diameter of the inflated canopy results $9.75m$. Hence, the normalized parachute diameter, reported in figure 2.5 (b), is $D_p = 2.57$, while the normalized diameter of the vent is $D_v = 0.26$. For the same reason that led us to neglect suspension lines, the parachute was designed with an increased thickness of 0.12 (in dimensionless terms), and with a rounded leading edge.

CONFIGURATION OF THE COMPUTATIONAL DOMAIN

A sketch of the full computational domain is shown in figure 2.7. The origin of the coordinate system is centered at the capsule tip; dimensionless coordinates of the domain are $[-1, 19] \times [-5, 5] \times [-5, 5]$; its dimensions are $L_x = 20, L_y = 10, L_z = 10$; the number of grid nodes in the three directions are $N_x = 2560, N_y = 840, N_z = 840$.

8 The nominal diameter, D_0, is fictitious diameter obtained by assuming that the nominal area of the parachute is that of a circle. The ratio between the projected diameter, D_p, of the inflated parachute and its nominal diameter, D_0, is called inflation ratio [39].

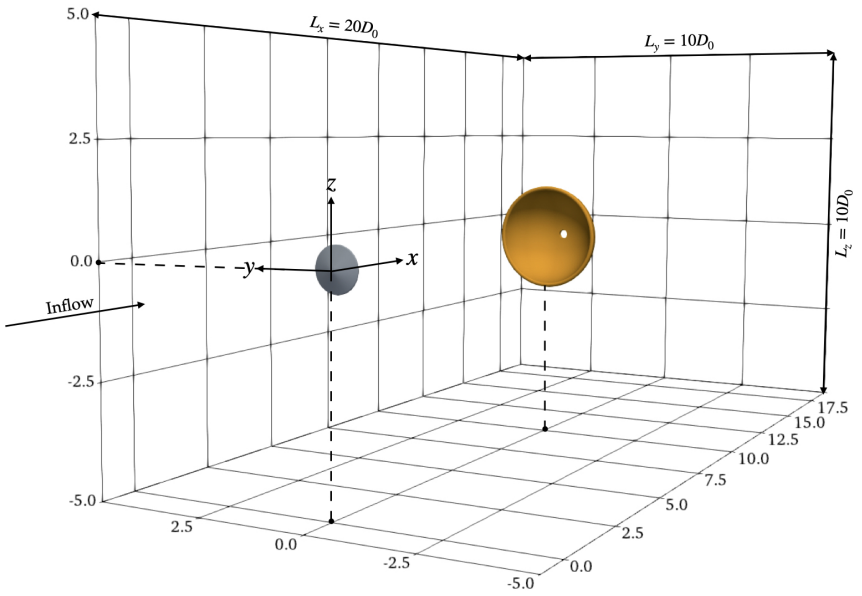

Figure 2.7: Three-dimensional representation of the full computational domain.

The structured grid is stretched or compressed according to local requirements: flow regions near the solid bodies are provided with the finest resolution, to better describe the fluid-solid interaction. Considering x direction, capsule and canopy regions have a *contraction factor* of 0.2, meaning that the grid-step is equal to $0.2\Delta_0$, where $\Delta_0 = L_x/N_x$ is the reference value of the grid-step. The spatial gradient of the grid density is quantified by the *fade*: a low value of fade indicates sharp variation, a high value indicates smooth variation. Grid-step varies from Δ_0 to $0.2\Delta_0$ sharply in front of the bodies (fade = 0.05), while smoothly behind the bodies (fade = 0.4). Indeed, bow shocks are in proximity to the bodies, while the turbulent wake, which requires fine resolution, extends over a long distance behind the bodies. The refinement along y and z directions ensures that the region around the symmetry axis has the finest resolution: along both y- and z-axis, contraction factor is 0.3 and fade is 0.2, symmetrical with respect to x-axis.

Inlet condition is set on the frontal wall, with uniform flow along x direction and free-stream quantities defined in section 2.1. On all other walls, *non-reflective* outlet conditions are imposed, so as not to perturb the outflow behavior.

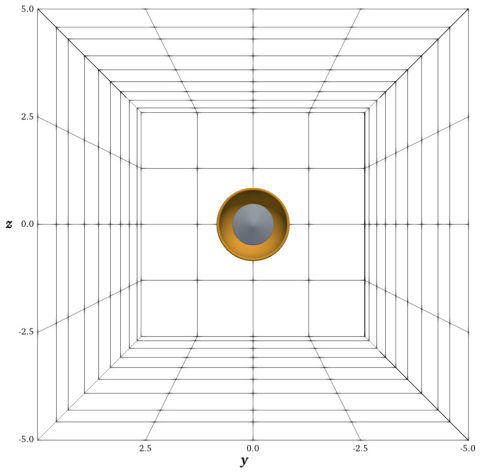

Figure 2.8: Frontal representation of the computational domain (y, z plane).

3 SIMULATION RESULTS

3.1 INSTANTANEOUS FIELDS

The three-dimensional structure presented in paragraph 2.5 is placed in a compressible supersonic flow, going from left to right of figure 2.4. Simulations are performed on CINECA's Marconi100 cluster, allowing the parallelization of the domain on 32 GPUs. We ran the simulation for a normalized time of $t = 60$, corresponding to 14 *flow times*, so that the initial transients dissipate and the flow reaches its natural state. The flow time is defined as the ratio of the trailing distance to free-stream velocity [27], $t_x = L/u_\infty = 4.39$. The reference time used for the normalization is defined as $t_0 = l_0/u_0 = \sqrt{\gamma} D_0/a_\infty$, where the free-stream speed of sound is equal to $a_\infty = 235.40 ms^{-1}$, obtained from ExoMars database. Hence, dimensional time of simulation is $1.1s$. Considering an auxiliary simulation to observe the flow behavior without the capsule, the total cost required was about 5 days. Since the system is axisymmetric, simulation results can be easily visualized extracting two-dimensional "slices" on the x, z central plane, which cuts the domain at $y = 0$.

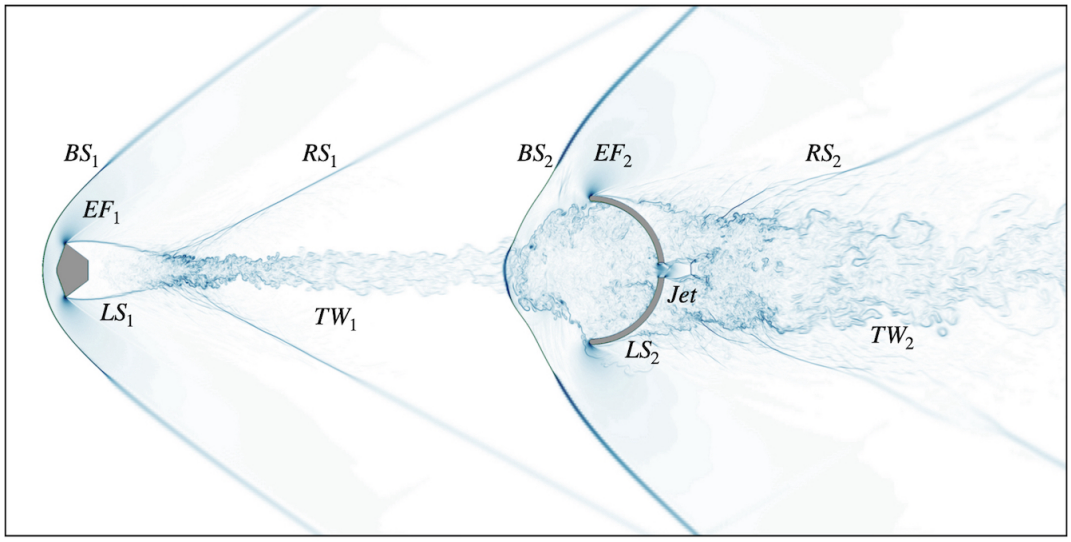

Figure 3.1: Instantaneous field of numerical Schlieren, showing canonical flow regions.

The compressible flow over the parachute-capsule system can be apportioned into some canonical regions, which can be clearly identified by computing the numerical Schlieren. This quantity is used to emphasize density gradients, and is defined as

$$Schlieren = \exp\left(-\frac{5|\nabla\rho|}{\max|\nabla\rho|}\right), \qquad |\nabla\rho| = \sqrt{\left(\frac{\partial\rho}{\partial x}\right)^2 + \left(\frac{\partial\rho}{\partial z}\right)^2}. \tag{3.1}$$

where ρ is the density of the gas. In figure 3.1 is shown the instantaneous field of numerical Schlieren at $t = 60$. We observe the generation of two *bow shocks*, BS_1 and BS_2, respectively ahead of the capsule and the canopy. These shocks are responsible for adjusting the supersonic flow conditions upstream of the solid boundaries of the

bodies. The capsule bow shock is steady, as well as the subsonic region between the shock and the capsule. At the capsule shoulder generates the *lip shock*, LS_1, separating the outer supersonic flow from the inner subsonic flow. The outer flow accelerates as it turns around the capsule shoulder through an expansion fan, EF_1, and it is then reconciled to free-stream conditions by the *recompression shock*, RS_1. The inner flow behind the capsule develops in a narrow turbulent wake, TW_1, which is quite stable.

A similar structure can also be identified in the canopy region, although the flow is clearly more unstable. Source of this instability is the *turbulence-shock* interaction, occurring when the capsule wake, TW_1, reaches the canopy bow shock, BS_2. The intensity of turbulence carried by the wake is amplified as the flow travel across BS_2, which *ingests* the turbulence leading to large fluctuations of momentum and pressure. In addition, being disrupted by the irregularities of the wake, the canopy bow shock does not reach a steady state, and shows an oscillatory motion. This motion is related to the parachute *breathing cycle*, which is evident regardless the parachute rigidity. At the canopy leading edge is visible the expansion fan, EF_2, and the lip shock, LS_2, despite being less sharp due to the instability of the flow. We also observe the supersonic *jet* leaving the vent at the back of the canopy, where the flow reaches its maximum velocity. Finally, behind the canopy is visible a large turbulent wake, TW_2, from which originates the recompression shock, RS_2, that rectify the oblique flow direction just behind the canopy structure with the free-stream direction.

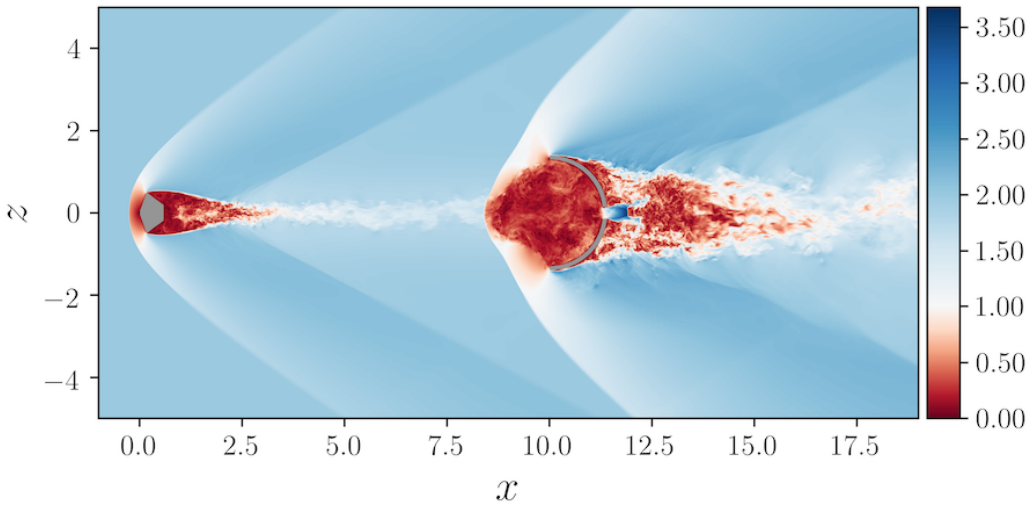

Figure 3.2: Instantaneous field of the Mach number at $t = 60$.

In figure 3.2 is shown the instantaneous field of the Mach number at $t = 60$. Supersonic flow regions (in blue), sonic regions (in white) and subsonic regions (in red) can be identified. We can see subsonic regions behind the two bow shocks; these regions are concentrated around the axis of symmetry, where the shock is stronger as its inclination angle with respect to the inflow is smaller. The high Reynolds number of the flow, $Re = 10^6$, results in the generation of an extended wake behind the capsule: near wake is characterized by subsonic recirculation regions, while far wake is in low-supersonic conditions. After interacting with the canopy bow shock, the flow develops into vortical structures both inside the canopy and at its back, producing large subsonic regions. The highest velocity is reached by the flow exiting the vent, with a Mach number of $M \simeq 3.6$.

Instantaneous fields of density and pressure are respectively shown in figures 3.3a and 3.3b. We note that peaks of density ($\rho_{max} \simeq 3.4\rho_\infty$) and pressure ($p_{max} \simeq 5.2p_\infty$)

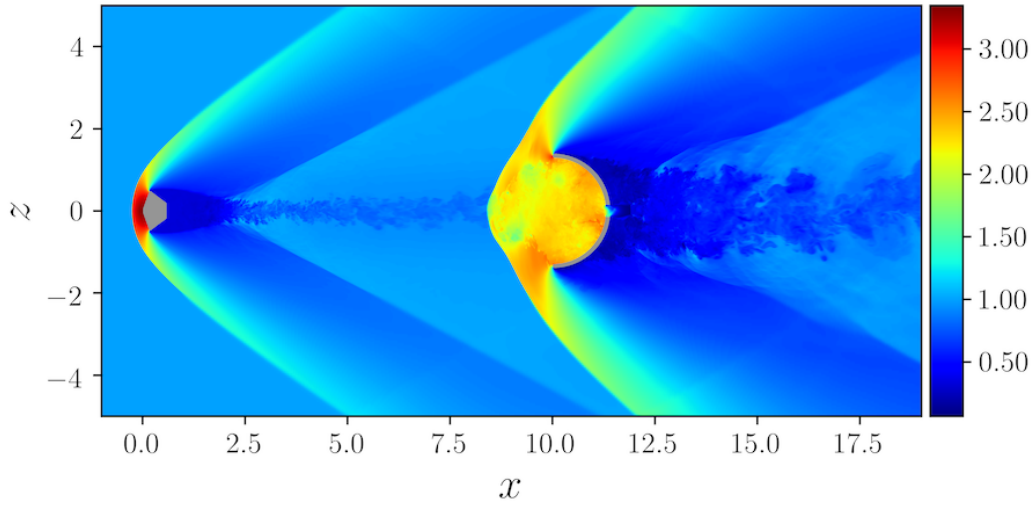

(a) Density

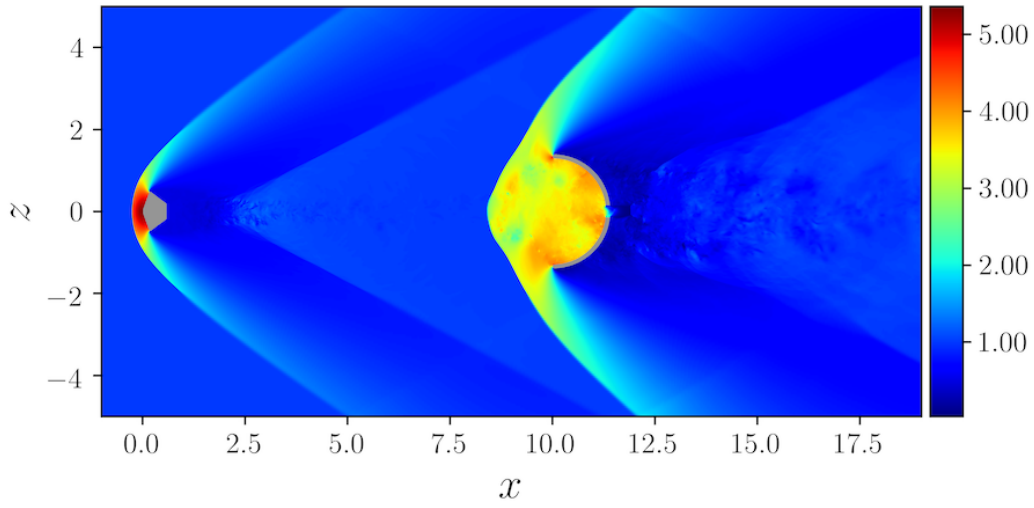

(b) Pressure

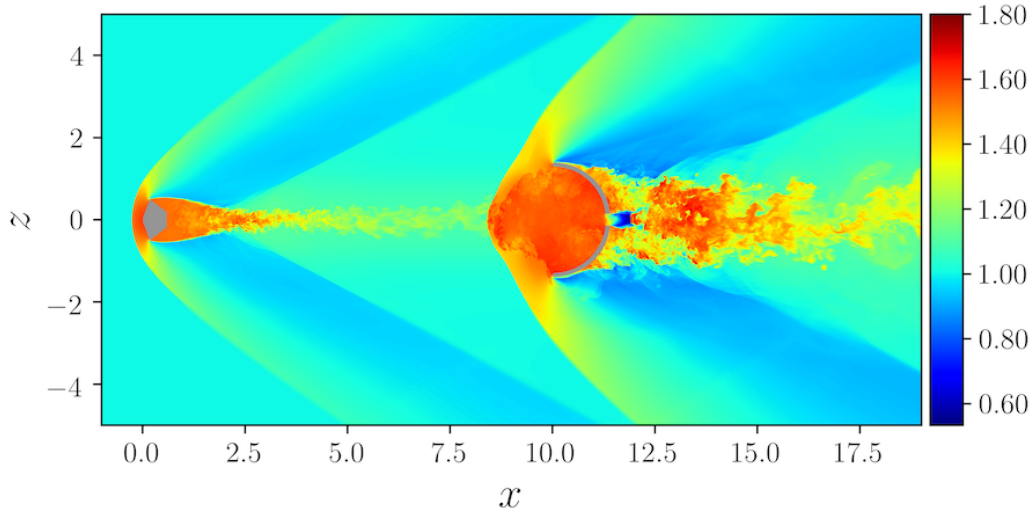

(c) Temperature

Figure 3.3: Instantaneous fields of density, pressure, temperature at $t = 60$. All quantities are normalized with respect to the corresponding free-stream values.

are reached in the subsonic region between the first bow shock and the capsule. The flow region within the canopy is also characterized by high density and pressure (in orange), which are unevenly distributed on the canopy inner surface. The temperature field is shown in figure 3.3c, where we see that temperature peaks ($T_{max} \simeq 1.8T_\infty$) are reached by the flow just after both the bow shocks, as well as in both wakes. We also note the low temperature of the accelerating flow in between the bow shock and the recompression shock, both in capsule and canopy regions, and the minimum value of temperature ($T_{min} \simeq 0.6T_\infty$) characterizing the supersonic jet leaving the vent.

Another relevant flow property is the vorticity, ζ, defined as the curl of the velocity

$$\zeta_i = \nabla \times u_i \tag{3.2}$$

Through Crocco's theorem, it is possible to show that a non-homoentropic flow is a rotational flow, i.e. $\zeta \neq 0$. As the flow passes through the bow shock, the entropy increase by an amount which depends on the local strength of the shock, variable according to its local slope. Therefore, an initially irrotational flow will acquire vorticity proportional to the entropy gradient generated by the bow shock [41].

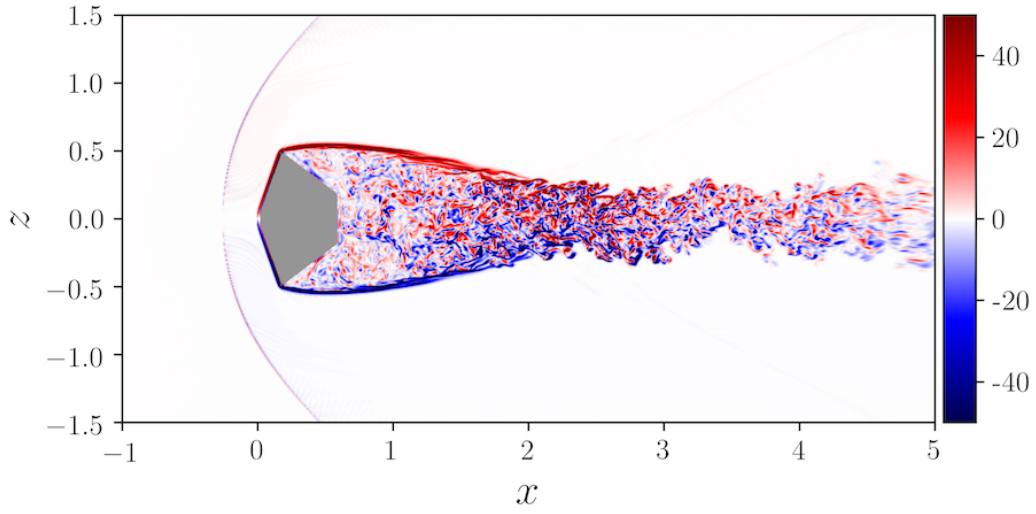

(a) Capsule region

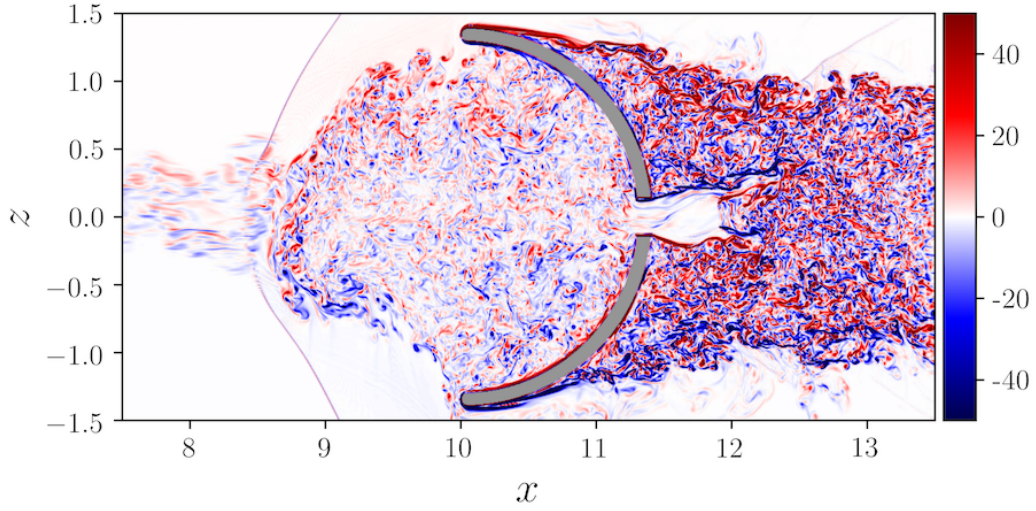

(b) Canopy region

Figure 3.4: Instantaneous field of the vorticity component along y direction at $t = 60$.

In figure 3.4 is shown a snapshot of the vorticity field, focusing on the regions of capsule (3.4a) and canopy (3.4b). Since we are utilizing two-dimensional slices on the central x, z plane, we are visualizing the y component of the vorticity

$$\zeta_y = \frac{\partial u}{\partial z} - \frac{\partial w}{\partial x} \tag{3.3}$$

The high intensity of vorticity on the capsule heat shield indicates the presence of a boundary layer, which detaches at the shoulder generating a free-shear layer and, further downstream, the near-wake vortical structures (3.4a). Free-shear layers also originate from the canopy leading edge and vent (3.4b). Specifically, at the vent section the flow is sonic; pushed by the high pressure within the canopy and finding a larger passage section,[1] it rapidly accelerates to the highest Mach number of the field. In a small distance, the supersonic flow runs into the canopy wake, characterized by high-vorticity turbulent structures, and its Mach number sharply drops. The interface between vortical structures and supersonic jet seems to be affected by the presence of *eddy shocklets*. Shocklets generate around coherent eddies that have sufficiently large spatial and temporal scales, and are visible at supersonic Mach number and high Reynolds number. All these conditions are found in this case, leaning toward a confirmation of the presence of eddy shocklets. In their proximity exists an energy transfer mechanisms, known as *pressure dilatation*, which accelerates the conversion of turbulent kinetic energy into internal energy [42]. The effect of this mechanism will be appreciated in the next section, through the analysis of mean fields.

3.2 TIME-AVERAGED FIELDS

After the analysis of the instantaneous fields, we proceed with statistical analysis. A generic variable, $u(x_j, t)$, can be decomposed as

$$u(x_j, t) = \overline{u}(x_j) + u'(x_j, t) \tag{3.4}$$

where $\overline{u}(x_j)$ is the time-average, while $u'(x_j, t)$ is the fluctuating part. In this section, we concentrate on time-averaged (or *mean*) quantities. Considering a time window $\Delta t = t_f - t_i$, the time-average of $u(x_j, t)$ is defined as

$$\overline{u}(x_j) = \frac{1}{\Delta t} \int_{t_i}^{t_f} u(x_j, t)\, \mathrm{d}t \tag{3.5}$$

Since the time-step has a finite value, the integral becomes a sum. Statistical quantities should be computed since the flow is fully developed, ensuring that they are not affected by initial transients. Therefore, statistics are computed from $t_i = 40$ to $t_f = 60$, after 9 flow times ($t_x = L/u_\infty = 4.39$).

In figure 3.5 is represented the mean field of the Mach number. Regions where the flow is sonic (red lines) and where the flow recovers free-stream conditions (blue lines) are emphasized. The sonic isoline encloses the region between the shock and the solid body as well as the near wake, for both capsule and canopy. We also note that the vent section is averagely in sonic conditions: we could then associate the canopy with a convergent nozzle with a chocked outflow, where the *throat* section is the vent. This analogy will be explored in the following. Different isolines corresponding to $M = 2$ are visible: the one originating from the capsule shoulder captures the

1 In general, a supersonic flow accelerates as the passage cross section increases.

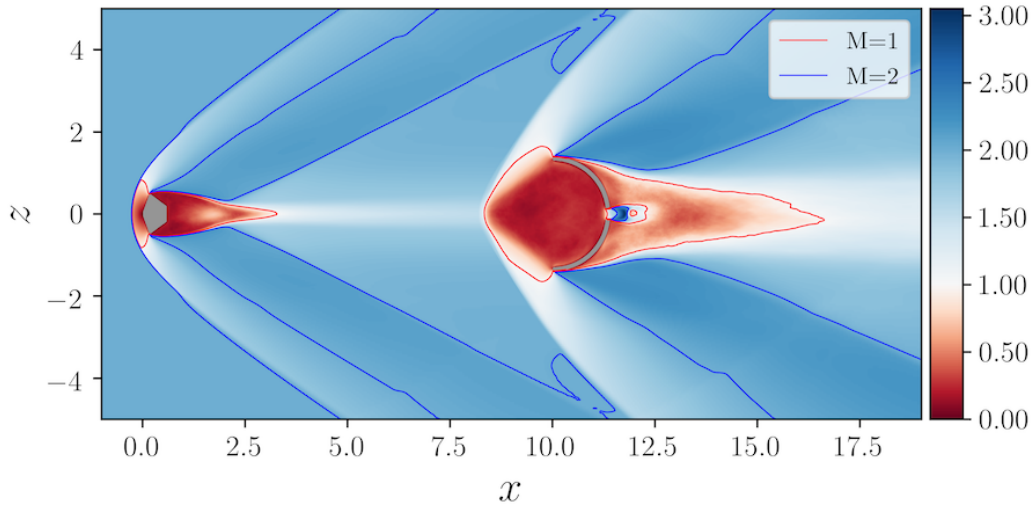

Figure 3.5: Mean field of the Mach number. The red isoline corresponds to $M = 1$, the blue one to $M = 2$.

accelerating flow right after the expansion fan; the one further downstream is located in correspondence with the recompression shock, indicating that the flow has actually been restored to the free-stream conditions. The same applies for the blue isolines in the canopy region, one originating from the canopy leading edge, and the other at the recompression shock.

Mean fields of density, pressure and temperature are respectively shown in figures 3.6a, 3.6b and 3.6c. A relevant note is that the subsonic region between the first bow shock and the capsule, highlighted in figure 3.5 by the red isoline, is where density, pressure and temperature are highest, with maximum values right at the capsule nose. As expected, the heat shield is subject to the most severe conditions, especially due to the high temperatures. The flow region within the canopy is also characterized by high values of density (in orange/yellow), pressure (in yellow) and temperature (in red). As far as the wake regions are concerned, we note that mean density and pressure have low values, while the temperature is high in both wakes, except for the cold jet that leaving the vent.

ONE-DIMENSIONAL ANALYSIS OF MEAN QUANTITIES

A more quantitative analysis can be made by considering the spatial trend of mean quantities computed along the symmetry axis, i.e. x-axis, as shown in figure 3.7. The symmetry axis is the most representative, as it crosses the bow shocks in normal direction, plus it captures the central part of the wake and the jet leaving the vent. The location of the capsule bow shock is highlighted in all graphs of figure 3.7: at $x = -0.3$ we see the maximum gradient of the analyzed quantities, corresponding to the shock location. By looking at graphs 3.7a, 3.7b and 3.7c, we note that density, pressure and temperature continue to increase after the capsule shock, reaching their peaks at $x = 0.0$, i.e. at the capsule tip. As for Mach number, shown in graph 3.7d, it rapidly drops to zero after the capsule shock, and then increases until $x \simeq 8.5$, i.e. the location of the canopy bow shock, where drops again. Once the canopy is traversed, the Mach number reaches its peak of $M = 3.1$ at $x \simeq 11.8$, where the flow leaves the vent. Shortly after, as the flow runs into the canopy wake, the Mach number sharply decreases to $M = 0.4$ at $x \simeq 13.1$. At the same location, there is a great increase in temperature. These trends seems to confirm the energy transfer mechanism by

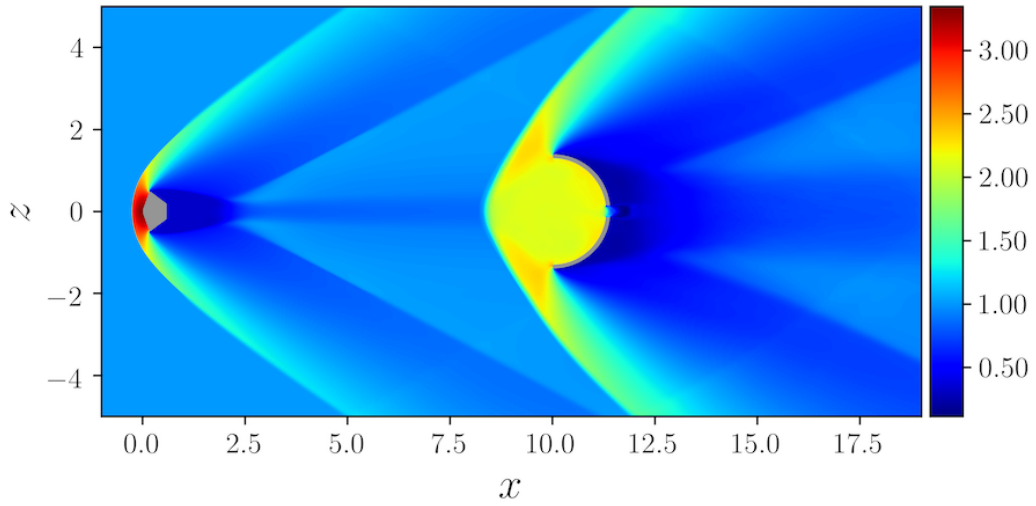

(a) Density

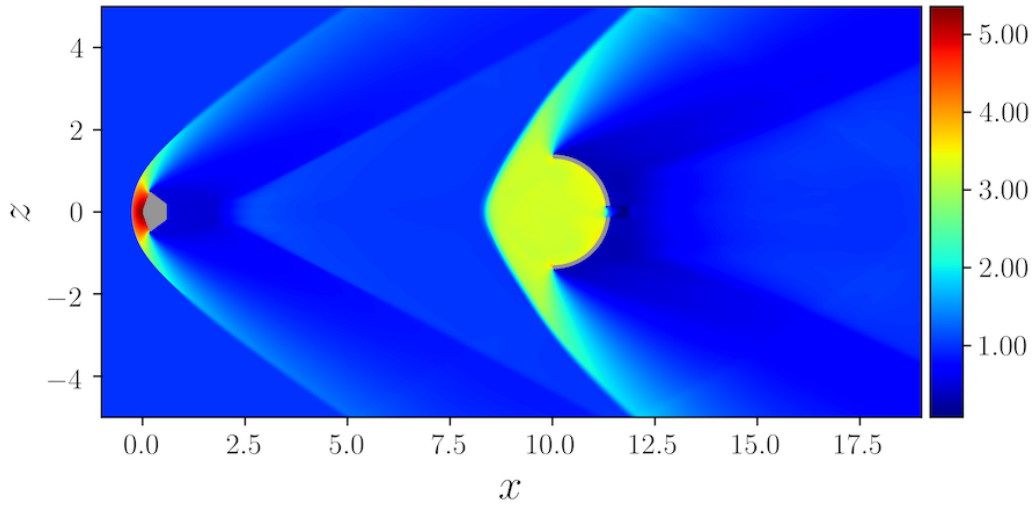

(b) Pressure

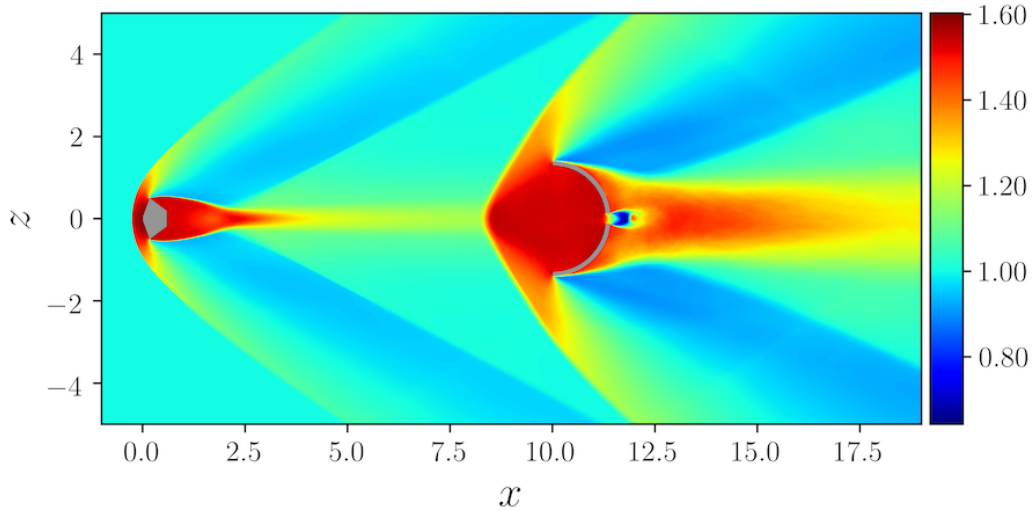

(c) Temperature

Figure 3.6: Mean fields of density, pressure, temperature. All quantities are normalized with respect to the corresponding free-stream values.

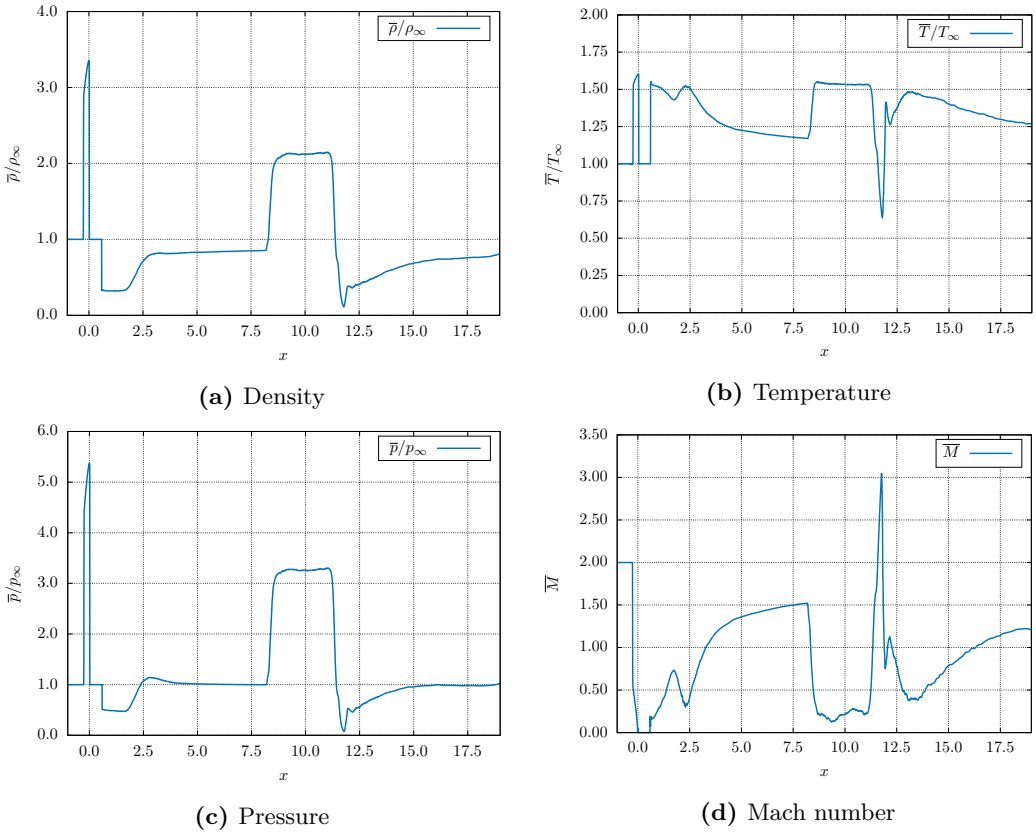

(a) Density **(b)** Temperature

(c) Pressure **(d)** Mach number

Figure 3.7: Mean quantities computed along the symmetry axis.

eddy shocklets, identified in section 3.1. In fact, Mach number is associated to kinetic energy, $E_{kin} \sim u^2 \sim M^2$, which is converted into internal (or *thermal*) energy.

Another reason motivating the one-dimensional analysis is that the the streamline along the symmetry axis crosses both shocks in normal direction. Therefore, we can compute the value of flow variables downstream of the shocks employing the *normal shock relations*, in order to have a yardstick through which we can assess the simulation results. As we will see in chapter 4.2, the normal-shock assumption will be employed to develop an analytical model describing the turbulence-shock interaction. By assuming that normal shocks are adiabatic (but non-isentropic), the normal shock relations analytically provide the ratio between downstream and upstream value of flow variables, $\bullet_2/\bullet_1$. All equations, listed below, are functions of M_1 only.

$$\textit{Normal shock relations} \quad \begin{cases} M_2^2 = \dfrac{1 + M_1^2(\gamma-1)/2}{\gamma M_1^2 - (\gamma-1)/2} \\ \dfrac{\rho_2}{\rho_1} = \dfrac{(\gamma+1)M_1^2}{2 + (\gamma-1)M_1^2} \\ \dfrac{p_2}{p_1} = 1 + \dfrac{2\gamma}{\gamma+1}\left(M_1^2 - 1\right) \\ \dfrac{T_2}{T_1} = \dfrac{p_2}{p_1} \cdot \dfrac{\rho_1}{\rho_2} \end{cases} \tag{3.6}$$

Upstream values	*Analytical values*	*Simulated values*
$M_1 = 2.00$	$M_2 = 0.56$	$M_2 = 0.56$
$\rho_1 = 1.00$	$\rho_2 = 2.88$	$\rho_2 = 2.87$
$p_1 = 1.00$	$p_2 = 4.39$	$p_2 = 4.39$
$T_1 = 1.00$	$T_2 = 1.53$	$T_2 = 1.53$

Table 3.1: Analytical and simulated values of flow variables downstream of the capsule bow shock. Upstream values are computed from the simulation at $x = -1, y = 0, z = 0$.

We can now compute the analytical values via the relations 3.6, and compare them with the mean values provided by the simulation. Simulations results are shown in figure 3.7, where we report the trend of mean quantities along x-axis. As for the capsule bow shock, upstream quantities coincide with free-stream quantities, and are computed at the inflow, i.e. at $x = -1.0$. Referring to the graphs of figure 3.7, the capsule tip is located at $x = 0.0$, while the capsule bow shock at $x = -0.3$, where simulated values are computed. These are listed in table 3.1, along with the analytical ones provided by normal shock relations (3.6). From the table we can appreciate the excellent match between simulated and analytical values.

Upstream values	*Analytical values*	*Simulated values*
$M_1 = 1.50$	$M_2 = 0.69$	$M_2 = 0.22$
$\rho_1 = 0.85$	$\rho_2 = 1.65$	$\rho_2 = 2.08$
$p_1 = 1.00$	$p_2 = 2.42$	$p_2 = 3.20$
$T_1 = 1.17$	$T_2 = 1.47$	$T_2 = 1.54$

Table 3.2: Analytical and simulated values of flow variables downstream of the canopy bow shock. Upstream values are computed from the simulation at $x = 7.5, y = 0, z = 0$.

As for the canopy bow shock, upstream conditions correspond to the capsule far wake, just before interacting with the shock. Specifically, they are computed from simulated mean quantities at $x = 7.5$, and they are used to calculate the analytical values through the relations (3.6). Simulated values of flow variables downstream of the canopy shock can be graphically derived from figure 3.7 at $x = 8.3$, which is the mean downstream location. Analytical and simulated values downstream of the canopy bow shock are listed in table 3.2, as well as simulated upstream values. In this case, analytical values do not precisely match with the simulation results, although being the same order of magnitude. Simulated flow variables are slightly higher compared to the analytical ones, except for the Mach number that is lower. This mismatch is explained by the fact that, unlike the steady capsule shock, the canopy shock is highly unsteady, as it is disrupted by the fluctuations of both the incoming turbulent wake and the vortical structures forming within the canopy. This instability is related to the parachute *breathing cycle*, which distorts the shape of the canopy bow shock. Moreover, since the upstream flow is turbulent, its mean direction is not perfectly straight. These two factors partially invalidate the normal-shock assumption along the symmetry axis.

The assessment of this instability and the location of regions where the flow is most variable can be done by fluctuation analysis, as we will see in the next section.

3.3 FLUCTUATING FIELDS

We proceed with the statistical analysis, aimed now at assessing the flow variability in terms of fluctuations. Recalling that a generic variable can be decomposed as $u(x_j,t) = \overline{u}(x_j) + u'(x_j,t)$, we focus on the fluctuating part, $u'(x_j,t)$. By definition, the time-average of fluctuations is zero, but its variance (or *mean square*) is not zero. The intensity of fluctuations is generally quantified by the Root Mean Square (RMS) of the fluctuating part, defined as

$$u_{rms} = \sqrt{\overline{(u')^2}} = \sqrt{\frac{1}{\Delta t}\int_{t_i}^{t_f} (u-\overline{u})^2 \, \mathrm{d}t} \tag{3.7}$$

where $\Delta t = t_f - t_i$ and, as for mean fields, $t_i = 40$ and $t_f = 60$. In figure 3.8 are shown the RMS fields of density, pressure and temperature fluctuations. We can see that the capsule bow shock is perfectly steady, as fluctuations are absent. Within the capsule wake, the amplitude of fluctuations is limited, indicating that the wake is quite stable, as well as the recompression shock. As expected, peaks of density and pressure fluctuations are located at the canopy bow shock (red regions in figures 3.8a and 3.8b). Being perturbed by the capsule wake, the bow shock is affected by an oscillatory dynamics involving a periodic motion along the symmetry axis, which is reflected in high fluctuations. This motion, visible throughout the simulation, shows a roughly regular pattern after the initial transient, and is related to the parachute *breathing cycle*, as we will see in section 3.4. From figure 3.8c, we see that the vent outflow shows the maximum amount of temperature fluctuations. We suppose that this high temperature variability is related to the *pressure-dilatation* mechanism involved in that region, discussed above.

In figure 3.9 are shown the RMS fields of velocity fluctuations. Fluctuations in the three directions are present in both capsule and canopy wake, with higher values along x direction, especially at the free-shear layers generating from the canopy leading edge and vent (figure 3.9a). We also note that x- and z-component of velocity fluctuations are intense at the canopy bow shock, where, instead, the y-component is absent. This is explained by the fact that the tangential component of the velocity, v, remains unchanged as the flow traverses the shock and, thus, is not affected by the shock instability. Conversely, since the two velocity components u and w are modified by the shock, they are affected by its instability, and show high variability.

To quantify the intensity of turbulence, it is usually employed the Turbulent Kinetic Energy (TKE), indicated with k and defined as

$$k = \frac{1}{2}(u_{rms}^2 + v_{rms}^2 + w_{rms}^2) \tag{3.8}$$

This quantity can be normalized with the specific kinetic energy of the mean flow, K

$$K = \frac{\overline{E}_{kin}}{\overline{\rho}} = \frac{1}{2}(\overline{u}^2 + \overline{v}^2 + \overline{w}^2) \tag{3.9}$$

In figure 3.10a is shown the TKE field normalized with $K_\infty = 0.5u_\infty^2$ (since $v_\infty = w_\infty = 0$). We note that its peak is at the interface between the vent outflow and the canopy wake, where is equal to $k_{max} \simeq 26\% K_\infty$. It is also meaningful to normalize the TKE with the *local* value of K. This field is shown in figure 3.10b, from which we see the strong intensity of turbulence in both wakes and within the canopy: as the mean velocity decreases in these regions, the TKE is consequently emphasized. We can also note that the vent outflow is free from turbulent structures.

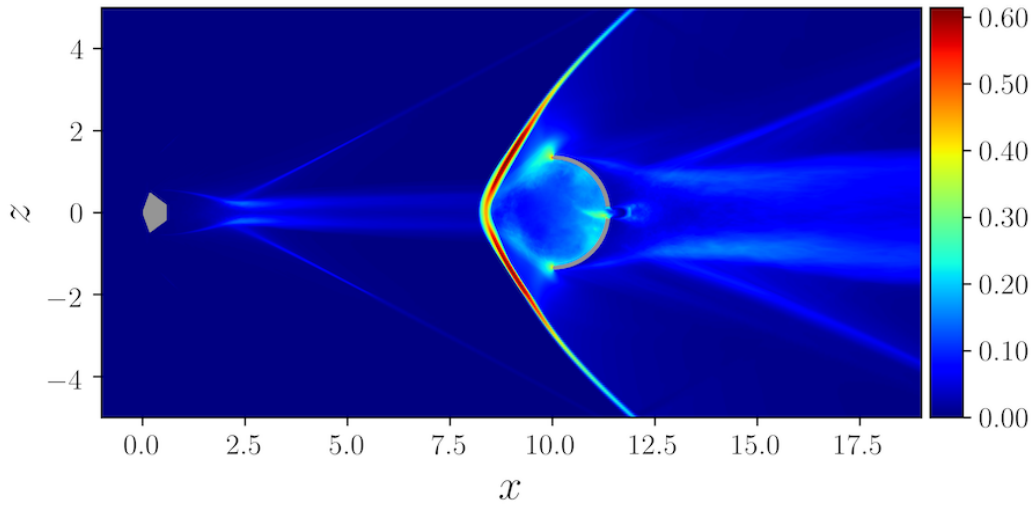

(a) Density

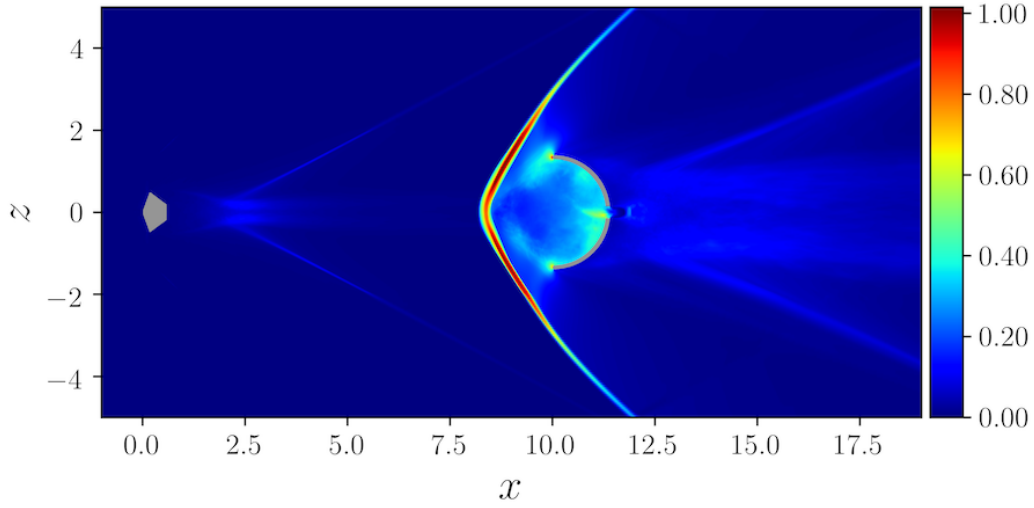

(b) Pressure

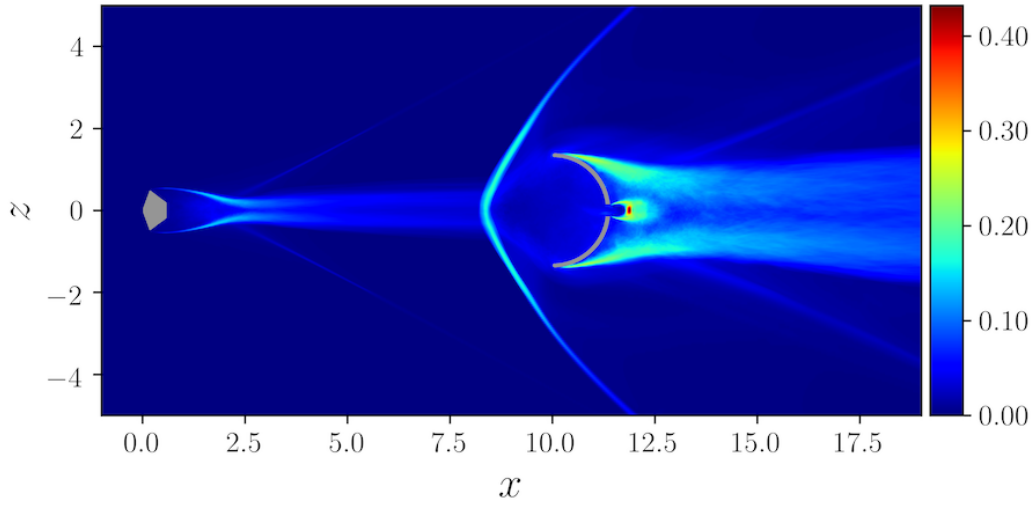

(c) Temperature

Figure 3.8: RMS fields of density, pressure and temperature fluctuations. All quantities are normalized with respect to the corresponding free-stream values.

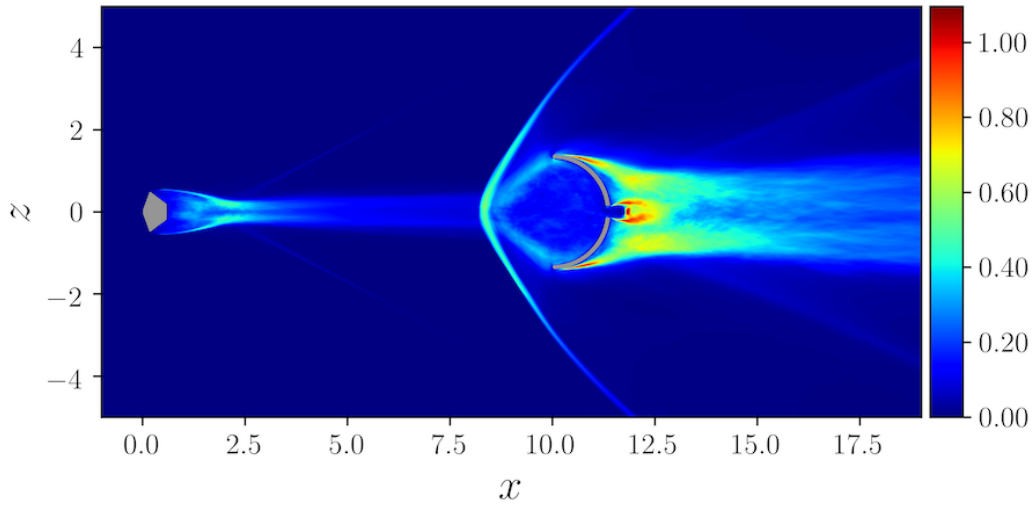

(a) u_{rms}

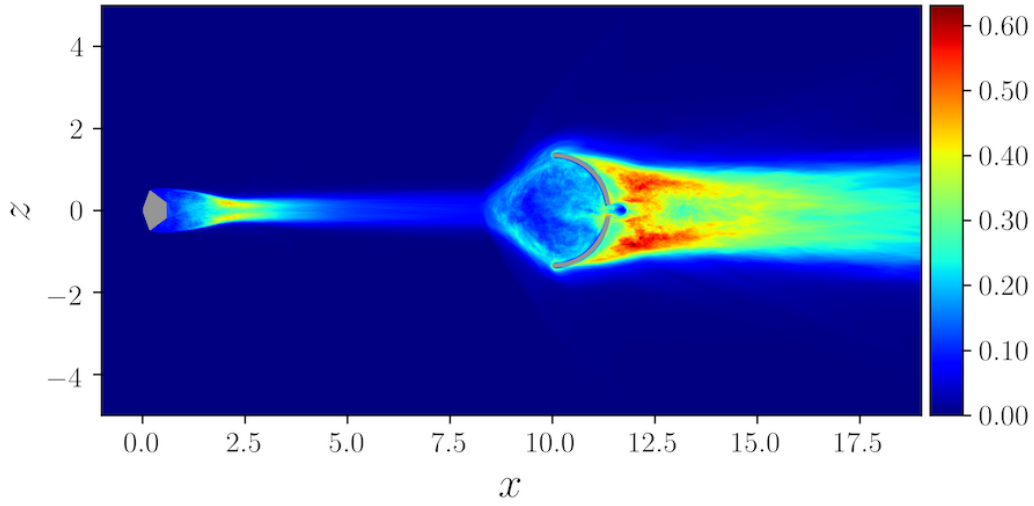

(b) v_{rms}

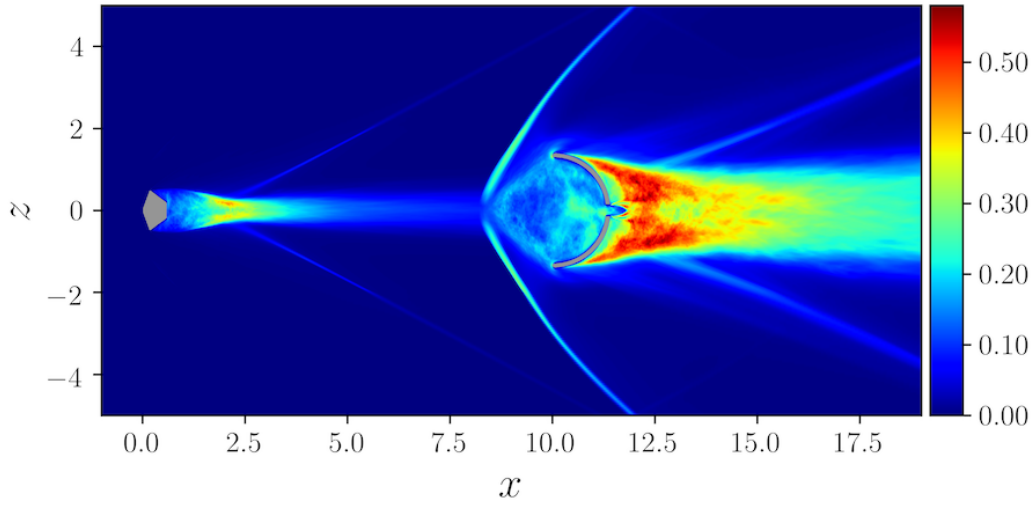

(c) w_{rms}

Figure 3.9: RMS fields of the velocity fluctuations along the three directions.

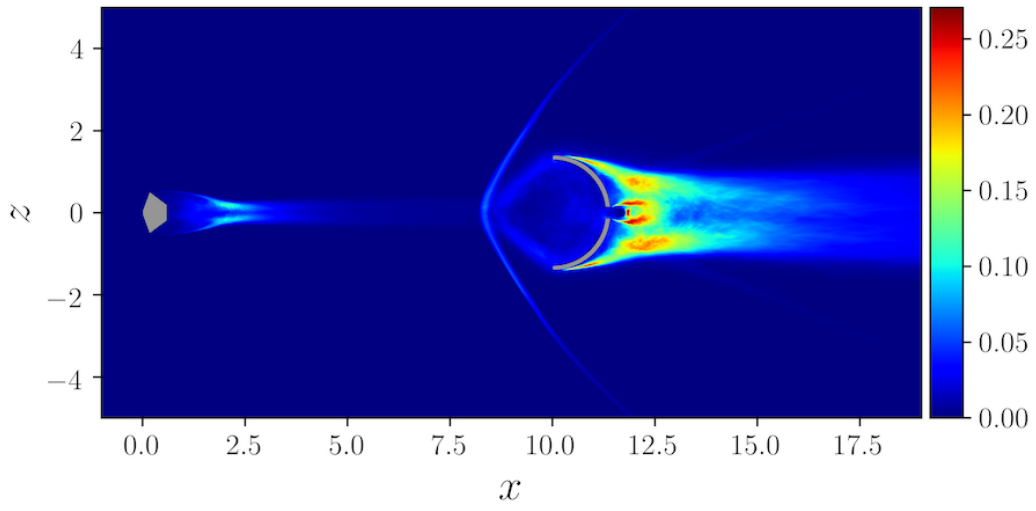

(a) k/K_∞

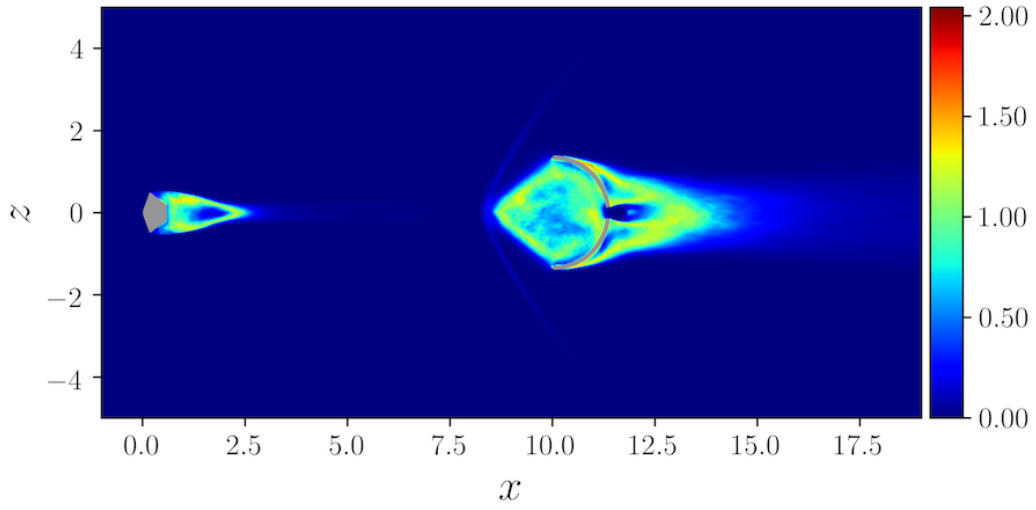

(b) k/K

Figure 3.10: Fields of Turbulent Kinetic Energy, k, normalized with K_∞ (3.10a) and with K (3.10b); K is the local specific kinetic energy of the mean flow, while K_∞ is its value in free-stream conditions.

ONE-DIMENSIONAL ANALYSIS OF FLUCTUATIONS

Also with regard to the assessment of fluctuations, it is significant to consider the spatial trend of the RMS of fluctuations computed along x-axis, shown in figure 3.11. As for density and pressure (3.11a), we see that the capsule bow shock, located at $x \simeq -0.3$, is steady (zero fluctuations), while a prominent fluctuations peak is visible at the canopy bow shock, at $x \simeq 8.5$, due to its unsteadiness. Temperature fluctuations reach their maximum just after the vent (3.11b), and a similar trend characterizes both the x-component of velocity fluctuations, u_{rms} (3.11d), and the K_∞-normalized TKE (3.11f). All peaks of T_{rms}, u_{rms} and k/K_∞ occur at $x \simeq 12.0$, which is the mean interface location between vent outflow and canopy near-wake. Also y- and z-component of velocity fluctuations, v_{rms} and w_{rms}, reach their peak at $x \simeq 12.0$ (3.11c), but its value is less that halved compared to u_{rms}'s. For v_{rms} and w_{rms} is almost absent the relative maximum at the canopy bow shock, which, instead, is clearly visible for u_{rms}. Since we are computing the fluctuations RMS along x-axis, in fact, the impact of the bow shock is much stronger on the normal

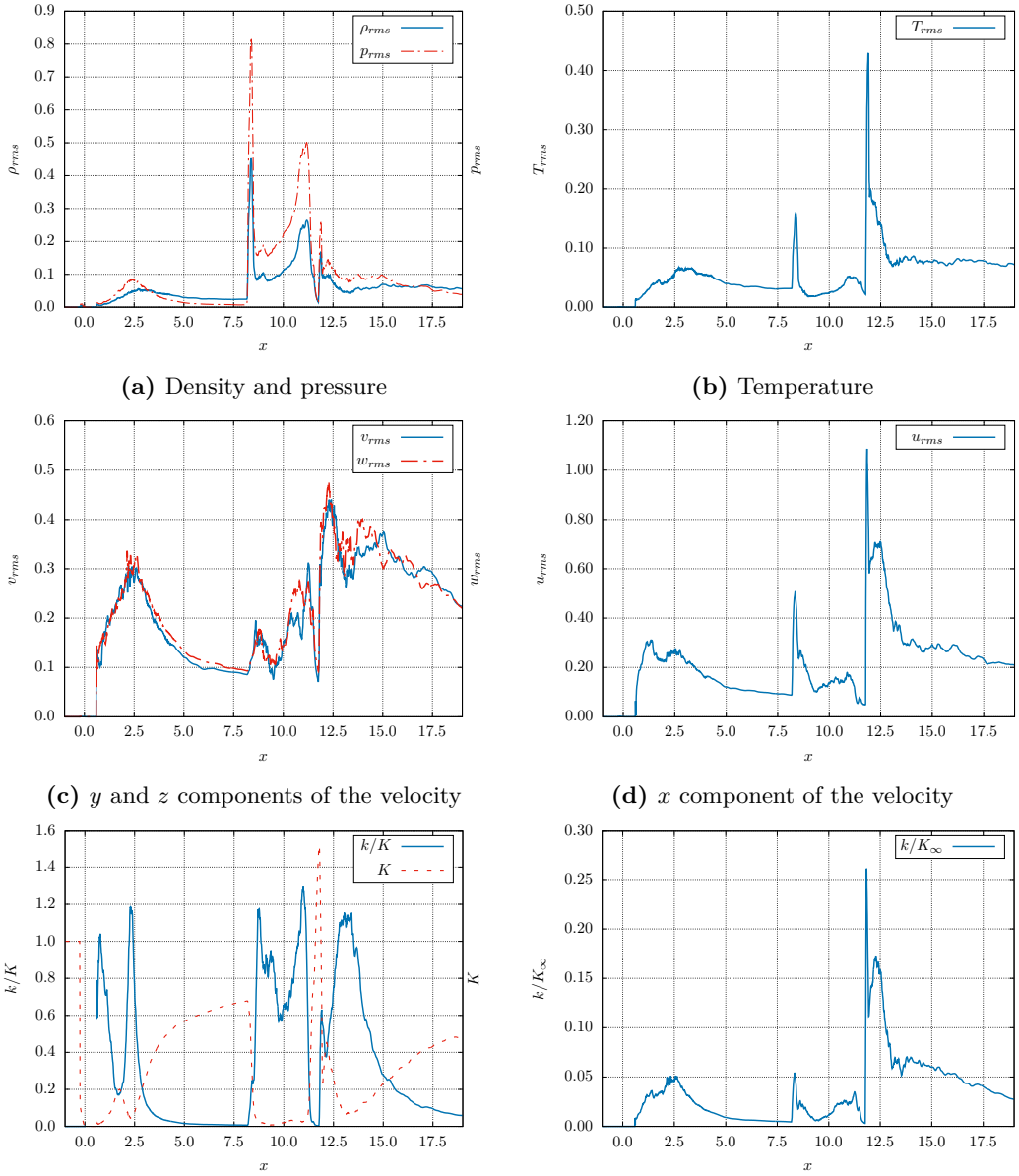

(a) Density and pressure

(b) Temperature

(c) y and z components of the velocity

(d) x component of the velocity

(e) K-normalized TKE

(f) K_∞-normalized TKE

Figure 3.11: RMS of fluctuations computed along the symmetry axis.

component of the velocity, u, than on the other two, v and w. Finally, the TKE (blu line) normalized with the local value of K (red dashed line) is shown in graph 3.11e. We can identify five regions where the TKE is highest:

- $x \simeq 1.0$: back-shell wake;
- $x \simeq 2.5$: near-to-far wake transition (where the recompression shock originates);
- $x \simeq 8.5$: unsteady canopy bow shock;
- $x \simeq 11.0$: region within the canopy;
- $x \simeq 13.0$: parachute near-wake.

The analysis of fluctuations allowed us to localize the most unsteady flow regions, helping to detect the presence of the parachute *breathing*, focus of the next section.

3.4 PARACHUTE BREATHING CYCLE

The *breathing* is a cyclic phenomenon that affects all supersonic parachutes, and consists of cyclically inflating (*inhaling*) and deflating (*exhaling*) of the parachute itself. This phenomenon involves large deformations of the canopy flexible membrane, with variations of area and, consequently, drag modifications. By the present simulation, we have shown that the canopy flexibility is not the main cause of breathing, since this phenomenon is visible even if the parachute is considered rigid. More precisely, what appears is not the expansion and shrinkage of the canopy area, but rather a periodic motion of the canopy bow shock along the symmetry axis. This motion involves inhomogeneous pressure fluctuations, which lead to large drag variations, despite the canopy area remains constant. Main cause of the breathing cycle seems the aerodynamic interaction between capsule wake and canopy bow shock. In real applications of flexible parachutes, canopy deformations are an effect that couples with this interaction, amplifying drag variability.

The flow unsteadiness caused by the breathing is highlighted in figure 3.12, where are shown time-trends of the variables of interest: centerline position (or *standoff distance*) of the canopy bow shock (3.12a), drag coefficient of the parachute (3.12b), density and pressure within the canopy (3.12c). To verify the influence of the capsule wake on the breathing cycle, we performed a preliminary simulation of the flow field without the presence of the capsule. Results showed that, after the initial transient, the canopy bow shock settles into a steady state, and the drag coefficient results constant and equal to $C_D^* \simeq 0.81$. Conversely, when the shock is perturbed by the capsule wake, the drag exhibits an oscillatory pattern. Drag coefficients of both the ideal canopy, C_D^* (without capsule), and the actual canopy, C_D (with capsule), are shown in graph 3.12b. The mean drag coefficient on the parachute over the considered time span, $t \in [35, 60]$, is $\overline{C}_D = 0.59$, with oscillations about $\pm 15\%$ of the mean value. The period of oscillation is approximately two flow time, $2t_x = 8.78$. From graph 3.12c, we see that density and pressure within the canopy also show an oscillatory trend, with both low-frequency oscillations, in phase with drag oscillations, and high-frequency fluctuations, due to the small scales of turbulence. Conversely, oscillations of the bow-shock standoff distance, Δ, are in phase opposition to the drag coefficient: from graph 3.12a, we see that peaks of C_D are nearly simultaneous with troughs of Δ (zero indicating the parachute leading edge).

This phenomenon can be understood by looking more closely at the mechanism driving the unsteadiness of the canopy. In ideal conditions (without capsule), the incoming flow and the canopy bow shock travel at the same velocity: thus, the shock stabilizes in an equilibrium position and remains stationary. The addition of the capsule wake creates a momentum deficit in the incoming fluid, which alters the shape of the bow shock. Specifically, since the incoming flow has a lower velocity than the shock, the latter moves upstream toward the capsule, effectively increasing its standoff distance. Its shape also becomes more oblique: streamlines are turned outward and inhibit the mass flux into the canopy. This allows the parachute to eject some of its captured fluid mass around the sides of the canopy, as the outlet sections has widened due to the upstream motion of the shock. This phase corresponds to the *exhaling* of the parachute.

Now that the canopy is in an under-pressurized state, the bow shock tends to collapse inward, becoming flatter and reducing its standoff distance. Thus, streamlines are less diverted, leading to a higher density rise of the incoming gas, and outlet sections become narrower, leading to a higher mass flux into the canopy. Flow accumulates in the canopy, driving the latter to an over-pressurized state, corresponding to the

inhaling of the parachute. If momentum fluctuations of the incoming flow were exhausted, parachute breathing would cease after a few cycles. However, as the capsule wake remains turbulent, the cycle repeats. A similar dynamic of supersonic parachute breathing was also identified by Barnhardt et al. [27].

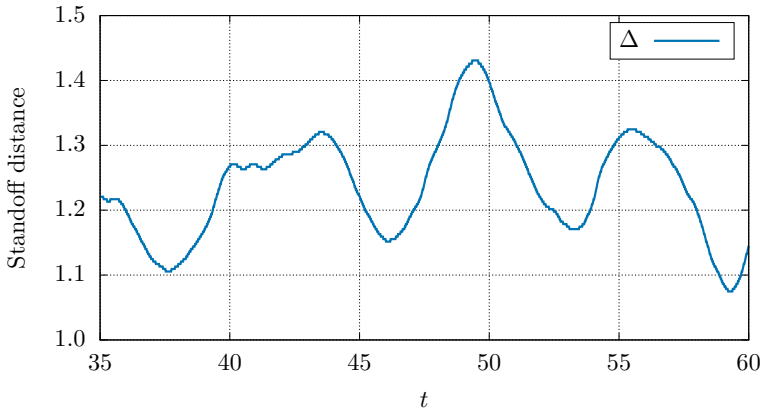

(a) Standoff distance, Δ, of the canopy bow shock, measured from the canopy leading edge in the capsule direction.

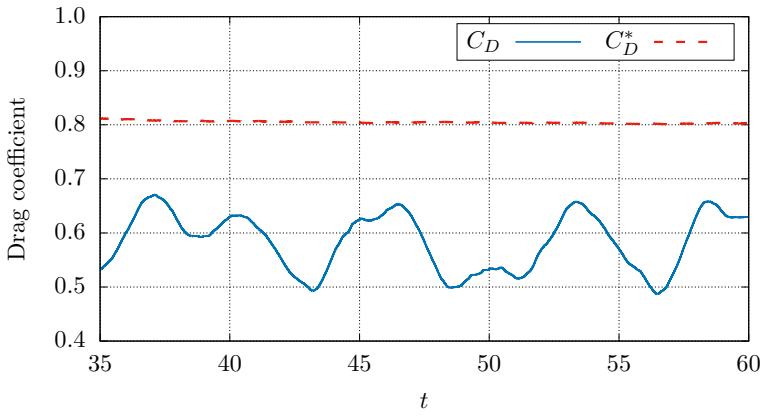

(b) Drag coefficient of the actual canopy, C_D, and drag coefficient of an ideal canopy, C_D^*, simulated without the capsule.

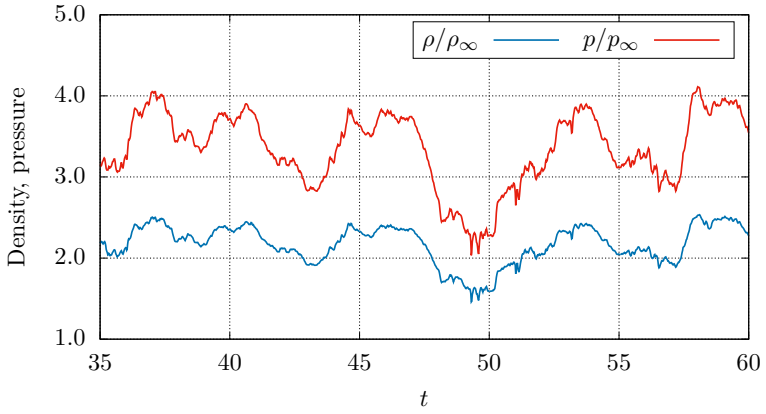

(c) Density, ρ/ρ_∞, and pressure, p/p_∞, of the gas within the canopy, computed at $x = 11, y = 0, z = 0$.

Figure 3.12: Trends over time of the variables of interest to the breathing cycle. These quantities are strictly related: troughs of Δ (i.e. shock close to the canopy, 3.12a) correspond to peaks of C_D and ρ/ρ_∞ (3.12b and 3.12c), and vice versa.

The parachute breathing cycle is clearly captured in figures 3.13, 3.14, 3.15, where are shown, respectively, the instantaneous field of density, pressure and numerical Schlieren. Each figure shows two transitions from the under-pressurized state (parachute exhaling) to the over-pressurized state (parachute inhaling), captured with a total of 8 snapshots separated by a normalized time of 1.5, from $t = 49.5$ to $t = 60$.

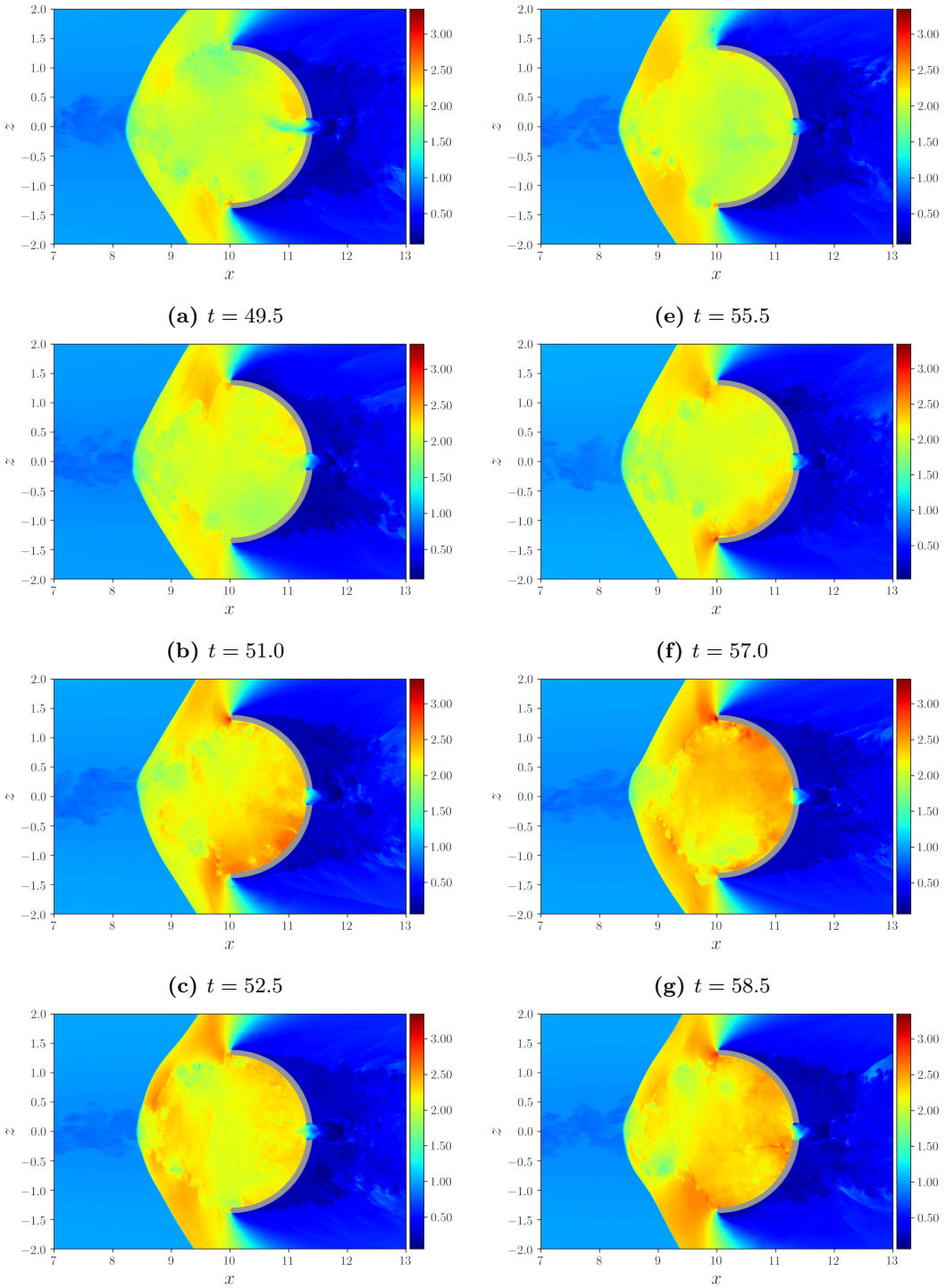

(a) $t = 49.5$ **(e)** $t = 55.5$

(b) $t = 51.0$ **(f)** $t = 57.0$

(c) $t = 52.5$ **(g)** $t = 58.5$

(d) $t = 54.0$ **(h)** $t = 60.0$

Figure 3.13: Instantaneous density field in the canopy region during different phases of the breathing cycle. Lower density is related to the exhaling phase, while higher density is related to the inhaling phase.

Specifically, in figures 3.13 and 3.14 are shown the quantitative variations in density and pressure corresponding to different phases of breathing. In figure 3.15 is shown the qualitative behavior of the flow, which is ejected from the sides of the canopy during the exhaling, while it accumulates within the canopy during the inhaling.

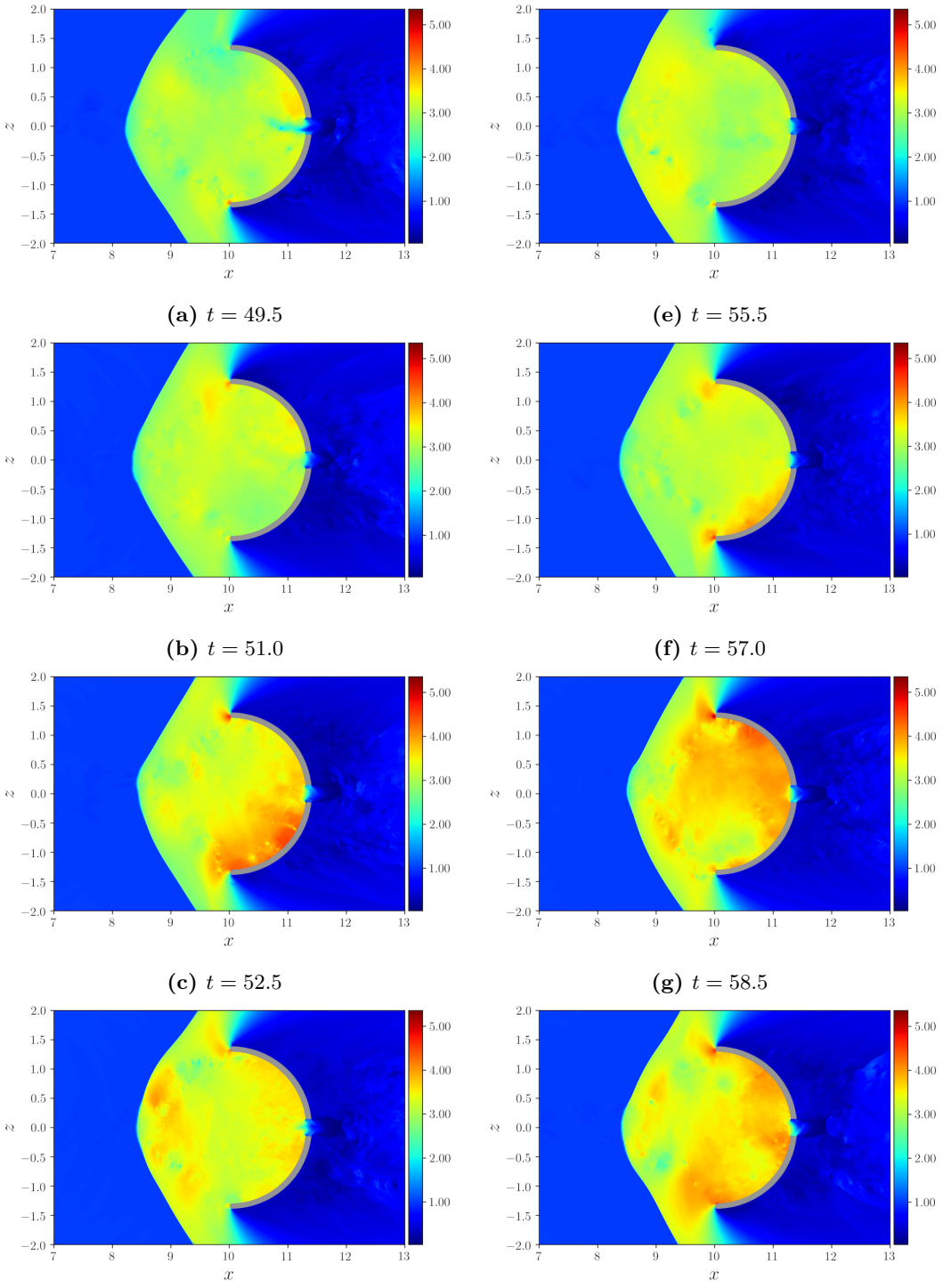

(a) $t = 49.5$ **(e)** $t = 55.5$

(b) $t = 51.0$ **(f)** $t = 57.0$

(c) $t = 52.5$ **(g)** $t = 58.5$

(d) $t = 54.0$ **(h)** $t = 60.0$

Figure 3.14: Instantaneous pressure field in the canopy region during different phases of the breathing cycle. Lower pressure is related to the exhaling phase, while higher pressure is related to the inhaling phase.

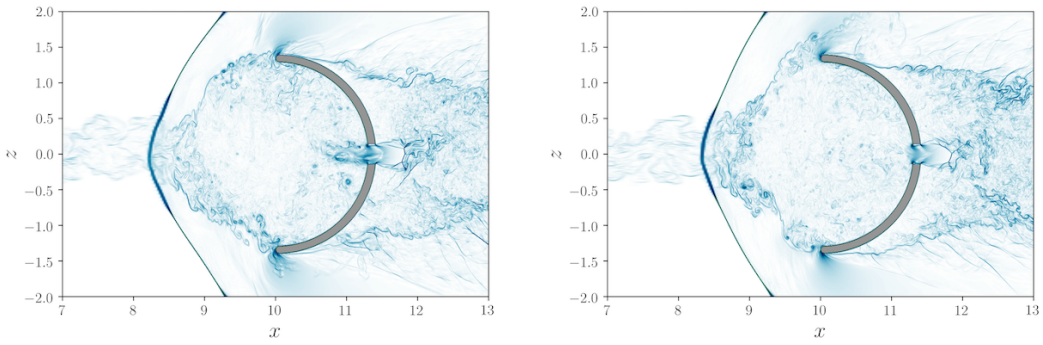

(a) $t = 49.5$

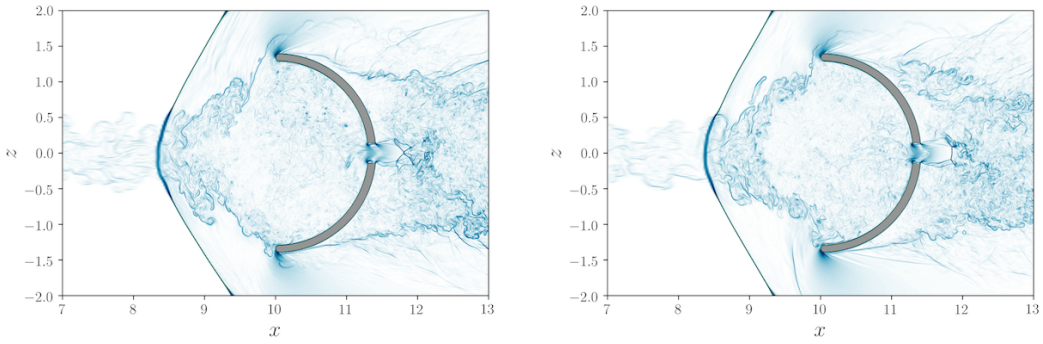

(b) $t = 51.0$

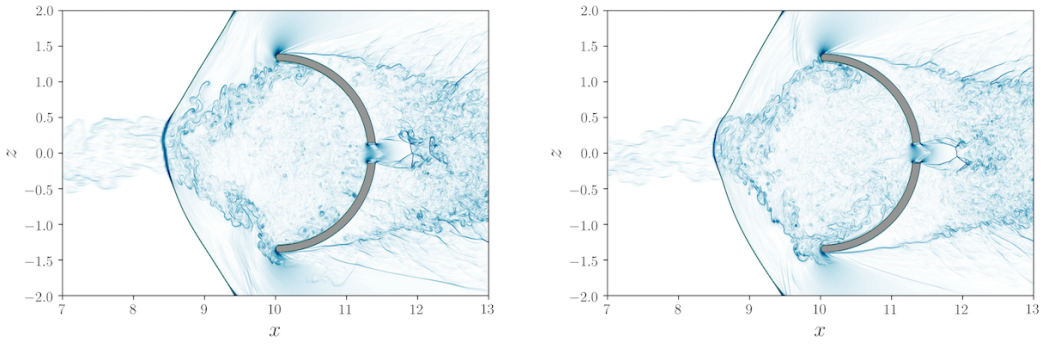

(c) $t = 52.5$

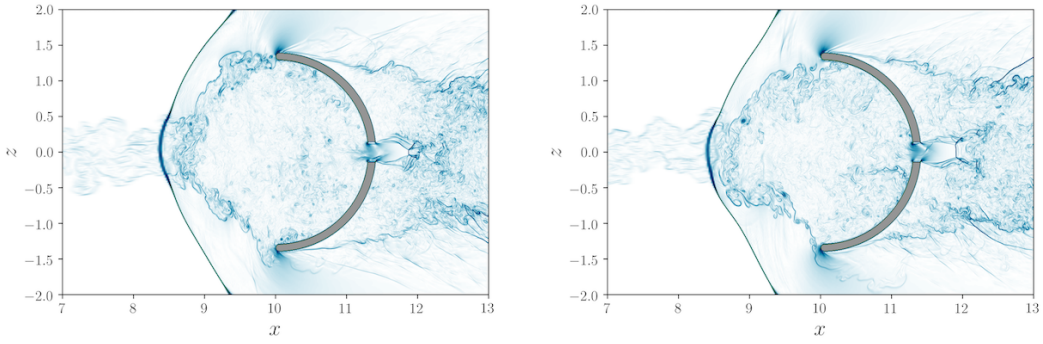

(d) $t = 54.0$

(e) $t = 55.5$

(f) $t = 57.0$

(g) $t = 58.5$

(h) $t = 60.0$

Figure 3.15: Instantaneous Schlieren field in the canopy region during different phases of the breathing cycle. The exhaling phase is related to greater standoff distance and greater outflow from the canopy leading edge, while the inhaling phase is related to a shorter standoff distance and a fuller canopy.

MODEL OF BREATHING CYCLE 4

4.1 PRELIMINARY CONSIDERATIONS

In the previous chapter, we have seen that the dynamics of supersonic parachutes is characterized by a breathing cycle, during which the canopy cyclically undergoes an inhalation phase, corresponding to an over-pressurized state, and an exhalation phase, corresponding to an under-pressurized state. Through the simulation results, we have shown that the breathing cycle occurs independently of the parachute flexibility, and involves a periodic oscillation of the canopy bow shock along the axis of symmetry.

THE BIG BUZZ ANALOGY

In the present chapter, we explore the original idea that the parachute breathing cycle can be related to the *big buzz* instability, a phenomenon of self-sustained shock oscillations that may appear in every type of supersonic inlets. Generally, this phenomenon arises when the entering mass flow is reduced below the so-called *buzz limit* (e.g. due to a turbulence momentum deficit), and results in high-amplitude pressure fluctuations [43]. A schematic diagram of the big buzz is shown in figure 4.1.

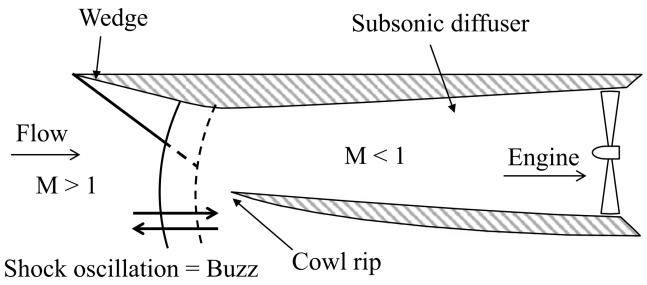

Figure 4.1: Schematic diagram of the big buzz instability [44].

The association between parachute breathing and inlet buzz is motivated by the fact that the rigid canopy can be seen as a supersonic inlet or, more precisely, as a converging nozzle with choked outflow. As mentioned in section 3.2, in fact, the supersonic inflow interacts with the canopy bow shock, becoming subsonic before entering the canopy; after crossing the canopy, the flow reaches the vent section in sonic conditions: thus, the vent represents the chocked throat of the nozzle.[1] Moreover, the fluctuations of the incoming turbulent wake can be seen as those perturbations that trigger and sustain the big buzz. Generally, the big buzz is a short-term phenomenon that is rapidly dampened, otherwise it would lead to severe effects, such as thrust loss and structural damages to the aircraft [45]. In our case, however, wake fluctuations persist over time, continuously feeding the breathing/buzz, which therefore cannot be dampened.

1 After leaving the vent, the flow accelerates: the supersonic region right after the vent, bounded by free-shear layers, could be considered as the diverging part of an ideal converging-diverging nozzle.

MODEL ASSUMPTIONS AND MOTIVATION

On the basis of these considerations and with the support of simulation results, we developed a lumped model, which captures the aerodynamic interaction between capsule wake and canopy bow shock, and describes the time-trend of shock position and flow variables downstream of the shock. The model, derived from a mass balance, is zero-dimensional, i.e. space-variations are neglected and only time-variations are considered. Underlying the model is the assumption that the shock in front of the canopy is normal, which is only true around the symmetry axis, i.e. for $|z| \to 0$.

We undertook this analysis with the aim of providing general guidance for the design of a parachute that achieves the optimal condition between drag and stability. Being based on strong simplifying assumptions, the model cannot offer highly-accurate results in terms of drag coefficient and oscillations amplitude. Rather, its purpose is to identify the qualitative (or *semi-quantitative*) trends of the involved quantities.

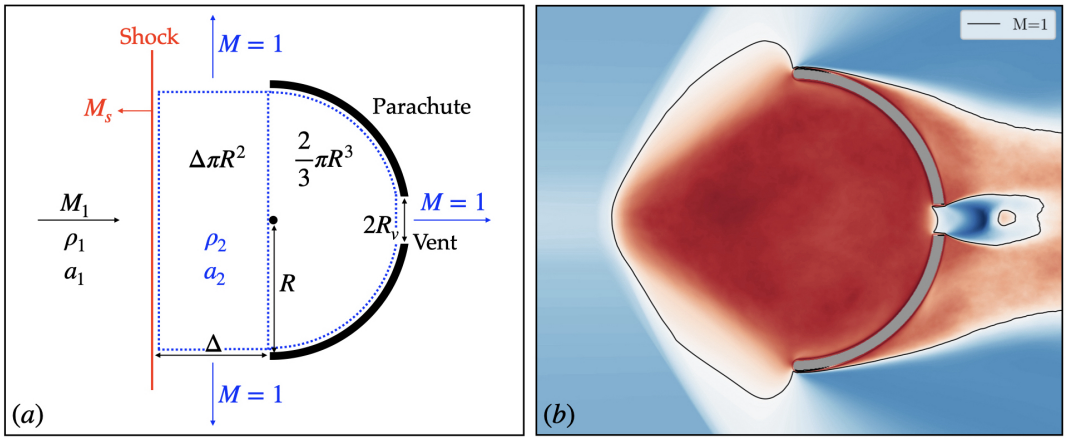

Figure 4.2: Two dimensional sketch of the geometry of the model $(x, z$ plane).

A geometrical sketch of the proposed model is illustrated in figure 4.2 (a), where we have emphasized the incoming flow from the capsule wake, identified by the variables M_1, ρ_1, a_1, and the flow downstream of the canopy bow shock, identified by ρ_2, a_2. Downstream conditions represent an average condition of the flow region within the canopy, which assumes great relevance regarding density and pressure. Specific attention must be paid on the Mach number. Downstream of a normal shock, the flow is always subsonic; however, the outflow Mach number assumes greater importance for the model, being involved in the mass balance between incoming and outgoing flow. Therefore, we denote by M_2 the Mach number of outflow sections. In addition, the shock wave moves relatively to the incoming flow: we denote by M_s the shock Mach number, which directly links upstream and downstream conditions through the normal shock relations.

In figure 4.2 (b) is shown a detail of the mean Mach number field over the canopy region, taken from the simulation. We see that the black isoline indicating $M = 1$, in addition to lying at the bow shock, lies along the outflow sections, consisting of the canopy leading edge and vent. Thus, the Mach number of the modeled outflow regions is set to $M_2 = 1$. Besides the normal-shock assumption, we also assume that the sonic line in between shock and leading edge is straight, greatly simplifying the mass balance calculation. As shown in figure 4.2 (b), however, both the actual shock and sonic line are curved. For a more accurate estimation of the parameters, especially the standoff distance, we can consider a straight sonic line correction factor, as outlined by Adams et al. [46].

4.2 MATHEMATICAL FORMULATION

Referring to figure 4.2 (a), we consider two flow locations with respect of the shock: the incoming flow is represented by upstream conditions, $\bullet_1$; after crossing the shock, the flow assumes downstream conditions, $\bullet_2$. The downstream flow collected within the parachute has two escape ways: the first consists of the upper and lower sections in between the normal shock and the canopy leading edge, represented as horizontal lines in figure 4.2 (a); the second consists of the vent. Upstream conditions are set according to the mean conditions of the capsule far-wake, obtained from the simulation. Downstream conditions, instead, are computed by the model, exploiting both a mass balance and the normal shock relations (3.6) as a function of the shock Mach number. In figure 4.2 (a) we also report the values of the volumes of interest for the mass balance. The control volume, V, is given by the canopy volume (a semi-sphere), $2/3 \cdot \pi R^3$, plus the volume in between the shock and the canopy, $\Delta \pi R^2$

$$V(t) = \frac{2}{3}\pi R^3 + \Delta \pi R^2 \tag{4.1}$$

where R is the canopy radius, and $\Delta = \Delta(t)$ is the standoff distance separating the bow shock from the canopy. Since Δ varies over time, also V does so. The time-variation of Δ is given by the difference between the velocities of incoming flow and bow shock. Expressing the velocity as $u = M \cdot a$, we obtain

$$\frac{\partial \Delta}{\partial t} = M_s a_s - M_1 a_1 \quad \xrightarrow{a_s \simeq a_1} \quad \frac{\partial \Delta}{\partial t} = (M_s - M_1)\, a_1 \tag{4.2}$$

where M_s and a_s are Mach number and sound speed of the shock, while M_1 and a_1 are Mach number and sound speed of the upstream flow. Since the variation of a_1 over time and space is negligible, it is assumed constant and equal to $a_1 = \sqrt{\gamma R_1 T_1} \simeq \sqrt{\gamma R_\infty T_\infty} = \sqrt{\gamma}$. The standoff distance, Δ, is obtained by integrating equation 4.2

$$\Delta = \int_0^t \frac{\partial \Delta}{\partial t}\, \mathrm{d}t = \Delta_e + (M_s - M_1)\, a_1\, t \tag{4.3}$$

where Δ_e is the standoff distance in equilibrium conditions, i.e. when $M_1 = M_s$. Once defined the geometric variables, we can calculate the mass balance by applying the principle of mass conservation

$$\frac{\mathrm{d}}{\mathrm{d}t} \int_V \rho \, \mathrm{d}V + \int_{\partial V} \rho\, u_i n_i \, \mathrm{d}S = 0 \tag{4.4}$$

where the control volume V is defined in equation 4.1. We observe that the fluid mass contained by the control volume varies over time, due to both the shock motion ($\partial V / \partial t \neq 0$) and the gas compressibility ($\partial \rho / \partial t \neq 0$). Explicating the fluxes of equation 4.4, we derive

$$\underbrace{\frac{\partial}{\partial t}(\rho_2 V)}_{\textit{Mass variation}} = \underbrace{\pi R^2 \cdot M_1 a_1 \cdot \rho_1}_{\textit{Inflow}} - \underbrace{(\pi R_v^2 \cdot M_2 a_2 \cdot \rho_2}_{\textit{Vent outflow}} + \underbrace{2\pi R \Delta \cdot M_2 a_2 \cdot \rho_2)}_{\textit{Leading edge outflow}} \tag{4.5}$$

where R_v is the vent radius. As mentioned in the previous section, M_2 indicates the Mach number of outflow sections, which are in sonic conditions.

By placing $M_2 = 1$ and explicating the left-hand-side derivative, we get

$$\frac{\partial \rho_2}{\partial t} V + \rho_2 \frac{\partial V}{\partial t} = \pi R^2 M_1 a_1 \rho_1 - \left[\pi a_2 \rho_2 (R_v^2 + 2R\Delta)\right] \tag{4.6}$$

From equation 4.2, we can compute the time-derivative of the volume as

$$\frac{\partial V}{\partial t} = \pi R^2 \frac{\partial \Delta}{\partial t} = \pi R^2 (M_s - M_1) a_1 \tag{4.7}$$

and, substituting equation 4.7 in 4.6, we can write

$$\frac{\partial \rho_2}{\partial t} V = \pi R^2 M_1 a_1 \rho_1 - \left[\pi a_2 \rho_2 (R_v^2 + 2R\Delta)\right] - \pi R^2 (M_s - M_1) a_1 \rho_2 \tag{4.8}$$

Finally, dividing both sides by ρ_1, and indicating $\rho_2/\rho_1 = P$, we obtain

$$\frac{\partial P}{\partial t} = \frac{\pi R^2}{V} M_1 a_1 - \frac{P}{V}\left[\left(\pi R_v^2 + 2\pi R\Delta\right) a_2 + \pi R^2 \left(M_s - M_1\right) a_1\right] \tag{4.9}$$

Equation 4.9 is a non-linear first-order differential equation, and it expresses the time-variation of the density ratio, P. The inflow Mach number, M_1, is the free coordinate of the model, while the shock Mach number, M_s, can be related to P by exploiting the normal shock relations, thanks to the first hypothesis of the model

$$\frac{\rho_2}{\rho_1} = P = \frac{(\gamma+1) M_s^2}{2 + (\gamma - 1) M_s^2} \quad \xrightarrow[M_s]{\text{solve for}} \quad M_s = \sqrt{\frac{2P}{(\gamma+1) - P(\gamma-1)}} \tag{4.10}$$

The model can also be used to roughly estimate the drag coefficient of the parachute. To this purpose, it is necessary to calculate the downstream pressure, which is assumed uniform within the canopy, and is given by

$$\frac{p_2}{p_1} = 1 + \frac{2\gamma}{\gamma + 1}\left(M_s^2 - 1\right) \tag{4.11}$$

By solving the governing equation of the system (4.9), we are able to analytically describe the parachute breathing cycle, which is the main purpose of the model.

PHYSICAL MEANING OF THE MODEL

A block diagram schematizing the general operation of the model is provided in figure 4.3. Given the inflow Mach number as input, the model provides the density ratio as output, allowing to estimate density fluctuations and all the other involved variables. The physical meaning behind this model recalls the driving mechanism of the breathing cycle, described in section 3.4.

Figure 4.3: Block diagram schematizing the general operation of the model in terms of input/output.

If ideally the canopy were not perturbed by the turbulent wake of the capsule, the flow would reach an equilibrium condition, in which the canopy bow shock is stationary, i.e.

$M_1 = M_s$. However, velocity fluctuations of the incoming turbulent wake cause M_1 to oscillate around its equilibrium position. If M_1 increases, then the inflow is faster than the shock, which moves downstream towards the canopy, i.e. Δ is decreasing. Consequently, also V is decreasing, as stated by equations 4.2 and 4.7

$$M_1 > M_s \implies \frac{\partial \Delta}{\partial t} = (M_s - M_1)a_1 < 0 \implies \frac{\partial V}{\partial t} = \pi R^2 \frac{\partial \Delta}{\partial t} < 0 \tag{4.12}$$

The volume reduction produces an increase in P (equation 4.9), related to the over-pressurization of the parachute inhaling. In compliance with normal shock relations, if the density increases, then also M_s must increase (equation 4.10), exceeding M_1. This means that the shock is now faster than the inflow, and moves upstream towards the capsule, i.e. Δ is increasing. The process is thus reversed, as V is increasing and P is decreasing, corresponding to the under-pressurization of the parachute exhaling. Due to the velocity fluctuations of the capsule wake, this cycle repeats without ever reaching a steady state. An illustration of this process is shown in figure 4.4, where the input M_1 is assumed to have a sinusoidal trend.

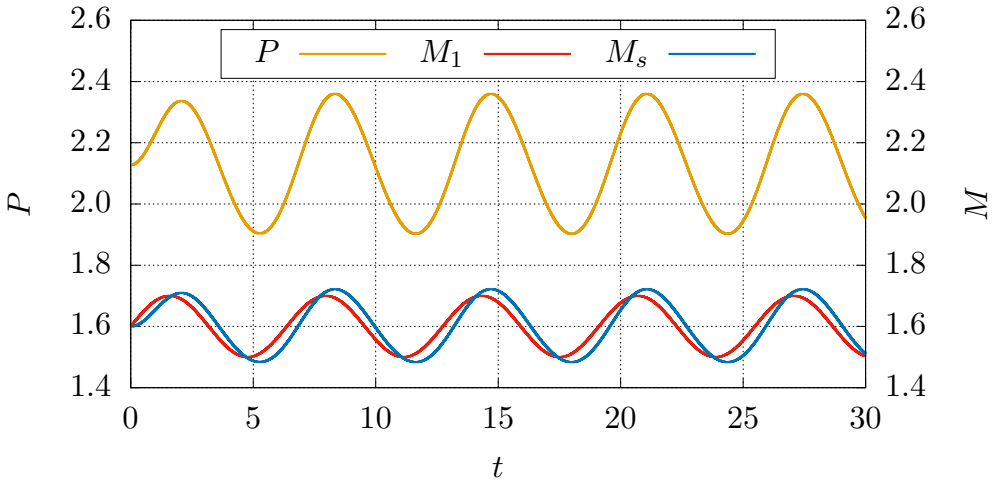

Figure 4.4: Trend over time of density ratio, P, input Mach number, M_1, and shock Mach number, M_s. We see that an increase of the input ($M_1 \uparrow$), causes the shock to approach the parachute ($\Delta \downarrow$), the density to increase ($P \uparrow$), and the shock to accelerate ($M_s \uparrow$); vice-versa if M_1 decrease.

From equation 4.9, we can observe that the canopy volume plays a key role in damping the density oscillations: a larger canopy would seem to lead to a more stable system. This hypothesis will be investigated in the following.

4.3 MODEL VALIDATION

In the first place, we verify reliability and accuracy of the model against the results of the simulation. The validation of the model is based on two steps: *i)* the calculation of equilibrium conditions, which correspond to mean conditions; *ii)* the generation of an input signal, which allows us to evaluate the dynamic response of the system.

SYSTEM RESPONSE IN EQUILIBRIUM CONDITIONS

In the ideal case of a parachute undisturbed by the turbulent wake of the capsule, the flow would reach the *equilibrium conditions*, corresponding to the mean position around which the oscillations occur. As we have seen, if the inflow were stationary, the bow shock ahead of the canopy would be motionless. Since the shock motion is the driving mechanism of the breathing cycle, in these condition the density ratio stabilizes to a constant value. Mathematically, $M_1 = M_s$ and $\partial P/\partial t = 0$. By substituting in equation 4.9, we obtain

$$\frac{\pi R^2}{V_e} M_e a_{1,e} = \frac{P_e}{V_e}\left(\pi R_v^2 + 2\pi R \Delta_e\right) a_{2,e} \tag{4.13}$$

where $\bullet_e$ indicates the equilibrium condition. The equilibrium Mach number, M_e, can be obtained from the simulation results. We consider the instantaneous Mach number along the axis of symmetry ($z = 0$) just before the shock ($x = 8$), and we average it over the time window analyzed, $t \in [30, 60]$. The resulting equilibrium Mach number is $M_e = 1.60$, which allows us to compute all other quantities at equilibrium

$$P_e = \left.\frac{\rho_2}{\rho_1}\right|_e = \frac{(\gamma+1)M_e^2}{2 + (\gamma-1)M_e^2} = 2.13 \tag{4.14}$$

$$\left.\frac{p_2}{p_1}\right|_e = 1 + \frac{2\gamma}{\gamma+1}\left(M_e^2 - 1\right) = 2.76 \tag{4.15}$$

$$A_e = \left.\frac{a_2}{a_1}\right|_e = \sqrt{\left[1 + \frac{2\gamma}{\gamma+1}\left(M_e^2 - 1\right)\right] \cdot \frac{2 + \left(\gamma-1\right)M_e^2}{\left(\gamma+1\right)M_e^2}} = 1.14 \tag{4.16}$$

and, from equations 4.13 and 4.1,

$$\Delta_e = \frac{R}{2}\left(\frac{M_e}{A_e P_e} - \frac{R_v^2}{R^2}\right) = 0.42 \tag{4.17}$$

$$V_e = \frac{2}{3}\pi R^3 + \Delta_e \pi R^2 = 6.58 \tag{4.18}$$

We note that these values are *semi-quantitative*, i.e. corrected in terms of order of magnitude, rather than in terms of detail. Specifically, we note that the modeled value of density ratio, $P_{mod} = 2.13$, is definitely close to the simulated value, $P_{sim} = 2.53$, while the modeled standoff distance, $\Delta_{mod} = 0.42$, is about 1/3 of the simulated one, $\Delta_{sim} = 1.24$. This is mainly due to the assumption of normal shock and straight sonic line. To be more accurate, we can utilize the *straight sonic line correction factor* suggested by Adams et al. [46], defined as $F_{sl} = \Delta^*/\Delta$, where Δ^* is the standoff distance computed assuming a straight sonic line, while Δ is the actual standoff distance. From the graph in figure 4.5 we see that, for an axisymmetric body with $M_\infty = M_e = 1.6$, we can assume $F_{sl} = 0.48$. We observe, though, that F_{sl} does not consider that the shock is assumed to be normal rather than curved: therefore, it must be multiplied by a *normal shock correction factor*, F_{ns}, obtaining $F_{sl}F_{ns} = \Delta^*/\Delta$. Given the originality of this analysis, such a correction factor is not found in the literature, but it can be roughly estimated. From the sketch on the right of figure 4.5, we see that, compared to the straight sonic line assumption, the normal shock assumption has less impact on the actual geometry: thus, a reasonable F_{ns} must be

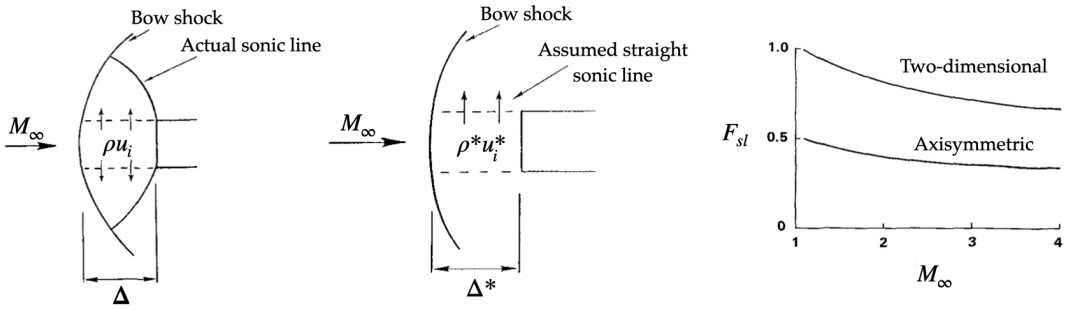

Figure 4.5: Sketch of the straight sonic line assumption, compared to the actual ones. On the right we can see the graph of the straight sonic line correction factor, F_{sl}, in function of M_∞ for both two-dimensional and axisymmetric bodies [46].

closer to one than F_{sl}. By setting the approximate value of $F_{ns} \simeq 0.70$, the actual standoff distance at equilibrium become

$$\Delta_e \simeq \frac{\Delta_e^*}{F_{sl} F_{ns}} = 1.25 \tag{4.19}$$

This value is in excellent match with the simulated one, $\Delta_{sim} = 1.24$, confirming the reliability of the model. Once the model reliability has been verified in the ideal case of static conditions, its dynamic behavior needs to be validated.

SYSTEM RESPONSE IN DYNAMIC CONDITIONS

We have seen that the dynamic response of the system is provided by the model as output starting from an input, which is represented by the inflow Mach number. In order for the modeled results to be comparable with simulated ones, it is necessary to provide an input signal that is both a simple function and an emulation of the actual Mach number of the inflow, provided by the simulation. An input signal with these features can be defined through a frequency analysis, by associating the actual signal with an ideal signal characterized by a single harmonic, i.e. a pure tone. Our goal, then, is to identify the *fundamental frequency* of the actual signal. The fundamental frequency is the harmonic component characterized by the maximum amplitude peak,

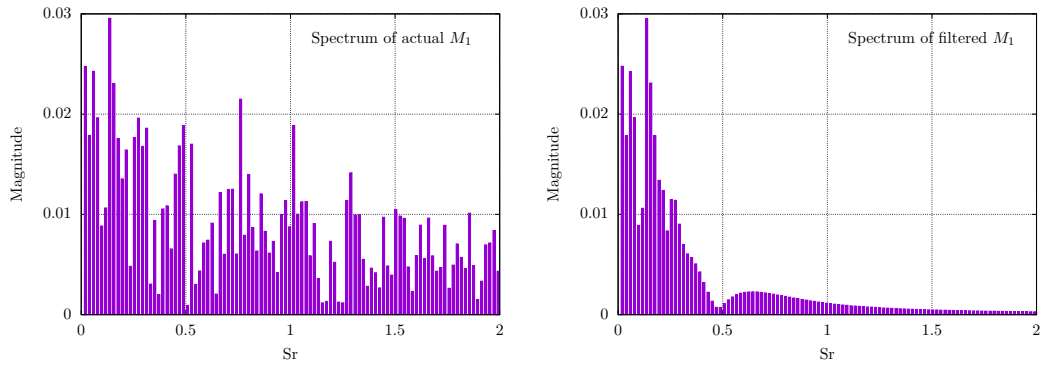

(a) Actual input, M_1 **(b)** Filtered input, M_1

Figure 4.6: Frequency spectrum of the input Mach number, obtained from the simulation, before and after the application of a low-pass filter. The frequency is expressed in terms of Strouhal number, Sr.

and it will be used as the frequency of the harmonic ideal signal. To this purpose, it is necessary to smooth the signal and cut off the highest frequencies, since the actual Mach number is extremely irregular. Thus, we applied a low-pass filter to the actual Mach number, and we computed the Fourier transform of both actual and filtered Mach number, obtaining the related *frequency spectrum*.

The frequency spectra of actual and filtered signals are shown, respectively, in figure 4.6a and 4.6b: they represent the amplitude components of the signal as a function of the frequency, which is expressed in terms of Strouhal number, Sr. From figure 4.6b, we see that the maximum amplitude peak is found at $Sr = 0.16$, which is, thus, the fundamental frequency of the signal. The correspondent amplitude peak is about 0.03. We considered, though, an amplitude contribution of $A = 0.10$, higher than the actual magnitude as it takes into account the neglected contributions of all other frequencies. Hence, the input Mach number is defined as

$$M_1(t) = M_e + A \sin(2\pi Sr \cdot t) \tag{4.20}$$

where $M_e = 1.60$ is the equilibrium Mach number derived above, $A = 0.10$ is the amplitude, and $Sr = 0.16$ is the Strouhal number corresponding to the fundamental frequency.

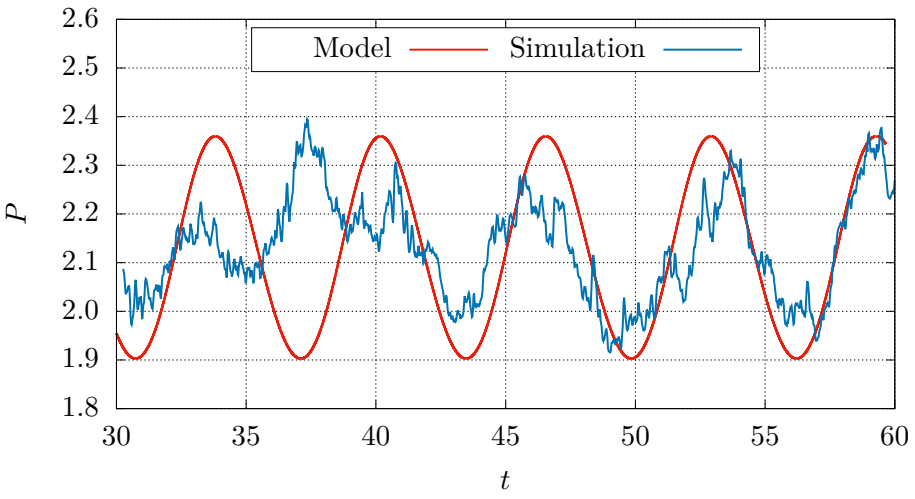

Figure 4.7: Comparison between the density ratio, P, provided by the model (red line) and by the simulation (blue line), measured at $x = 10, y = 0, z = 0$.

In figure 4.7 are compared the results of the simulation with those of the model, obtained using as input the sinusoidal Mach number defined in equation 4.20. The analyzed time window is $t \in [30, 60]$, expressed in dimensionless terms. From the graph of figure 4.7, we see that the amplitude of density oscillations is extremely well captured by the model, an also the fundamental frequency is essentially correct. The second peak of the density ratio, which occurs at $t \simeq 37.5$, corresponds to a frequency twice the fundamental, i.e. the second harmonic component of the actual signal. This peak can not be captured by the model, since the input M_1 is a pure tone, unlike the actual Mach number that has a continuum spectrum. This comparison confirms the *semi-quantitative* nature of the model, whose purpose is to provide an order of magnitude of the variables involved, rather than their detailed trends. The latter, in fact, is the goal of the simulation.

4.4 MODEL RESULTS

After verifying that the model is capable to capture the breathing cycle, we focus on assessing the effects of breathing on the parachute dynamics. The existence of breathing is visible from the oscillations of the standoff distance, while its intensity can be distinctly estimated from the oscillations of density within the canopy. Our aim is to understand whether the breathing intensity can be reduced by adjusting the geometric parameters of the parachute.[2] In the first place, we consider a canopy with the dimensions used in the simulation, based on ExoMars 2022, i.e. normalized radius of $R = 1.28$ and vent radius of $R_v = 0.13$.

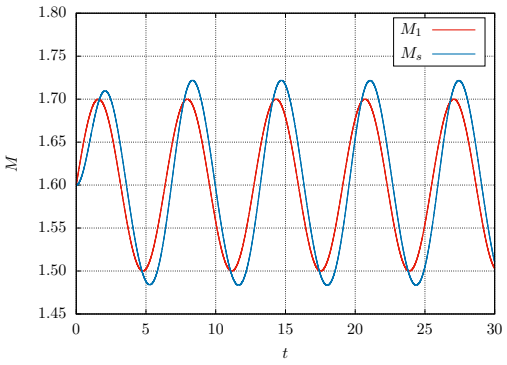

(a) Input Mach, M_1, and shock Mach, M_s

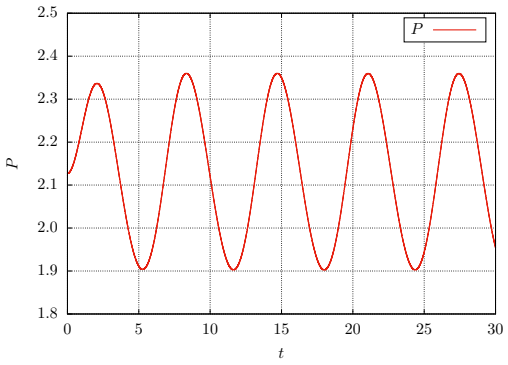

(b) Density ratio, P

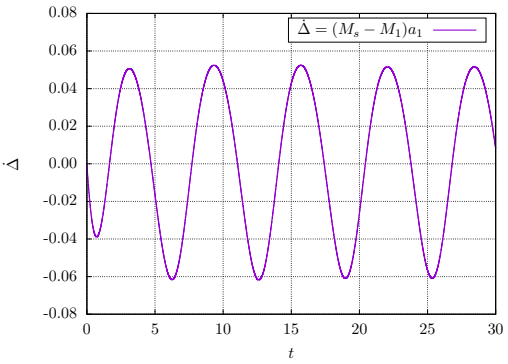

(c) Δ time-derivative, $\dot{\Delta} = (M_s - M_1)a_1$

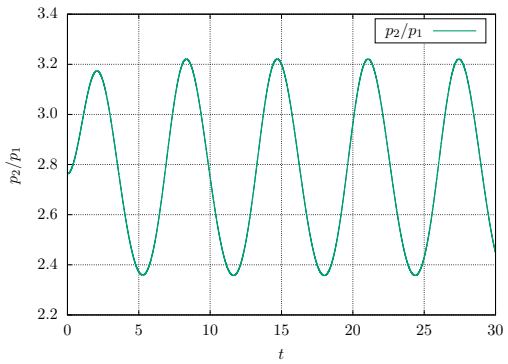

(d) Pressure ratio, p_2/p_1

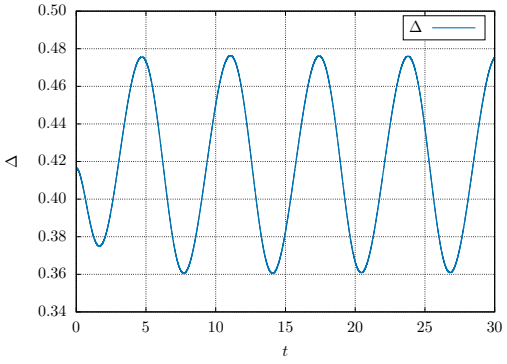

(e) Stand-off distance, Δ

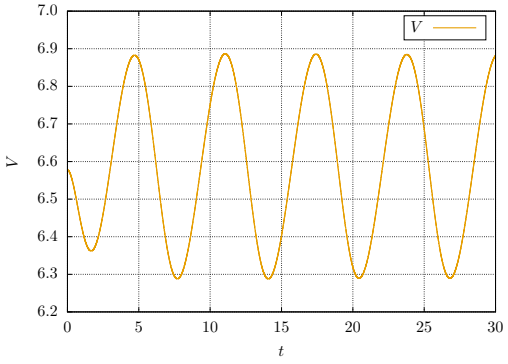

(f) Control volume, V

Figure 4.8: Trends over time of the variables of interest to the model.

2 The parachute breathing also depends on external parameters, represented by amplitude and frequency of the inflow Mach number, M_1. In this section we analyze the response of the system under nominal external conditions. These, however, can vary unpredictably: the effect of external conditions on the system behavior will be studied in the following.

The results of the model are shown in figure 4.8, where we report the trend over time of the system response, in terms of different variables, to the input M_1, defined in equation 4.20. It appears that, as M_1 increases, the standoff distance, Δ, and the volume, V, decrease. The volume reduction causes the density ratio, P, to increase, as well as the shock Mach number, M_s. As soon as M_1 begins to decrease, the process is reversed. After the first semi-period, the initial transient is exhausted and the system moves to a condition of dynamic equilibrium, with oscillations of constant amplitude. We observe that, while Δ and V are exactly in phase opposition with respect to the input M_1, conversely P and M_s follow M_1 with a slight phase delay. Time-trends of the different variables graphically confirm their relations derived above. These are summarized in table 4.1, where time-derivatives of Δ, V, P are related to the difference $M_s - M_1$.

$M_s - M_1$	$\dot{\Delta}$	$\dot{V}$	$\dot{P}$
< 0	< 0	< 0	> 0
$= 0$	$= 0$	$= 0$	$= 0$
> 0	> 0	< 0	< 0

Table 4.1: Summary of the relations between the main variables examined in figure 4.8.

Once examined the system behavior in the reference case of the simulation, and verified the reliability of the model, which was found to correctly describe the breathing phenomenon, we proceed to examine the influence of the geometric parameters. Specifically, we are interested in the role of the canopy radius, R, and the vent radius, R_v. The simulation values, $R = R_0 = 1.28$ and $R_v = 0.13$ are assumed as reference.

EFFECT OF THE CANOPY RADIUS

We analyze the effect of the canopy radius (and thus of its volume, which scales with the radius cubed) on the parachute stability. To assess stability, we compute the amplitude, A, of density oscillations as a function of the canopy radius, R. Density fluctuations are associated with flow instability, and are accompanied by pressure fluctuations, main cause of drag variability and unpredictability. Smaller amplitude, thus, corresponds to higher stability. From graph 4.8b, we see that the maximum deviation from the mean, i.e. maximum amplitude, for $R = R_0$ is $A \simeq 0.23$. We wonder whether the amplitude changes for different dimensions of the canopy, whose radius is normalized with the reference value of $R_0 = 1.28$. To extend this analysis to different flight conditions, three cases will be examined in terms of mean Mach number of the inflow: $M_e = 1.2$, $M_e = 1.6$ and $M_e = 2.0$, covering a range of free-stream Mach number indicatively from $M_\infty = 1.5$ to $M_\infty = 2.5$.

Left images of figure 4.9 show the maximum amplitude of density oscillations, A, as a function of the canopy radius, R/R_0. The radius, R, is varied from $0.2R_0$ to $3R_0$, for all three cases of equilibrium Mach number, M_e. The vent radius has been adjusted to keep the ratio R/R_v unchanged. In general, the amplitude reaches an absolute maximum for $R \simeq R_0$, and decreases not only as R increases, with an absolute minimum at $3R_0$, but also as R decreases, with a relative minimum at $0.2R_0$. It is interesting to note that the amplitude peak at $M_e = 1.6$ is obtained precisely for $R_0 = 1.28$, the reference value based on ExoMars 2022 mission. The shape of the amplitude curve as a function of the radius is comparable in all three cases of M_e; the difference is that the amplitude peak, A_{max}, shifts to the right (i.e. larger radius) as M_e increases. These considerations are summarized in table 4.2.

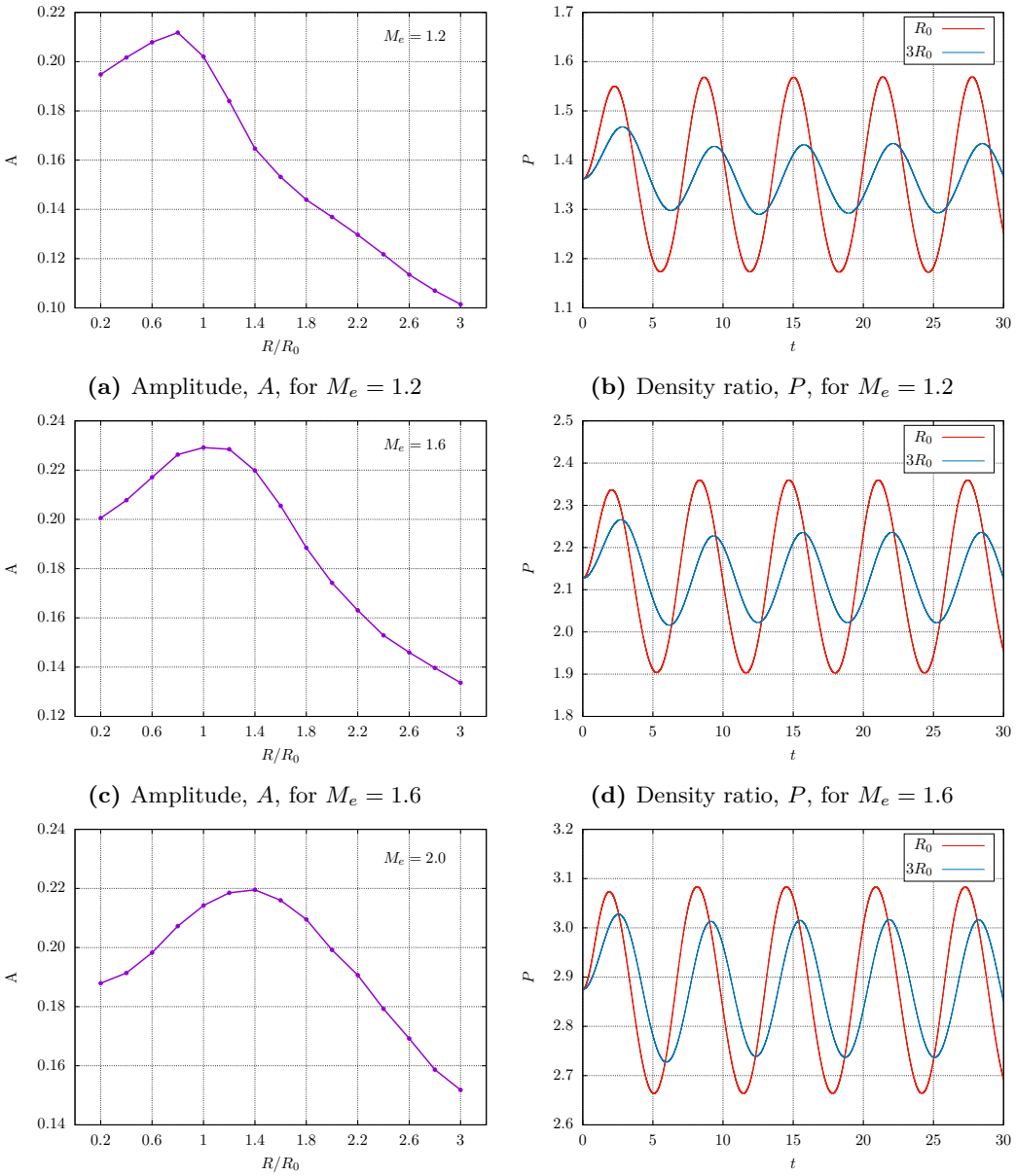

(a) Amplitude, A, for $M_e = 1.2$

(b) Density ratio, P, for $M_e = 1.2$

(c) Amplitude, A, for $M_e = 1.6$

(d) Density ratio, P, for $M_e = 1.6$

(e) Amplitude, A, for $M_e = 2.0$

(f) Density ratio, P, for $M_e = 2.0$

Figure 4.9: Left graphs: amplitude of density oscillations as a function of the canopy radius (normalized with respect to R_0). Right graphs: density oscillations over time for $R = R_0$ and $R = 3R_0$. The three cases correspond to different values of M_e.

M_e	P_e	R_{max}	A_{max}
1.2	1.37	$0.8R_0$	0.21
1.6	2.13	R_0	0.23
2.0	2.88	$1.4R_0$	0.22

Table 4.2: Values of amplitude peak, A_{max}, with the corresponding radius, R_{max}, for three values of equilibrium Mach number, M_e. The amplitude peak, A_{max}, appears independent of M_e, which instead affect the density ratio at equilibrium, P_e.

Right images of figure 4.9 show the time-trend of the density ratio, P, for both the reference case, $R = R_0$, and the upper-limit case, $R = 3R_0$. We see that the amplitude for R_0 is essentially the same in all three cases, while the amplitude for $3R_0$ increases for higher values of M_e, still remaining lower compared to the reference case. From figure 4.9 and table 4.2, we also note that the equilibrium Mach number, M_e, greatly changes the equilibrium position, P_e, while it slightly affects the peak of oscillations amplitude, A_{max}.

Recalling that the capsule diameter is $D_0 = 1$, the lower-limit case of $0.2R_0 = 0.26$ has no physical meaning, as a parachute with such a small canopy would be ineffective. The optimal design solution seems to be a larger canopy, which would lead to the double benefit of greater drag and greater stability. This result is in full agreement with the study conducted by Sengupta et al. [28], who observed a more stable flow as the relative size of the canopy to the capsule wake becomes larger. As highlighted in right graphs of figure 4.9, the stability of a larger canopy is more pronounced as the Mach number drops toward the sonic condition: this makes a larger canopy even more preferable to use, being increasingly stable throughout its operational period. We observe that the size of the canopy can be increased compatibly with the aerodynamic loads the parachute can withstand, as the drag force scales with the canopy cross-section, i.e. with the radius squared. Therefore, it is necessary for a larger canopy to be reinforced with stronger materials.

EFFECT OF THE VENT RADIUS

We focus now on the effect of the vent dimension on parachute stability. The vent is a circular hole in the back of the canopy: its role is to provide the canopy with a geometric porosity, nominally to improve stability. We verify whether a larger vent corresponds to greater stability, identified by smaller amplitude of density oscillations. In this case we fix the input Mach number to $M_1 = M_e + A\sin(2\pi Sr \cdot t)$, with the simulation-derived values of $M_e = 1.60,\ A = 0.10,\ Sr = 0.16$. Using as reference the simulation value of vent radius, $R_v = 0.13$, we analyze the behavior of a parachute without vent, $R_v = 0$, and with a vent twice as large as the reference, $2R_v$, fixed the value of canopy radius to R_0.

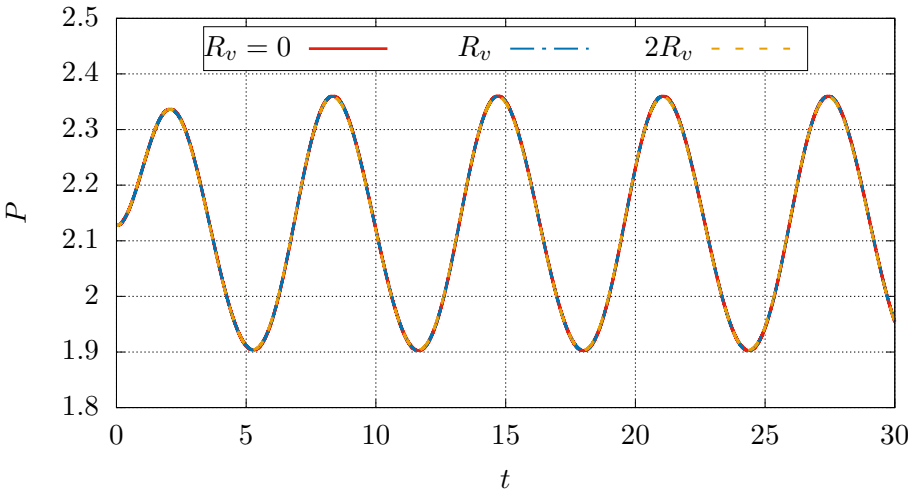

Figure 4.10: Trend over time of density oscillations for three different values of the vent radius, R_v. The effect of R_v on the amplitude of oscillations appears negligible.

Figure 4.10 shows the trend over time of the density ratio, P, for the three values of R_v. The three lines of the graph corresponding to the three values are overlapping,

Canopy radius	*Vent radius*	A_{max}
R_0	0	0.23
R_0	R_v	0.23
R_0	$2R_v$	0.23

Table 4.3: Values of amplitude peak, A_{max}, with the corresponding vent radius, R_v. Input Mach number and parachute radius are fixed.

indicating that the density ratio is practically independent of R_v. In table 4.3 are listed the values of maximum oscillations amplitude, A_{max}, for the three values of R_v. We see that A_{max} remains unchanged: therefore, the effect of R_v on the density trend is negligible. In fact, the vent radius is an order of magnitude less than the canopy radius ($R_v/R \simeq 10^{-1}$), and it is squared in equation 4.9. Rearranging equation 4.9,

$$\frac{V}{\pi R^2}\frac{\partial P}{\partial t} + \left[a_2\left(\frac{R_v^2}{R^2} + \frac{2\Delta}{R}\right) + a_1(M_s - M_1)\right]P = M_1 a_1 \tag{4.21}$$

we see that the term $R_v^2/R^2 \simeq 10^{-2}$ is negligible, and does not tangibly affect the evolution of P. Since a larger vent does not provide more stability, the optimal design solution seems to be a smaller vent, aiming to maximize the area of resistance and, thus, the drag force acting on the parachute.

FURTHER MODEL SIMPLIFICATIONS

In this section we have analyzed the behavior of the parachute as a function of geometric parameters, which we can refer to as *internal* parameters. While the effect of the vent size is negligible, we have shown that a larger canopy is subject to density fluctuations of smaller amplitude. The reason may be due to the response time of the system: a larger canopy takes longer to respond to input fluctuations, and does not reach the maximum amplitude, since it cannot keep pace with the constantly changing input. We could say that a larger parachute has greater *inertia*. This has a relevant implication: the response of a parachute subject to a high-frequency input will be characterized by small-amplitude oscillations.

To prove these two hypotheses, it is necessary to calculate the response time of the system, as well as to assess its behavior as a function of the input frequency. The response time can be estimated by an analysis in the Laplace domain, while its frequency response can be studied in the Fourier domain. This further analysis has two purposes:

- give a clearer physical meaning to each term of the governing equation, by simplifying the system into a canonical form;
- assess the impact of *external* parameters, such as the input frequency, on the system response.

Focusing on these two major goals, the system analysis in both Laplace and Fourier domains will be carried out in the following sections.

We observe that the stability of the system can also be studied by simplifying the model following a different approach. After identifying the main parameters on which the system response depends, the system can be linearized around the equilibrium position by expanding in Taylor series the governing equation. We refer to appendix A.1 for further details.

4.5 LAPLACE-DOMAIN ANALYSIS

The parachute dynamics, in terms of density fluctuations within the canopy, depends on the *response time* of the system. The response time is a relevant parameter, which expresses how quickly the system responds to an external impulse. The external forcing is nominally represented by fluctuations of the capsule wake interacting with the canopy shock; however, during the descent to Mars, sudden gusts of wind may occur, shifting the parachute-capsule system from the equilibrium position, to which the system must return. The time taken by the system to restore the equilibrium condition of stable oscillations is determined by the response time.

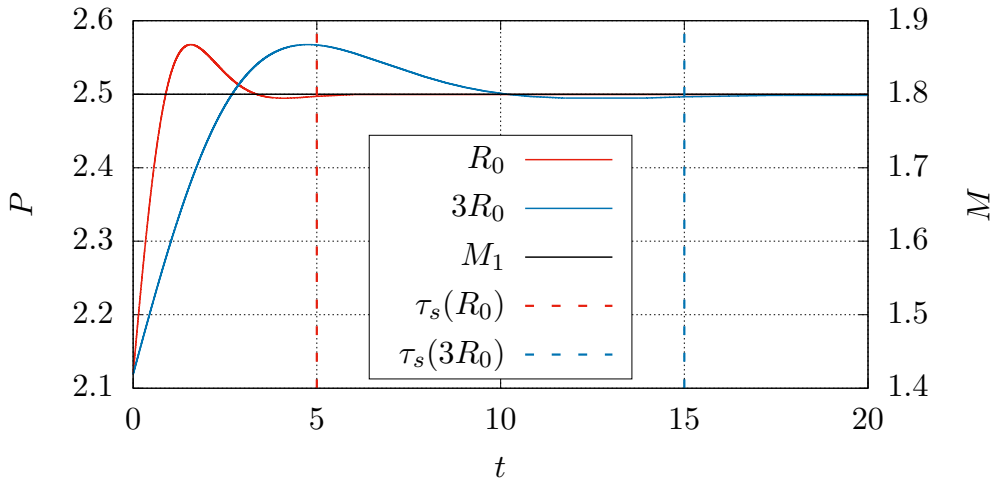

Figure 4.11: System response, P, at a step input, $M_1 = M_e + 0.2$, for two values of canopy radius, R_0 and $3R_0$. The settling time, τ_s, increases with the canopy radius.

To get a qualitative idea of the response time, we subject the system to a step input: this type of input is used to evaluate the response of the system to the initial transient. In the present system, the input is represented by the inflow Mach number, which in this case is set to $M_1 = M_e + 0.2$. In section 4.4 we have shown that the optimal design solution seems to be a larger canopy: thus, we focus on two cases of practical interest, considering the reference canopy, with radius R_0, and the upper-limit canopy, with radius $3R_0$. The two responses in terms of density ratio, P, to the step input, M_1, are shown in figure 4.11. We observe that the system with larger canopy (blue line) returns to equilibrium more gradually than the reference one (red line). From the graph we can estimate the settling time[3] of the two systems, which results $\tau_s \simeq 5$ for $R = R_0$, and $\tau_s \simeq 15$ for $R = 3R_0$. From this qualitative analysis, the response time of the system appears proportional to the canopy radius. The amplitude of the overshoot is nearly identical in the two cases, appearing independent of the canopy radius: since the input has only one variation, the larger parachute has all the time needed to reach the maximum amplitude.

The settling time, graphically derived in the time domain, can be more rigorously defined and quantified through an analysis in the Laplace domain. To this end, it is necessary to simplify the system and reduce it to a canonical form. This will also help to give a physical meaning to the different terms in the governing equation.

3 *Settling time* is defined as the time taken by the system to reach 95% of the final value.

SPRING-DAMPER MODEL

One possible approach to simplify the system is to consider it as a concentrated parameter model. Resuming the governing equation of the system (4.9)

$$\dot{P} = \frac{\pi R^2}{V} M_1 a_1 - \frac{P}{V}\left[\left(\pi R_v^2 + 2\pi R\Delta\right)a_2 + \pi R^2\left(M_s - M_1\right)a_1\right] \tag{4.22}$$

where we have placed $\partial P/\partial t = \dot{P}$, we see that the term $\pi R^2/V$ can be expanded by using the definition of the control volume (4.1)

$$\frac{\pi R^2}{V} = \left(\frac{2}{3}R + \Delta\right)^{-1} \tag{4.23}$$

Hence, we can rearrange the governing equation in the following form

$$\left(\frac{2}{3}R + \Delta\right)\dot{P} + \left[a_2\left(\frac{R_v^2}{R^2} + \frac{2\Delta}{R}\right) + a_1\left(M_s - M_1\right)\right]P = M_1 a_1 \tag{4.24}$$

As seen in section 4.4, the effect of the vent radius on the system behavior is negligible; considering the reference values, in fact, results $R_v^2/R^2 \simeq 10^{-2}$. Also the term $a_1(M_s - M_1) = \dot{\Delta} \simeq 5 \cdot 10^{-2}$ can be neglected, since our purpose is to predict the qualitative behavior of the system, without claiming to provide quantitative results. Neglecting the time-variation of Δ is physically equivalent to assume a stationary shock: this simplifying assumption is extremely strong, since the shock motion is a keystone phenomenon of the breathing cycle. Thus, it will be necessary to validate this simplified model, verifying whether it is able to provide reliable results in terms of magnitude order. If the shock is stationary, then Δ is constant and equal to the equilibrium standoff distance, Δ_e. Hence, the simplified governing equation results

$$\left(\frac{2}{3}R + \Delta_e\right)\dot{P} + a_2\frac{2\Delta_e}{R}P = M_1 a_1 \tag{4.25}$$

Equation 4.25 closely resembles the governing equation of a one-degree-of-freedom *spring-damper system*, to which we can thus associate our system. Generally, the behavior of a spring-damper system is described by the following equation

$$c\dot{x}(t) + kx(t) = F(t) \tag{4.26}$$

where $x(t)$ is the degree of freedom, $\dot{x}(t)$ is its time-derivative, $F(t)$ is the forcing term, c is the damping coefficient and k is the spring constant. Comparing equations 4.25 and 4.26, we see that

$$\begin{cases} c = \dfrac{2}{3}R + \Delta_e \sim R \\ k = a_2\dfrac{2\Delta_e}{R} \sim const \end{cases} \tag{4.27}$$

Hence, we can express the governing equation of the simplified spring-damper system

$$c\dot{P} + kP = u_1 \tag{4.28}$$

where the degree of freedom is the density ratio, P, and the forcing term is the inflow velocity, $u_1 = M_1 a_1$. We observe that, as we had guessed, the size of the parachute is associated with damping: specifically, the damping coefficient is proportional to the canopy radius. The elastic constant, instead, is proportional to the ratio Δ_e/R,

as a_2 is approximately constant. Since Δ_e is proportional to R (equation 4.17), it follows that k is a constant of the system. We also note that equation 4.28 is a *linear* first-order differential equation: to obtain the spring-damper system, actually, we have linearized the system around its equilibrium position. Having reduced the governing equation to a canonical form, we can now express it by means of the Laplace variables. From equation 4.28, we derive

$$P(s)[c\,s + k] = U_1(s) \tag{4.29}$$

by indicating with capital letters the following Laplace transforms: $P(s) = \mathcal{L}[P(t)]$, $sP(s) = \mathcal{L}[\dot{P}(t)]$, $U_1(s) = \mathcal{L}[u_1(t)]$. We can now define the transfer function[4] of the system, $T(s)$

$$T(s) = \frac{P(s)}{U_1(s)} = \frac{1}{cs + k} = \frac{k^{-1}}{\tau s + 1} \tag{4.30}$$

where $\tau = c/k$ is the *time constant* of the system; the settling time is defined as $\tau_s = 3\tau$. Since k is constant, both τ and τ_s are proportional to the canopy radius, confirming the hypothesis made earlier. The reciprocal of the spring constant, k^{-1}, is the amplitude of the steady-state response to a unit step input, $U_1(s) = s^{-1}$. As we will see later, this value represents the *static amplification factor* of the response. All coefficients are listed in table 4.4. The spring constant is equal to $k = 0.84$, leading to a static amplification factor of $k^{-1} = 1.19$. The positive nature of the time constant indicates that the system is stable, as expected. We also note that these values of settling time are in good match with those obtained graphically from the full system response, (figure 4.11), leaning toward the validity of this analysis.

Radius	k	c	τ	τ_s
R_0	0.84	1.27	1.53	4.53
$3R_0$	0.84	3.85	4.59	13.76

Table 4.4: Spring constant, k, damping coefficient, c, time constant, τ, and settling time, τ_s, for two values of canopy radius, R_0 and $3R_0$.

Now we verify the reliability of the simplified spring-damper model, using as reference the transient response of the full system, reported in figure 4.11. To this purpose, we calculate the inverse Laplace transform of the spring-damper response, $P(s)$, to the unit step input, $U_1(s) = s^{-1}$. In this way, we get the spring-damper response in the time domain, $P(t)$

$$P(t) - P_e = \mathcal{L}^{-1}\Big[P(s)\Big] = \mathcal{L}^{-1}\left[\frac{T(s)}{s}\right] = \mathcal{L}^{-1}\left[\frac{k^{-1}}{s(\tau s + 1)}\right] = \frac{1}{k}\left(1 - e^{-\frac{t}{\tau}}\right) \tag{4.31}$$

The trend over time of the spring-damper response, setting null initial conditions (i.e. $P_e = 0$), is shown in figure 4.12. To compare this response with that of the full system, we need to calibrate the value of the step amplitude, which is set to $A = 0.32$. We also have to add the initial conditions, i.e. the density ratio at equilibrium, which is equal to $P_e = 2.13$, as derived in section 4.3.

4 The *transfer function* of a system represents the relationship between the output signal and the input signal, for all possible values of the input. It is defined as the ratio of the Laplace transform of the output variable to the Laplace transform of the input variable, assuming all initial conditions to be zero.

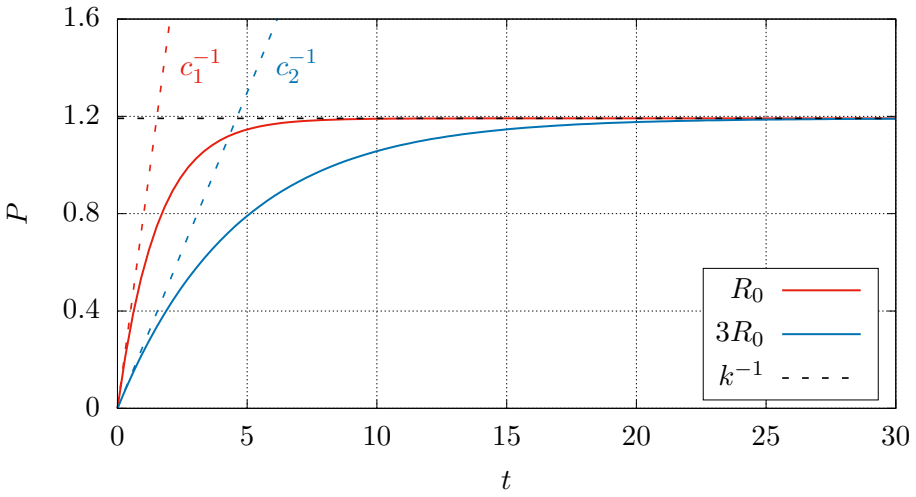

Figure 4.12: Time-response of the spring-damper system, P, to a unit step input (computed by equation 4.31) for the values R_0 and $3R_0$. Spring constant, k, and damping coefficients, c_1 and c_2, are listed in table 4.4, with $c_1 = c(R_0)$ and $c_2 = c(3R_0)$.

Thus, the response over time of the spring-damper system becomes

$$P(t) = P_e + \frac{A}{k}\left(1 - e^{-\frac{t}{\tau}}\right) = 2.13 + 0.38\left(1 - e^{-\frac{t}{\tau}}\right) \tag{4.32}$$

In figure 4.13 is shown a comparison between the two responses of full model and spring-damper model, both obtained by setting the value of canopy radius to R_0 in 4.13a and $3R_0$ in 4.13b. We observe that the simplified spring-damper model provides a transient response that is substantially correct, with a good estimate of the settling time, after which the system reaches a steady state. Moreover, it is able to capture how the system response varies as a function of the canopy radius. From the graph, we can see that the simplified system is unable to capture the first overshoot, which results from the non-linear terms in the governing equation of the full system. The spring-damper model, in fact, has been derived by assuming a steady shock wave ahead of the canopy, fixing the standoff distance at equilibrium. In mathematical terms, this is equivalent to linearizing the system around the equilibrium position, and results in simplifying the full non-linear system into a first-order linear system,

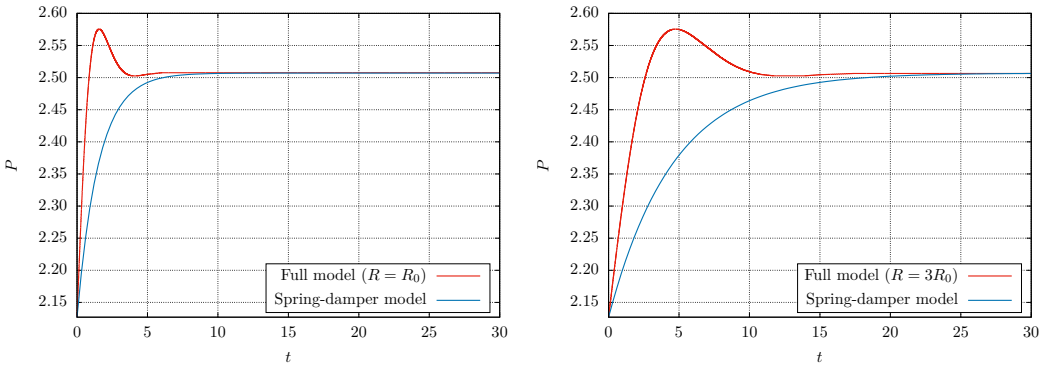

(a) $R = R_0$ **(b)** $R = 3R_0$

Figure 4.13: Step-input response, P, of both full and spring-damper systems, for two values of canopy radius, R_0 and $3R_0$. The spring-damper model correctly estimate the response time, despite not being able to capture the first overshoot.

whose response is overshoot-free by definition. In any case, the first overshoot is not relevant for our purposes. Much more relevant, instead, is the qualitative description of the system behavior, and the correct estimation of the response time as a function of the canopy radius. The latter is the specific purpose of this analysis, which is also essential to identify the driving parameters, and give them a physical meaning in terms of spring constant, damping coefficient and time constant.

Having verified the reliability of the spring-damper model through the study of the *transient* response, we can exploit this model to study the frequency response of the system. This is precisely the topic of the next section, where we will focus on the *steady-state* response of the system.

4.6 FREQUENCY-DOMAIN ANALYSIS

To exhaustively assess the stability of the system, its response should be evaluated not only under nominal conditions, as already discussed in section 4.4, but also under exceptional conditions. The effect of external conditions can be simulated by varying the frequency of the input signal. Actually, we are interested in understanding the effect of the input frequency on the system behavior for two main reasons:

- the actual inflow Mach number is not a pure tone, as assumed so far, but is characterized by a continuous spectrum, with high-amplitude contributions at both lower and higher frequencies compared to the fundamental one, $Sr = 0.16$. Specifically, an amplitude peak of 0.02 is found at $Sr = 0.80$, comparable with the fundamental contribution of 0.03, as shown in figure 4.6a;
- in addition to capsule wake fluctuations, representing the nominal inflow condition, the parachute could also be perturbed by wind gusts, characterized by high-frequency velocity oscillations. Precisely these difficult-to-predict environmental conditions have been identified as one of the main causes behind the failure of ExoMars 2016 mission, as highlighted in section 1.4.

We proceed, thus, with the frequency analysis of the system response. Exploiting the previously developed spring-damper model, the problem is greatly simplified: since this system is linear, we can apply the *principle of superposition*. This allows us to focus on the steady-state response, knowing that the transient response, derived in section 4.5, can be simply added to obtain the full response. For simplicity, we first consider a null-average sine-wave input $u_1(t) = u_0 \sin \omega t$, where u_1 is the inflow velocity. As known, the steady-state response of a one-degree-of-freedom system to a harmonic input is also harmonic, with the same frequency of the driving force. Recalling equations 4.25 and 4.27, we can write

$$c\dot{P} + kP = u_0 \sin \omega t \tag{4.33}$$

where u_0 is the input amplitude, and $\omega = 2\pi Sr$ is its angular frequency, in terms of Strouhal number. Thanks to Euler's identity, the input sine-wave can be written as

$$u_1(t) = u_0 \sin \omega t = \mathrm{Im}(u_0 e^{i\omega t}) \tag{4.34}$$

For simplicity of notation, we will only consider the imaginary part, neglecting the real one. This allows us to write the input as $u_1(t) = u_0 e^{i\omega t}$.

Being characterized by the same frequency of the input, the steady-state response can be expressed as

$$P(t) = P_0 e^{i\omega t} \quad \xrightarrow{\mathrm{d}/\mathrm{d}t} \quad \dot{P}(t) = i\omega P_0 e^{i\omega t} \tag{4.35}$$

where P_0 is the response amplitude. Equation 4.33 then becomes

$$P_0 e^{i\omega t}\Big(i\omega c + k\Big) = u_0 e^{i\omega t} \quad \xrightarrow{\cdot e^{-i\omega t}} \quad P_0 = \frac{u_0}{i\omega c + k} \tag{4.36}$$

We can now define the *frequency response function* of the system, $T(i\omega)$

$$T(i\omega) = \frac{P_0}{u_0} = \frac{1}{i\omega c + k} = \frac{k^{-1}}{\tau i\omega + 1} \tag{4.37}$$

where $\tau = c/k$ is the time constant of the system, previously derived. We note that, if we assume $s = i\omega$, then $T(i\omega)$ coincides with the transfer function of the system, $T(s)$, defined in equation 4.30. The frequency response function can be conveniently expressed in polar form

$$T(i\omega) = |T(i\omega)|e^{i\varphi} \tag{4.38}$$

where $\varphi(\omega)$ is its phase and $|T(i\omega)|$ is its module (or *amplification factor*), respectively defined as

$$\varphi(\omega) = atan(\omega\tau) \tag{4.39}$$

$$|T(i\omega)| = \left|\frac{k^{-1}}{\tau i\omega + 1}\right| = \frac{k^{-1}}{\sqrt{\omega^2\tau^2 + 1}} \tag{4.40}$$

Hence, the steady-state response of the spring-damper system in the time-domain results

$$P(t) = |T(i\omega)|e^{i\varphi}u_0 e^{i\omega t} = |T(i\omega)|u_0 \sin(\omega t + \varphi) \tag{4.41}$$

Equation 4.41 states that a sinusoidal input produces a sinusoidal output, according with the results of section 4.4. We can now compare the steady-state response of the spring-damper system with the response of the full system. To this purpose, we have to consider a sine-wave input characterized by a Strouhal number of $Sr = 0.16$, derived in 4.3, and evaluate module and phase of the frequency response function for that precise value. In this case, the input has a non-null mean, and can be written as $u_1 = a_1 M_1 = a_1(M_e + A\sin\omega_0 t)$, where $\omega_0 = 2\pi \cdot 0.16 = 1.01$ is the *fundamental angular frequency* of the input. Hence, we can write the input of the system, and its output evaluated at the input frequency

$$Input \quad \longrightarrow \quad u_1 = u_e + u_0 \sin(\omega_0 t) \tag{4.42}$$

$$Output \quad \longrightarrow \quad P = P_e + |T(i\omega_0)|u_0 \sin(\omega_0 t + \varphi_0) \tag{4.43}$$

where $u_e = a_1 M_e = 1.82$ is the mean value of the input, $u_0 = a_1 A = 0.11$ is its amplitude, $P_e = 2.13$ is the mean value of the output, $\varphi_0 = \varphi(\omega_0)$ is its phase evaluated for ω_0. Because of the strong assumption of stationary shock wave, a calibration constant that multiplies the input amplitude must be included in the model. Based on the results of the full model, we assume a calibration constant of $\alpha = 3.10$, obtaining an input amplitude of $u_0 = a_1 A\alpha = 0.35$. Module and phase of the frequency response function, which depend on the canopy radius, are evaluated

for $\omega = \omega_0$, and listed in table 4.5 for both the reference value R_0 and the upper-limit value $3R_0$. We focus our attention on the value of the amplification factor, which is less than halved for the larger canopy compared to the smaller canopy. But we will return to this later.

Radius	*Sr*	$\lvert T(i\omega_0)\rvert$	$\varphi(\omega_0)$ [°]
R_0	0.16	0.65	-57.01
$3R_0$	0.16	0.25	-77.76

Table 4.5: Module and phase of the frequency response function, $T(i\omega)$, for two values of canopy radius, R_0 and $3R_0$.

Thus, we have derived the steady-state response of the spring-damper system, which can now be compared with the response of the full model. Both systems are subject to the same input, a sine-wave with angular frequency $\omega_0 = 2\pi \cdot 0.16$, and their output is expressed in terms of density ratio, P. Results are shown in figure 4.14, where we notice the excellent match of the two models. As expected, the output amplitude of the canopy with radius $3R_0$ is about halved compared with the reference case of R_0. This comparison shows that the spring-damper model is definitely capable of qualitatively describing the steady-state response of the system.

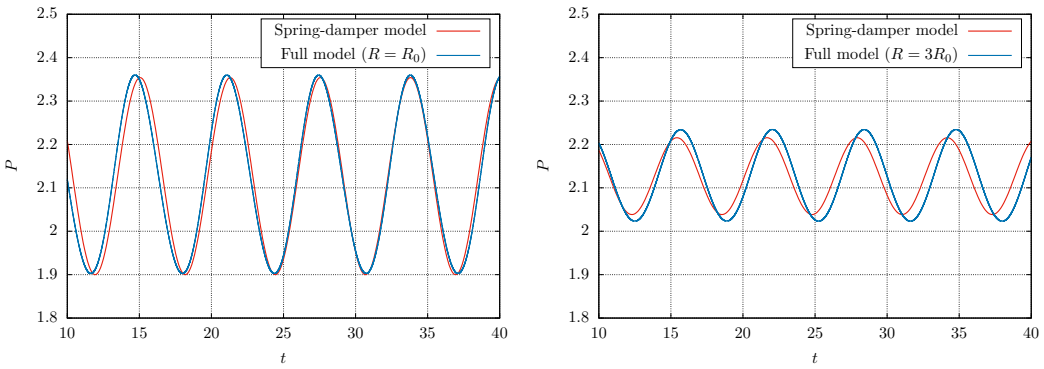

(a) $R = R_0$ **(b)** $R = 3R_0$

Figure 4.14: Steady-state response, P, to a sinusoidal input, estimated via both full model and spring-damper model (equation 4.43 with parameters 4.5). The canopy radius is set to R_0 in 4.14a and $3R_0$ in 4.14b.

Therefore, we can utilize this simplified model to further investigate the stability analysis of the system, trying to understand how *external* parameters, in terms of input frequency, impact on the behavior of the parachute. From equation 4.41, we see that the amplification factor represents a coefficient that, multiplied by the input, gives the amplitude of the output. Since the output represents the density fluctuations within the canopy, and the stability can be assessed precisely from the amplitude of density fluctuations, it follows that the amplification factor is directly related to the stability of the system. Thus, we calculate the trend of the amplification factor as a function of the input angular frequency: a lower amplification factor implies greater stability. By taking equation 4.40 with the values of spring constant, k, and time constant, τ, listed in table 4.4, we obtain the results shown in figure 4.15. From the graph appears that the amplification factor, $\lvert T(i\omega)\rvert$, decreases with the increase of both the angular frequency, ω, and the canopy radius, R.

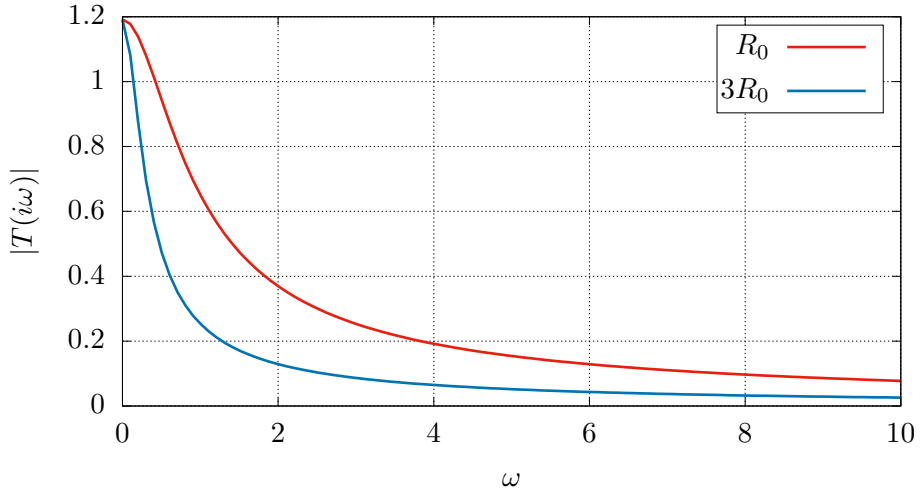

Figure 4.15: Amplification factor, $|T(i\omega)|$, as a function of the angular frequency, ω, and the canopy radius, R. $|T(i\omega)|$ decreases as both ω and R increase.

We observe that the maximum value of the amplification factor is reached in response to an input with zero frequency. This value, which we can refer to as *static amplification factor*, is equal to $|T(\omega = 0)| = k^{-1} = 1.19$, as already found in section 4.5. The static amplification factor, in fact, coincides with the response amplitude to a unit step, which is a zero-frequency input.

From figure 4.15, we can draw two main conclusions: *i)* a parachute with larger canopy is more stable, as shown in section 4.4; *ii)* low-frequency external forcing has a greater impact on parachute behavior. This is due to the fact that high-frequency input contributions are damped by the parachute (to a greater extent the larger the canopy), suggesting that the system behaves as a low-pass filter.

LOW-PASS FILTER BEHAVIOR

To generalize this results, it is convenient to represent the frequency response of the system with the *Bode diagram*, consisting of a gain plot and a phase plot, both expressed on a semi-logarithmic scale. The amplification factor, expressed as gain, is measured in decibel

$$|T(i\omega)|_{\text{dB}} = 20log_{10}|T(i\omega)| \quad [\text{dB}] \tag{4.44}$$

The Bode diagram of the spring-damper system is shown in figure 4.16. Having normalized the angular frequency, ω, with respect to the reciprocal of the time constant τ^{-1}, these diagrams are generally valid, independently of the canopy radius. The first relevant information we derive from the Bode diagram is that the system behaves as a low-pass filter: this means that all input frequencies higher than the cut-off threshold are damped. The *cut-off frequency*, ω_{cut}, is the reciprocal of the time constant

$$\omega_{cut} = \frac{1}{\tau} = \frac{k}{c} \sim \frac{1}{R} \tag{4.45}$$

A larger canopy, therefore, has a smaller cut-off frequency, and input frequencies begin to be damped from lower values. This results in an amplification factor that decreases more quickly, as can be inferred from the gain diagram 4.16a. In other words, a larger canopy is less affected by input high-frequencies, again proving to be more stable. This result is in full accordance with the hypothesis put forward

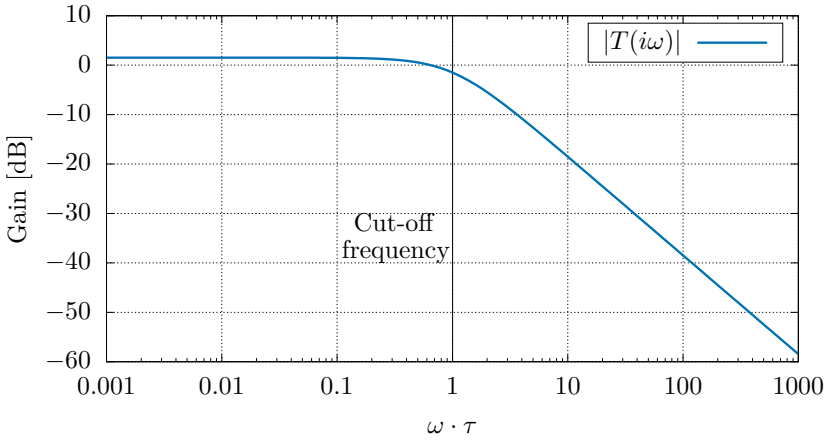

(a) Gain diagram

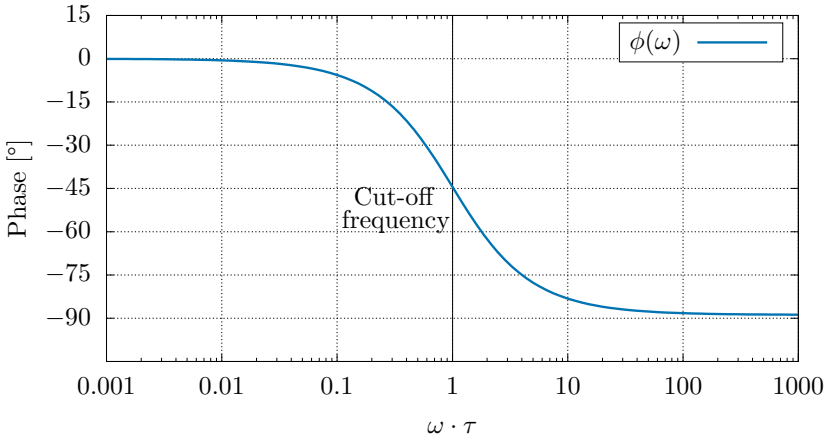

(b) Phase diagram

Figure 4.16: Bode diagram of the frequency response of the spring-damper system, whose behavior is equivalent to a low-pass filter. The frequency scale is logarithmic and normalized with respect to τ^{-1}. The static gain is $20log_{10}(k^{-1}) = 1.525\ dB$; the cut-off frequency is $\omega = \tau^{-1}$.

in section 4.4. The phase diagram 4.16b also provides interesting informations. It shows that the response of a system with a smaller canopy, characterized by a higher cut-off frequency, remains in phase with the forcing for a wider range of frequencies. Conversely, the response of a system with a larger canopy acquires a phase delay more rapidly ($\partial\varphi/\partial\omega < 0$), due to its longer response time.

4.7 PARACHUTE DRAG COEFFICIENT

Besides the assessment of the system stability, this model was also tailored to evaluate the drag coefficient of the parachute. Thus, we will resume the original model, more accurate than the spring-damper model, to conduct a final analysis on the parachute drag. In section 4.2 we have shown how the model can compute the Mach number of the shock, which is related to the density ratio through the normal shock relations. From the Mach number of the shock, we can compute the flow pressure on the canopy (by equation 4.11), whence we can estimate the parachute drag coefficient. The drag coefficient provided by the model will be compared with that computed by the simulation, for a further verification of the model reliability.

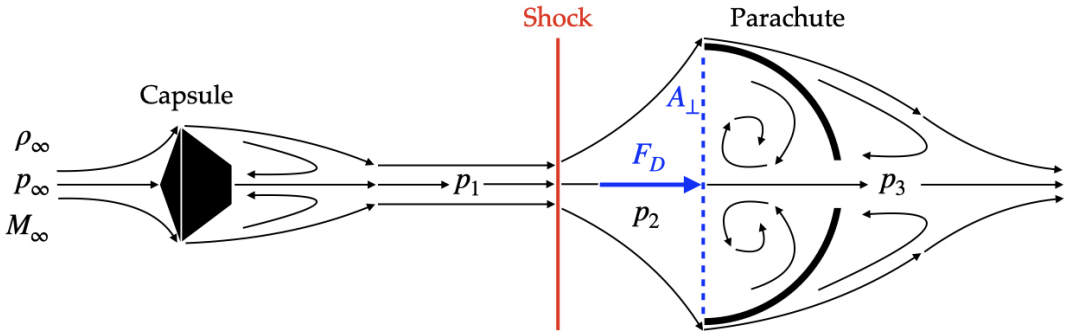

Figure 4.17: Sketch of the flow locations considered for the drag estimation.

In figure 4.17 are shown the flow locations that we consider to estimate drag: ∞ is the undisturbed flow, 1 is the capsule wake, 2 is the shock-downstream flow, 3 is the parachute wake. Referring to the figure, the parachute drag coefficient, C_D, is expressed as

$$C_D(t) = \frac{2F_D}{\rho_\infty u_\infty^2 A_\perp} \tag{4.46}$$

where $A_\perp = \pi(R^2 - R_v^2)$ is the canopy cross-section, F_D is the drag force, and $\rho_\infty = 1$, $p_\infty = 1$, $u_\infty = \sqrt{\gamma} M_\infty$ are the free-stream flow variables. As we have seen in chapter 3, we can assume that flow pressure in the parachute wake, p_3, has reached undisturbed conditions again, $p_3 \simeq p_\infty = 1$. Thus, the drag force acting on the parachute can be expressed as

$$F_D = \left(\frac{p_2}{p_\infty} - \frac{p_3}{p_\infty}\right) A_\perp \quad \xrightarrow{p_3 \simeq p_\infty = 1} \quad F_D \simeq (p_2 - 1) A_\perp \tag{4.47}$$

By substituting these values into equation 4.46, we get the expression of the modeled drag coefficient

$$C_D(t) = \frac{2(p_2 - 1)}{\gamma M_\infty^2} \tag{4.48}$$

The model provides the pressure ratio, p_2/p_1, where p_2 is the modeled flow pressure on the canopy, and p_1 is the flow pressure in the capsule wake, which is computed from the simulation at $x = 8, y = 0, z = 0$.

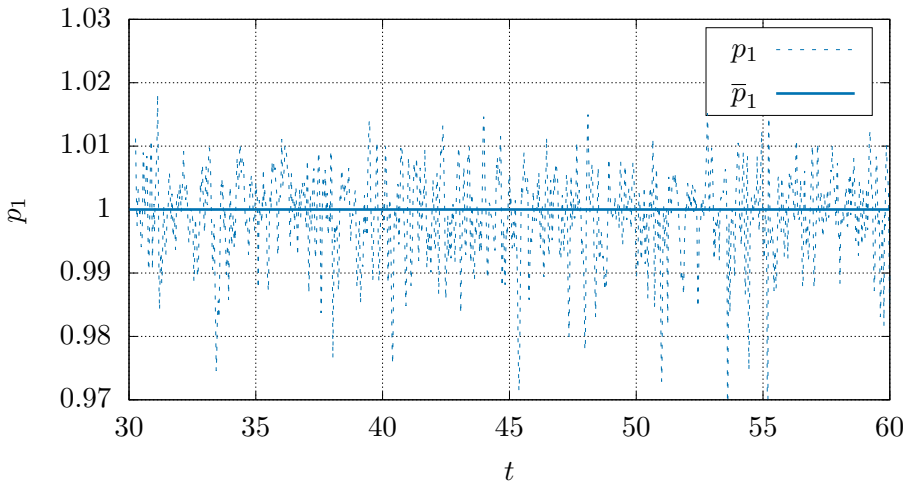

Figure 4.18: Time-trend of the capsule-wake pressure, p_1, and its time-average, $\overline{p}_1 = 1$.

As shown in figure 4.18, the capsule-wake pressure restores undisturbed conditions, $p_2 \simeq p_\infty = 1$. By averaging p_1 over time, we obtain $\overline{p}_1 = 1$, with maximum fluctuations around 2%, meaning that $p_2 \simeq p_2/p_1$. Thus, we can calculate the parachute drag coefficient directly from the model, obtaining the time-trend shown in figure 4.19.

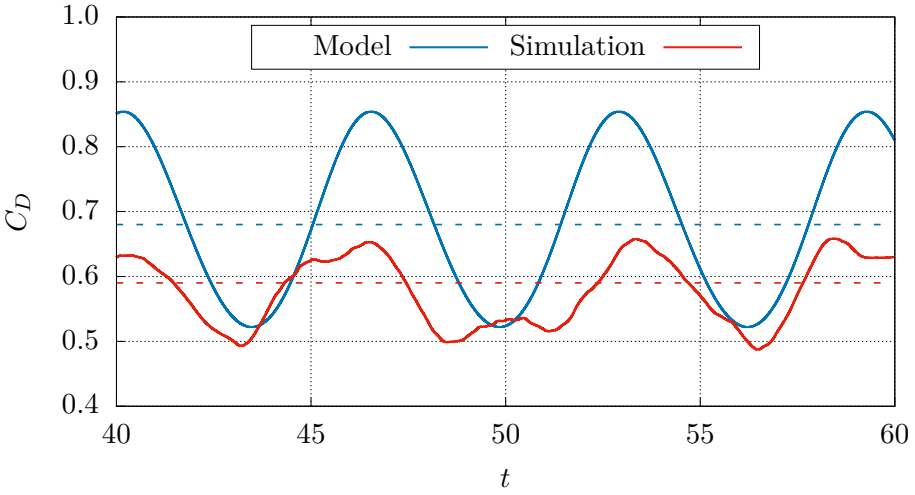

Figure 4.19: Simulated (red) and modeled (blue) drag coefficients, with mean values respectively of 0.59 and 0.68. The modeled drag matches well the simulated one, in terms of mean value, oscillations amplitude and frequency.

In the graph we also report the simulated drag coefficient: by comparing modeled and simulated drag coefficients, we can appreciate the excellent match between the two, in terms of mean value, oscillations amplitude and frequency. As for the mean value, considering the same time window used in the simulation, $t \in [40, 60]$, we obtain a mean pressure of $\overline{p}_2 = 2.77$, hence the mean drag coefficient results

$$\overline{C}_D = \frac{2(\overline{p}_2 - 1)}{\gamma M_\infty^2} = 0.68 \tag{4.49}$$

This value is remarkably close to that of the simulation, $\overline{C}_D = 0.59$, confirming the accuracy and reliability of the model. This comparison was made with the geometric (or *internal*) parameters used in the simulation. We will now see what is the effect of these parameters on the drag.

EFFECT OF GEOMETRIC PARAMETERS

In the previous sections we have shown that a larger canopy is more stable. Now, we see how the canopy size affects drag. As might be expected, the effect of canopy size on flow pressure is similar to that on density: as the radius increases, the amplitude of fluctuations decreases, while the mean value is unchanged. As visible from equations 4.48 and 4.49, this leads to an identical mean drag coefficient, which *instantaneously* has fluctuations of smaller amplitude. The time-trend of the parachute drag coefficient for two values of canopy radius, R_0 and $3R_0$, is shown in figure 4.20. As before, the vent radius, R_v, is changed so that the ratio R/R_v remains fixed. From the graph, we see that in both cases the mean value is $\overline{C}_D = 0.68$ (black dashed line). The amplitude of fluctuations, instead, is halved in the case of larger radius, $3R_0$, compared to the reference one, R_0. These results are summarized in table 4.6. As far as the vent size is concerned, it does not affect the trend of the drag coefficient, which is identical in the two cases of a canopy without vent and with vent doubled from the reference.

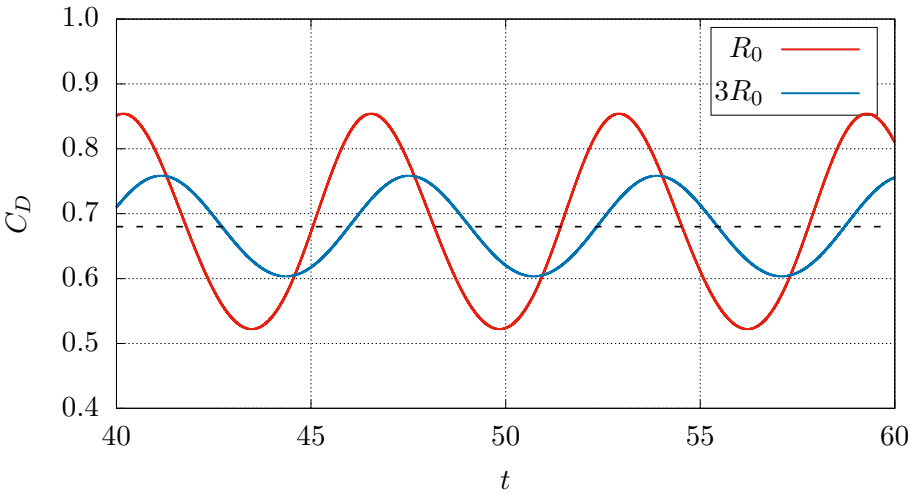

Figure 4.20: Drag coefficient, C_D, for two values of canopy radius, R_0 and $3R_0$. Mean values of C_D are both equal to 0.68; the amplitude of oscillations is 17% of the mean value for R_0, 8% of the mean value for $3R_0$.

Canopy radius	M_∞	$\overline{C}_D$	*Amplitude* [%]	*Frequency* [Sr]
R_0	2	0.68	17	0.16
$3R_0$	2	0.68	8	0.16

Table 4.6: Mean value ($\overline{C}_D$), fluctuations amplitude (% of the mean) and frequency (Sr) of the modeled drag coefficient, for two values of canopy radius, R_0 and $3R_0$.

In the final instance, some consideration must be made about drag *force*. The drag force is defined as

$$F_D(t) = \frac{1}{2}\rho_\infty u_\infty^2 A_\perp C_D(t) \tag{4.50}$$

All parameters except C_D are constant over time, so the remarks made on the drag coefficient remain valid. Besides C_D, the other significant parameter is the canopy cross-section, $A_\perp = \pi(R^2 - R_v^2)$, which depends on internal parameters. Recalling that $\rho_\infty = 1$ and $u_\infty = \sqrt{\gamma} M_\infty = 2.28$, we report in table 4.7 the values of the mean drag force, as a function of internal parameters. We see that, in the limit case of a canopy without vent, the drag force is not significantly increased, pointing out the negligibility of the effect of the vent size. Conversely, tripling the canopy radius leads to a drag force that is almost ten times greater. This is a limit case: purpose of this analysis is to identify a possible direction to follow for an optimal design of the parachute. Any increase in the size of the canopy should be accompanied by considerations regarding the strength limit of the material, as well as the weight of the capsule that needs to be slowed down.

Canopy radius	*Vent radius*	$\overline{F}_D$
R_0	R_v	13.31
R_0	0	13.44
$3R_0$	$3R_v$	119.73

Table 4.7: Mean value of the modeled drag force as a function of geometric parameters.

4.8 SUMMARY OF THE MODEL RESULTS

The analytical model of the parachute breathing cycle, after being validated, was used both in its original form and in a simplified form to study the behavior of a supersonic parachute. The model can help to understand the driving mechanisms of the breathing, and can provide general guidelines for the design of a parachute that achieves the optimal condition between stability and drag. The most relevant results we have accomplished can be enclosed in the following points:

SUMMARY OF THE BREATHING-MODEL RESULTS

- the model is able to analytically describe the parachute breathing cycle, whose effect is to amplify density fluctuations within the canopy;
- a parachute with larger canopy is more stable, in an increasingly pronounced way as the Mach number drops toward the sonic condition;
- the vent size does not have an appreciable impact on the parachute behavior: thus, increase its size for stability does not seem judicious;
- the parachute can be associated with a spring-damper system, with spring constant appearing to be independent of the canopy radius;
- the canopy radius appears to be proportional to the damping coefficient, which is responsible for damping density fluctuations within the canopy;
- the canopy radius is also proportional to the time constant, meaning that a larger parachute responds more slowly to the input forcing;
- the parachute behavior is analogous to that of a low-pass filter, with cut-off frequency inversely proportional to the canopy radius;
- consequently, the parachute dynamics is more affected by low-frequency forcing (undamped), rather than high-frequency forcing (damped);
- a lower cut-off frequency corresponds to a narrower bandwidth, thus a larger canopy dampens the input forcing starting from lower frequencies;
- the modeled drag coefficient excellently matches the simulated drag coefficient, in terms of mean value, oscillations amplitude and frequency;
- a larger canopy ensures a drag coefficient with equal mean but smaller amplitude of fluctuations, providing, moreover, much greater drag force.

CONCLUSIONS 5

5.1 ACTIVITIES CARRIED OUT

In the present work, we focused on the descent phase of a parachute-capsule system towards Mars. It is a timely topic, given the interest of space agencies in Mars exploration, on which state-of-the-art research is not yet exhaustive. In fact, the dynamics of supersonic parachutes includes coupled phenomena of different nature with complex interactions, making it difficult to simulate this problem. We opted to employ a CFD approach, assuming a rigid-parachute model, in order to fully understand the flow physics and aerodynamic interactions involved.

We simulated a supersonic compressible flow over a parachute-capsule system based on ESA's ExoMars 2022 mission. We used the ILES, an approach that allows to capture the unsteadiness of the problem, while keeping the computational cost affordable; moreover, it does not require any implementation of external turbulence model. Capsule and parachute were considered rigid and fixed in space, and BCs at the fluid-structure interface have been imposed through the GPFM, a direct discrete-forcing IBM. Free-stream Mach number was set to $M_\infty = 2$, corresponding to the flight regime of the capsule at the moment of parachute deployment, being also the most critical regime as for the stability. The Reynolds number based on capsule diameter, $Re = 10^6$, was provided by ExoMars database; heat capacity ratio and Prandtl number were set to $\gamma = 1.3$ and $Pr = 0.72$, with the aim of simulating the CO_2 environment of Mars. The Navier-Stokes equations, expressed in dimensionless formulation, have been solved with the in-house finite-difference code STREAmS [34].

5.2 CONCLUDING REMARKS

The results of the simulation have been examined in terms of instantaneous, time-averaged and fluctuating fields. Through the analysis of instantaneous fields, we identified some canonical flow regions, with a comparable structure around both capsule and parachute. Specifically, a bow shock generates in front of the solid body; an expansion fan at the corner accelerates the flow, which is then returned to free-stream conditions by the recompression shock; at the body corner originates a lip shock, bounding the external inviscid flow from the internal turbulent wake. The parachute region differs by the presence of the supersonic jet leaving the vent. In this region of confluence between supersonic flow and subsonic turbulent wake, it has been identified a kinetic-to-thermal energy transfer, known as pressure dilatation.

The aerodynamic interaction between the turbulent wake behind the capsule and the bow shock ahead of the canopy was especially investigated. The canopy bow shock is incessantly disrupted by the incoming wake, whose fluctuations are amplified as it traverses the shock, leading to flow unsteadiness and potential system instability. This unsteadiness is related to the parachute breathing, an oscillatory phenomenon that produces large variations in the parachute drag. The breathing involves a periodic motion of the canopy shock along the symmetry axis: the shock moving downstream towards the parachute corresponds to an over-pressurized state

and high drag (parachute *inhaling*), while the shock moving upstream towards the capsule corresponds to an under-pressurized state and low drag (parachute *exhaling*). Parachute breathing has been highlighted by computing the RMS of density and pressure fluctuations. Moreover, thanks to a TKE map normalized with respect to both free-stream and local conditions, we were able to precisely locate the most unsteady flow regions.

With the aim of analytically modeling the parachute breathing cycle, we explored the original idea that it can be related to the *big buzz* instability. To better understand the driving mechanisms, we simplified the geometry, considering a normal shock and a straight sonic line between shock and parachute. A zero-dimensional model based on a mass balance was developed and validated against the simulation results with excellent match. By setting the inflow Mach number (input), the model provides the trend over time of all the variables of interest (output). The model was used to conduct a stability analysis as a function of the canopy radius, showing that a larger canopy is subject to smaller drag fluctuations, and it is consequently more stable. This result is in agreement with previous studies, e.g. [28] and [47]. A relevant remark is that the parachute designed for ExoMars 2022 mission appears potentially subject to density fluctuations with maximum amplitude, compared to both smaller and larger parachutes, at $M_\infty = 2$. The vent size does not have a noticeable impact on parachute behavior, making it seem unwise to increase its size hoping for greater stability. Through a Laplace-domain analysis, the original model was reduced to a canonical spring-damper system, allowing to give a physical meaning to the main terms of the governing equation. Specifically, a damping coefficient was associated to the canopy radius, which is thus responsible for damping fluctuations within the canopy. With a frequency-domain analysis, we showed that the system is comparable to a low-pass filter, with cut-off frequency inversely proportional to the canopy radius: all input frequencies higher than the cut-off are damped by the system and do not impact its stability, in contrast to low-frequency forcing that most affects the parachute dynamics. A summary of the model results can be found in section 4.8.

5.3 FUTURE PERSPECTIVES

In the present work of master's thesis, we have achieved results that can be considered satisfactory, yet they still require further development and implementation. Possible (and necessary) developments will be cited according to an increasing level of computational effort.

In the first place, it is possible to enlarge the available database of simulations, both at different flight regimes and with different parachute geometries. To improve the simulation accuracy, we could develop an ad-hoc wall model to be incorporated into the LES, so that the boundary layer that forms on solid surfaces can be evaluated. A relevant improvement is to simulate the impact of parachute oscillations on the capsule trajectory, by modeling the two bodies as a coupled 3-degree-of-freedom system. Finally, the major step forward is to describe the deformations of the flexible canopy. To this purpose, a finite-element thin-structure solver needs to be developed and coupled with the finite-difference fluid solver. The coupling between the two solvers can be achieved through an IBM that is suitable for thin structures (so that it is accurate in space) and based on a feedback scheme (so that it is accurate in time). This ad-hoc developed IBM will have to capture the mutual influence between the flow, which deforms the structure, and the structure, which in turn influences the flow.

APPENDIX

A.1 LINEARIZED MODEL OF BREATHING CYCLE

In chapter 4, we have seen that a parachute with a larger canopy is subject to fluctuations of smaller amplitude and, consequently, it is more stable. The stability of the system can be further examined by linearizing the model around the equilibrium position. If we express the time-derivative of the pressure ratio as $\partial P/\partial t = \dot{P}$, equation 4.9 becomes

$$\dot{P} = \frac{\pi R^2}{V} M_1 a_1 - \frac{P}{V}\left[\left(\pi R_v^2 + 2\pi R\Delta\right)a_2 + \pi R^2\left(M_s - M_1\right)a_1\right] \tag{A.1}$$

The time-variation of the system response, $\dot{P}$, is a function of the system response, P, and the system input, M_1. To demonstrate this (recalling that a_1 is a model constant) we explicate the dependence of the variables involved

$$\begin{cases} M_s = M_s(P) \\ a_2 = a_2(M_s) = a_2(P) \\ \Delta = \Delta(M_1, M_s) = \Delta(M_1, P) \\ V = V(\Delta) = V(M_1, P) \end{cases} \tag{A.2}$$

hence

$$\dot{P} = f(P, M_1, M_s, a_1, a_2) \implies \dot{P} = f(P, M_1) \tag{A.3}$$

The function $f(P, M_1)$ can be linearized around the equilibrium position by Taylor series expansion, which for simplicity we truncate to first order. Indicating the equilibrium position with $\bullet_e$, we have

$$\dot{P} = f(P, M_1) \xrightarrow{\text{LIN}} \dot{P} \simeq f(M_e, P_e) + \left.\frac{\partial f}{\partial P}\right|_e (P - P_e) + \left.\frac{\partial f}{\partial M_1}\right|_e (M_1 - M_e) \tag{A.4}$$

where $f(M_e, P_e) = 0$, by definition of equilibrium position. If we define $(P - P_e) = \delta P$ and $(M_1 - M_e) = \delta M_1$, we can write

$$\dot{P} \simeq \left.\frac{\partial f}{\partial P}\right|_e \delta P + \left.\frac{\partial f}{\partial M_1}\right|_e \delta M_1 \tag{A.5}$$

Thus, we proceed with the calculation of the partial derivatives of all dependent variables with respect to P and M_1. Simulation results show that the variation of a_2 is negligible, so we can assume $a_2 = a_{2,e} = const$. If we define the speed of sound ratio as $A = a_2/a_1$, we can set $A = A_e = const$, hence $\partial A/\partial P = \partial A/\partial M_1 = 0$.

From equations 4.10, 4.3, 4.1, we derive

$$\begin{cases} \dfrac{\partial M_s}{\partial P} = \dfrac{\gamma+1}{\sqrt{2P}}\Big[(\gamma+1) - P(\gamma-1)\Big]^{-3/2} \\ \dfrac{\partial \Delta}{\partial P} = a_1 t \dfrac{\partial M_s}{\partial P} \\ \dfrac{\partial \Delta}{\partial M_1} = -a_1 t \\ \dfrac{\partial}{\partial P}\left(\dfrac{1}{V}\right) = -\dfrac{\pi R^2}{V^2} a_1 t \dfrac{\partial M_s}{\partial P} \\ \dfrac{\partial}{\partial M_1}\left(\dfrac{1}{V}\right) = \dfrac{\pi R^2}{V^2} a_1 t \end{cases} \tag{A.6}$$

We can now calculate the partial derivatives of the function f, i.e. $\partial f/\partial P$ and $\partial f/\partial M_1$, and evaluate them at the equilibrium position, obtaining

$$\left.\frac{\partial f}{\partial P}\right|_e = -\Big(\alpha^2 R^2 \varepsilon\beta + \alpha\delta\varepsilon\Big)\cdot t + \alpha\gamma \tag{A.7}$$

$$\left.\frac{\partial f}{\partial M_1}\right|_e = \Big(\alpha^2 R^2 \beta + \alpha\delta\Big)\cdot t + \alpha\zeta \tag{A.8}$$

where

$$\begin{cases} \alpha = a_1\pi/V_e \\ \beta = R^2 M_e - R_v^2 P_e A_e - 2R\Delta_e P_e A_e \\ \gamma = -R_v^2 A_e - 2R\Delta_e A_e - R^2 P_e \varepsilon \\ \delta = 2RP_e a_2 \\ \varepsilon = (\partial M_s/\partial P)_e \\ \zeta = R^2(1+P_e) \end{cases} \tag{A.9}$$

are time-constant values that only depend on R, R_v, M_e. Since the constructive solution of interest seems to be a larger canopy, we decided to analyze two parachute configurations, corresponding to the reference case, $R = R_0$, and the upper-limit case, $R = 3R_0$. The vent radius, R_v, has been adjusted to keep $R/R_v = const$. For these two cases, equation A.5 respectively reduces to:

$$R = R_0 \quad \longrightarrow \quad \dot{P} \simeq \Big(3.86\cdot t + 2.80\Big)\delta M_1 - \Big(2.01\cdot t + 1.67\Big)\delta P \tag{A.10}$$

$$R = 3R_0 \quad \longrightarrow \quad \dot{P} \simeq \Big(0.43\cdot t + 0.93\Big)\delta M_1 - \Big(0.22\cdot t + 0.56\Big)\delta P \tag{A.11}$$

In the first place, we verify that the linearized model properly approximates the full model. In figure A.1 is shown a comparison between the response of the system, computed via both linearized and full model, to the sinusoidal input $M_1 = M_e + 0.1\sin(2\pi 0.16\cdot t)$, derived in section 4.3. As concerns the reference case, $R = R_0$, density trend over time estimated with the linearized model is in excellent match with the full model; in the second case, $R = 3R_0$, the linearized response seems to be in a slight phase advance compared to the full one, and oscillations amplitude is

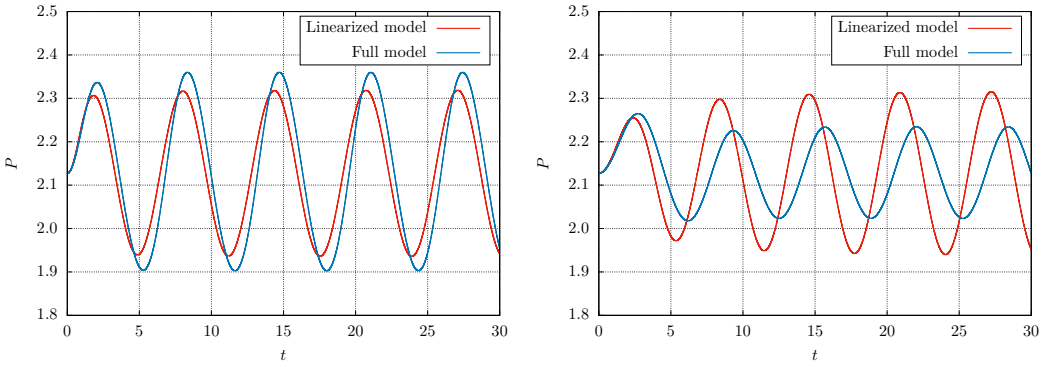

(a) $R = R_0$ **(b)** $R = 3R_0$

Figure A.1: Time-trend of the density ratio, P, obtained via both the linearized model and the full model. Responses are computed for the cases $R = R_0$ and $R = 3R_0$, with the input Mach number $M_1 = 1.6 + 0.1\sin(2\pi 0.16 \cdot t)$.

slightly over-estimated. However, the linearized model can be considered valid, since it captures the general trend of the response, which moves to a condition of dynamic equilibrium after the initial transient.

Once verified the reliability of the linearized model, we can use it to conduct a stability analysis. To assess the stability of the system, its response should be evaluated not only under nominal conditions, but also under exceptional ones, represented by an input signal with high-frequency oscillations. The system is therefore subject to a high-frequency sinusoidal input, characterized by a Strouhal number equal to $Sr = 1$. Since these perturbations are usually short-term, the considered time window is reduced to $t \in [0, 20]$. The linearized response to the input $M_1 = M_e + 0.1\sin(2\pi t)$ in shown in figure A.2.

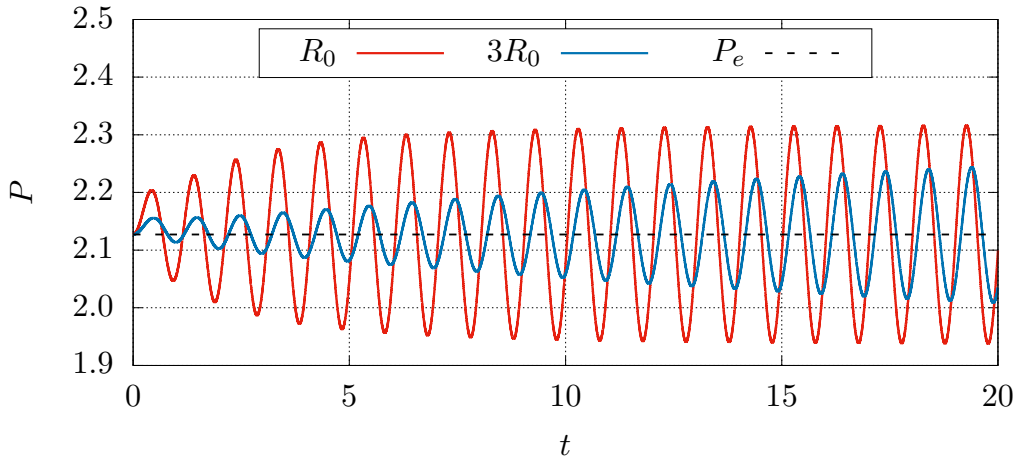

Figure A.2: Response of the linearized system to the sinusoidal input $M_1 = M_e + 0.1\sin(2\pi t)$, for different values of canopy radius, R_0 and $3R_0$. A larger radius leads to oscillations of smaller amplitude.

We observe that the response of the system with smaller canopy radius, R_0, quickly moves to the steady state, with high-amplitude oscillations. In contrast, the system with larger canopy radius, $3R_0$, takes longer to respond to the rapidly alternating oscillations, and therefore the oscillations amplitude can never reach the steady state value in the considered time window. This result is relevant, as the transient essence of high-frequency perturbations exhausts them quickly. Therefore, a parachute with

a larger canopy not only is more stable under nominal conditions, but is also less sensitive to this high-frequency disturbances. By widening the time interval, the response of the system with larger radius also reaches the steady state, but after longer time. This *response time* depends on the canopy radius: the larger the radius, the higher the response time.

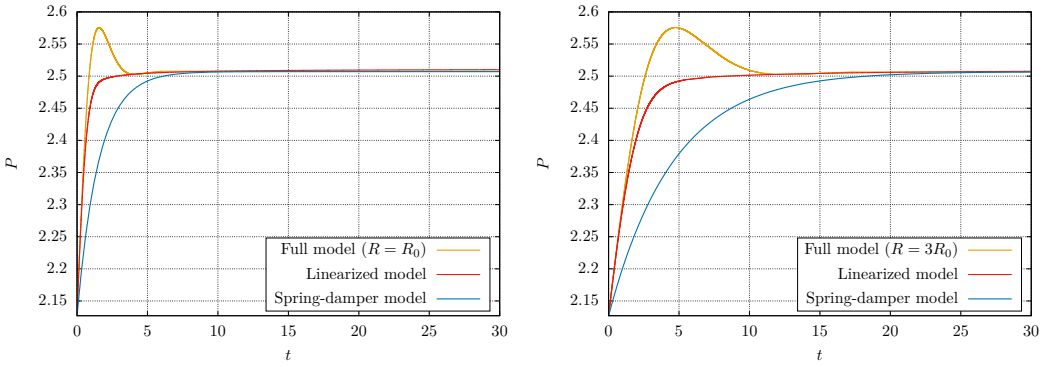

(a) $R = R_0$ **(b)** $R = 3R_0$

Figure A.3: System response, P, to a step input, estimated via full model, linearized model and spring-damper model, for two values of canopy radius, R_0 and $3R_0$. The two simplified models are in good agreement with the full one, despite not being able to capture the first overshoot.

The behavior of the linearized system via Taylor series expansion is further validated by studying the response to a step input. Results, compared with the full system and the spring-damper system, are shown in figure A.3, where we note that the linearized model correctly captures the response trend of the system.

BIBLIOGRAPHY

[1] M.C. Malin, M.H. Carr, and M.J.S. Belton. *Mars Spacecraft Exploration*. Encyclopædia Britannica. 2022.

[2] X. Xue and C.Y. Wen. "Review of unsteady aerodynamics of supersonic parachutes." In: *Progress in Aerospace Sciences* 125 (2021), p. 100728.

[3] K. Karagiozis, R. Kamakoti, F. Cirak, and C. Pantano. "A computational study of supersonic disk-gap-band parachutes using Large-Eddy Simulation coupled to a structural membrane." In: *Journal of Fluids and Structures* 27.2 (2011), pp. 175–192.

[4] W.G. Vincenti, J.W. Boyd, and G.E. Bugos. "H. Julian Allen: an appreciation." In: *Annu. Rev. Fluid Mech.* 39 (2007), pp. 1–17.

[5] R.C. Mehta. "Numerical simulation of supersonic flow past reentry capsules." In: *Shock Waves* 15.1 (2006), pp. 31–41.

[6] B.R. Hollis and S. Borrelli. "Aerothermodynamics of blunt body entry vehicles." In: *Progress in Aerospace Sciences* 48 (2012), pp. 42–56.

[7] G. Pezzella and A. Viviani. *Hypersonic Vehicles: Past, Present and Future Developments*. BoD–Books on Demand, 2019.

[8] D.E.A. Reichenau. *Aerodynamic characteristics of disk-gap-band parachutes in the wake of Viking entry forebodies at Mach numbers from 0.2 to 2.6*. Tech. rep. Arnold Engineering Development Center Arnold AFB TN, 1972.

[9] I. Clark and C. Tanner. "A historical summary of the design, development, and analysis of the disk-gap-band parachute." In: *2017 IEEE Aerospace Conference*. IEEE. 2017, pp. 1–17.

[10] J.R. Cruz and J. Lingard. "Aerodynamic decelerators for planetary exploration: past, present, and future." In: *AIAA Guidance, Navigation, and Control Conference and Exhibit*. 2006, p. 6792.

[11] A. Aboudan, G. Colombatti, C. Bettanini, F. Ferri, S. Lewis, B. Van Hove, O. Karatekin, and S. Debei. "ExoMars 2016 Schiaparelli module trajectory and atmospheric profiles reconstruction." In: *Space Science Reviews* 214.5 (2018), pp. 1–31.

[12] F. Ferri, Ö. Karatekin, S.R. Lewis, F. Forget, A. Aboudan, G. Colombatti, C. Bettanini, S. Debei, B. Van Hove, V. Dehant, et al. "Exomars atmospheric mars entry and landing investigations and analysis (AMELIA)." In: *Space Science Reviews* 215.1 (2019), pp. 1–21.

[13] T. Tolker-Nielsen. *ExoMars 2016 – Schiaparelli Anomaly Inquiry*. Report. European Space Agency, 2017.

[14] ESA Media Relations, ed. *ExoMars parachute testing moves forward*. 2020. URL: https://www.esa.int/Science_Exploration/Human_and_Robotic_Exploration/Exploration/ExoMars/ExoMars_parachute_testing_moves_forward.

[15] J.D. Maynard. *Aerodynamic characteristics of parachutes at Mach numbers from 1.6 to 3*. National Aeronautics and Space Administration, 1961.

[16] C.V. Eckstrom and J.S. Preisser. *Flight Test of a 30-foot Nominal Diameter Disk-gap-band Parachute Deployed at a Mach Number of 1.56 and a Dynamic Pressure of 11.4 Pounds Per Square Foot*. NASA technical memorandum. National Aeronautics and Space Administration, 1967.

[17] R.J. Bendura, L.C. Coltrane, and E.K. Huckins. *Performance of a 19.7 meter diameter disk gap band parachute in a simulated Martian environment*. Tech. rep. 1968.

[18] R.J. Bendura, R.R. Lundstrom, P.G. Renfroe, and S.R. LeCroy. *Flight tests of Viking parachute system in three Mach number regimes. 2: Parachute test results*. Tech. rep. 1974.

[19] R.D. Moog, R.J. Bendura, J.D. Timmons, and R.A. Lau. "Qualification flight tests of the Viking decelerator system." In: *Journal of Spacecraft and Rockets* 11.3 (1974), pp. 188–195.

[20] H. Murrow, C. Eckstrom, and D. Henke. "Development flight tests of the Viking decelerator system." In: *4th Aerodynamic Deceleration Systems Conference*. 1973, p. 455.

[21] S. Steinberg, P.M. Siemers, and R.G. Slayman. "Development of the Viking Parachute Configuration by Wind-Tunnel Investigation." In: *Journal of Spacecraft and Rockets* 11.2 (1974), pp. 101–107.

[22] J.R. Cruz, R. Mineck, D. Keller, and M. Bobskill. "Wind tunnel testing of various disk-gap-band parachutes." In: *17th AIAA Aerodynamic Decelerator Systems Technology Conference and Seminar*. 2003, p. 2129.

[23] A. Sengupta, R. Kelsch, J. Roeder, M. Wernet, A. Witkowski, and M. Kandis. "Supersonic performance of disk-gap-band parachutes constrained to a 0-degree trim angle." In: *Journal of Spacecraft and Rockets* 46.6 (2009), pp. 1155–1163.

[24] R. Lafarge, J. Nelsen, and K. Gwinn. "A novel CFD/structural analysis of a cross parachute." In: *32nd Aerospace Sciences Meeting and Exhibit*. 1993, p. 752.

[25] J. Lingard and M. Darley. "Simulation of parachute fluid structure interaction in supersonic flow." In: *18th AIAA Aerodynamic Decelerator Systems Technology Conference and Seminar*. 2005, p. 1607.

[26] J. Lingard, M. Darley, J. Underwood, and G. Brown. "Simulation of the Mars Science Laboratory parachute performance and dynamics." In: *19th AIAA Aerodynamic Decelerator Systems Technology Conference and Seminar*. 2007, p. 2507.

[27] M. Barnhardt, T. Drayna, I. Nompelis, G. Candler, and W. Garrard. "Detached eddy simulations of the MSL parachute at supersonic conditions." In: *19th AIAA Aerodynamic Decelerator Systems Technology Conference and Seminar*. 2007, p. 2529.

[28] A. Sengupta, A. Steltzner, K. Comeaux, G. Candler, M. Barnhardt, C. Pantano, J. Bell, J.T. Heineck, and E. Schairer. "Results from the Mars Science Laboratory parachute decelerator system supersonic qualification program." In: *2008 IEEE Aerospace Conference*. IEEE. 2008, pp. 1–15.

[29] H. Yu, C. Pantano, and F. Cirak. "Large-eddy simulation of flow over deformable parachutes using immersed boundary and adaptive mesh." In: *AIAA Scitech 2019 Forum*. 2019, p. 0635.

[30] X.P. Xue, H. Koyama, Y. Nakamura, and C.Y. Wen. "Effects of suspension line on flow field around a supersonic parachute." In: *Aerospace Science and Technology* 43 (2015), pp. 63–70.

[31] X. Yang. "Effect of air permeability on stability of supersonic parachute." In: *Aviation* 25.2 (2021), pp. 123–128.

[32] N. Dahal, K. Fukiba, K. Mizuta, and Y. Maru. "Study of pressure oscillations in supersonic parachute." In: *International Journal of Aeronautical and Space Sciences* 19.1 (2018), pp. 24–31.

[33] D.Z. Huang, P. Avery, C. Farhat, J. Rabinovitch, A. Derkevorkian, and L.D. Peterson. "Modeling, simulation and validation of supersonic parachute inflation dynamics during Mars landing." In: *AIAA Scitech 2020 Forum*. 2020, p. 0313.

[34] M. Bernardini, D. Modesti, F. Salvadore, and S. Pirozzoli. "STREAmS: A high-fidelity accelerated solver for direct numerical simulation of compressible turbulent flows." In: *Computer Physics Communications* 263 (2021), p. 107906.

[35] G.S. Jiang and C.W. Shu. "Efficient implementation of weighted ENO schemes." In: *Journal of computational physics* 126.1 (1996), pp. 202–228.

[36] R. Mittal and G. Iaccarino. "Immersed boundary methods." In: *Annu. Rev. Fluid Mech.* 37 (2005), pp. 239–261.

[37] F. De Vanna. "A high-resolution fully compressible Navier-Stokes solver for analysis of moving objects at high Mach numbers." PhD thesis. 2019.

[38] M. Bernardini, D. Modesti, and S. Pirozzoli. "On the suitability of the immersed boundary method for the simulation of high-Reynolds-number separated turbulent flows." In: *Computers & Fluids* 130 (2016), pp. 84–93.

[39] J.R. Cruz. "Parachutes for planetary entry systems." In: ed. by NASA Langley Research Center. 2005.

[40] J.R. Cruz, D. Way, J. Shidner, J.L. Davis, R.W. Powell, D. Kipp, D.S. Adams, A. Sengupta, A. Witkowski, and M. Kandis. "Parachute models used in the Mars Science Laboratory entry, descent, and landing simulation." In: *AIAA Aerodynamic Decelerator Systems (ADS) Conference*. 2013, p. 1276.

[41] A.J. Smits. *Lectures in fluid mechanics: Viscous flows and turbulence*. 2005.

[42] T.B. Gatski and J.P. Bonnet. *Compressibility, turbulence and high speed flow*. Academic Press, 2013.

[43] S. Trapier, S. Deck, and P. Duveau. "Delayed detached-eddy simulation and analysis of supersonic inlet buzz." In: *AIAA journal* 46.1 (2008), pp. 118–131.

[44] J. Yamamoto, Y. Kojima, M. Kameda, Y. Watanabe, A. Hashimoto, and T. Aoyama. "Prediction of the onset of supersonic inlet buzz." In: *Aerospace Science and Technology* 96 (2020), p. 105523.

[45] S. Trapier, P. Duveau, and S. Deck. "Experimental study of supersonic inlet buzz." In: *AIAA journal* 44.10 (2006), pp. 2354–2365.

[46] J.R. Adams, W. Martindale, and M. Varner. "One-dimensional unsteady modeling of supersonic inlet unstart/restart." In: *22nd Aerospace Sciences Meeting*. 1984, p. 439.

[47] A. Sengupta, A. Steltzner, A. Witkowski, G. Candler, and C. Pantano. "Findings from the supersonic qualification program of the Mars Science Laboratory parachute system." In: *20th AIAA Aerodynamic Decelerator Systems Technology Conference and Seminar*. 2009, p. 2900.